ABSTRACT

Title of dissertation: UNCERTAINTY QUANTIFICATION OF A RADIATIVE TRANSFER MODEL AND A MACHINE LEARNING TECHNIQUE FOR USE AS OBSERVATION OPERATORS IN THE ASSIMILATION OF MICROWAVE OBSERVATIONS INTO A LAND SURFACE MODEL TO IMPROVE SOIL MOISTURE AND TERRESTRIAL SNOW

Jongmin Park, Doctor of Philosophy, 2020

Dissertation directed by: Professor Barton A. Forman
Department of Civil and Environmental Engineering

Soil moisture and terrestrial snow mass are two important hydrological states needed to accurately quantify terrestrial water storage and streamflow. Soil moisture and terrestrial snow mass can be measured using ground-based instrument networks, estimated using advanced land surface models, and retrieved via satellite imagery. However, each method has its own inherent sources of error and uncertainty. This leads to the application of data assimilation to obtain optimal estimates of soil moisture and snow mass. Before conducting data assimilation (DA) experiments, this dissertation explored the use of two different observation operators within a DA framework: a L-band radiative transfer model (RTM) for soil moisture and support vector machine (SVM) regression for soil terrestrial snow mass. First, L-band brightness temperature (T_b) estimated from the RTM after being calibrated against multi-angular SMOS T_b's showed good performance in both ascending and descending overpasses across North America except in regions with sub-grid scale lakes and

dense forest. Detailed analysis of RTM-derived L-band T_b in terms of soil hydraulic parameters and vegetation types suggests the need for further improvement of RTM-derived T_b in regions with relatively large porosity, large wilting point, or grassland type vegetation. Secondly, a SVM regression technique was developed with explicit consideration of the first-order physics of photon scattering as a function of different training target sets, training window lengths, and delineation of snow wetness over snow-covered terrain. The overall results revealed that prediction accuracy of the SVM was strongly linked with the first-order physics of electromagnetic responses of different snow conditions. After careful evaluation of the observation operators, C-band backscatter observations over Western Colorado collected by Sentinel-1 were merged into an advanced land surface model using a SVM and a one-dimensional ensemble Kalman filter. In general, updated snow mass estimates using the Sentinel-1 DA framework showed modest improvements in comparison to ground-based measurements of snow water equivalent (SWE) and snow depth. These results motivate further application of the outlined assimilation schemes over larger regions in order to improve the characterization of the terrestrial hydrological cycle.

UNCERTAINTY QUANTIFICATION OF A RADIATIVE TRANSFER MODEL AND MACHINE LEARNING TECHNIQUE FOR USE AS OBSERVATION OPERATORS IN THE ASSIMILATION OF MICROWAVE OBSERVATIONS INTO A LAND SURFACE MODEL TO IMPROVE SOIL MOISTURE AND TERRESTRIAL SNOW

by

Jongmin Park

Dissertation submitted to the Faculty of the Graduate School of the
University of Maryland, College Park in partial fulfillment
of the requirements for the degree of
Doctor of Philosophy
2020

Advisory Committee:
Associate Professor Barton A. Forman, Chair/Advisor
Associate Professor Karen L. Prestegaard, Dean's Representative
Associate Professor Kaye L. Brubaker
Assistant Professor Michelle Bensi
Dr. Sujay Kumar

Foreword

Materials presented in Chapter 2 and Chapter 3 in this study have been submitted and reviewed in the peer-reviewed journals and expected to be published in the next few months. Chapter 4 of this study is expected to be submitted to the peer-reviewed journal in the next few months. The dissertation contents were conducted in its entirety by Jongmin Park. Please see the list of publications below.

Park, J., Forman, B.A., Tarik, S.B., De Lannoy, G.J.M., Reichle, R.H. Evaluation of GEOS-5 L-Band Microwave Brightness Temperatures using Aquarius Observations over Non-Frozen Land in North America, *Remote Sensing*, (2020) (Under Review).

Park, J., Forman, B. A., and Lievens, H. Prediction of active microwave backscatter over snow-covered terrain across Western Colorado using a land surface model and support vector machine regression, *IEEE Journal of Selected topics in applied earth observation and remote sensing*, (2020) (under review)

Park, J. and Forman, B. A. Estimation of snow mass information through assimilation of C-band synthetic aperture radar observations using an advanced land surface model and support vector machine regressions, *Water Resources Research*, (2020) (In preparation).

Acknowledgments

First and foremost, I would like to thank God for providing me the opportunity to undertake my research in the United States as well as the strength, wisdom, and ability to successfully fulfill this degree. This achievement would not be possible without his blessings, vision, and guidance.

During my Ph.D journey, I sincerely would like to express my deepest appreciation to my advisor, Dr. Forman, who has been a great mentor, a role model, friend, and, an inspiration. He provided me invaluable opportunities to study at the University of Maryland, College Park. I learned a lot from Dr. Forman, including the scientific process, numerous research-related skills and relevant communication skills in academia, and enthusiasm for both research and education. His keen intuition as well as his nice, endless handwritten comments on my draft papers help motivate me in the direction of becoming an independent researcher and pursue my future academic career. I also want to express my gratitude to all my dissertation committee members, Dr. Brubaker and Dr. Bensi (from Civil and Environmental Engineering), Dr. Prestegaard (from Department of Geology), and Dr. Kumar (research physical scientist at Goddard Space Flight Center, NASA) for agreeing to serve on my dissertation committee. It is great pleasure for me to have all four experts on my research committee. Their indispensable comments and suggestions helped improve the quality of this dissertation. Their valuable comments also provide me to with critical thinking skills throughout the research as well as help improve communication skills.

In addition to the committee members, I would like to acknowledge the Dr.

De Lannoy (Professor at Ghent University), Dr. Reichle (research physical scientist at Goddard Space Flight Center, NASA), and Dr. Lievens (postdoctoral researcher in Ghent University), who have been collaborating with me throughout my Ph.D journey. It is a great experience collaborating with these valuable researchers so that I can better learn the true value of collaboration as well as extend my research background.

I also want to mention about my colleagues at the University of Maryland as well as Sungkyunkwan University in Korea. I want to express my thankfulness to Gaohong Yin and Jawaria A. Ahmad, who started the graduate program the same year as me and provided me their most heartfelt support. I also want to mention Dr. Yonghwan Kwon, Lizhao Wang, Dr. Yuan Xue, Jing Wang, Dr. Lu Liu, and Elizabeth Megan Ryan who gave strong support to me. I would like to thank Sachraa Borjigan for helping me enrich my graduate life in the United States. Furthermore, I would love to mention Dr. Minha Choi, M.S. advisor in Sungkyunkwan University, Dr. Jongjin Baik and Dr. Chanyang Sur, and all ERSL lab members who have always been my solid support.

Last but not least, I owe my greatest and deepest thanks to my family - my mother, father, and sister who are always strong supporters for my life and pray for my success regardless of physical distance. I am proud of being my parent's son and appreciate them for being with me. Especially, I would love to mention my father, Dr. Jungkyoo Park, professor in Department of Civil Engineering at Daejeon Institute of Science and Technology Korea. He gave me his warm heart and shared his research experiences as well as insights with me, which leads me one step forward

in my research.

The completion of my Ph.D degree is valuable, but it does not signify the end. Instead, it symbolizes the beginning of a new future with goals, visions, and passions for what I have learned throughout my Ph.D journey. I wish to have chance to look back on this page after achieving of my ultimate goal of an academic career.

Table of Contents

List of Tables

List of Figures

List of Abbreviations

T_b	Brightness temperature
σ^0	backscatter observation
AMSR-E	Advanced Microwave Scanning Radiometer - the Earth Observing System
AMW	Active Microwave
ANN	Artificial Neural Network
DA	Data Assimilation
EASE-Grid	Equal Area Scable Earth Grid
ECMWF	European Centre for Medium-Range Weather Forecasts
EnFK	Ensemble Kalman Filter
ESA	European Space Agency
GEOS	Goddard Earth Observing System Model
GRDC	Global Runoff Data Center
GSOD	Global Surface Summary of the Day
LSM	Land Surface Model
MERRA	Modern-Era Retrospective Analysis for Researches and Application
ML	Machine Learning
Noah-MP	Noah-Multiparameterization
PMW	Passive Microwave
RFI	Radio Frequency Interface
RMSE	Root mean square error
RTM	Radiative Transfer Model
SAR	Synthetic Aperture Radar
SCA	Snow Covered Area
SCAN	Soil Climate Analysis Network
SLWC	Snow liquid water content
SMAP	Soil Moisture Active Passive
SMOS	Soil Moisture and Ocean Salinity
SNOTEL	Snowpack Telemetry
SSM/I	Special sensor Microwave Imager
SVM	Support Vector Machine
SWE	Snow Water Equivalent
MERRA	Modern-Era Retrospective analysis for Research Application
NASA	National Aeronautics and Space Administration
USDA	United States Department of Agriculture
ubRMSE	Unbiased root mean square error
USCRN	U.S. Climate Reference Network

Chapter 1: Introduction

1.1 Terrestrial Hydrological Cycle

The terrestrial water and energy cycles play a crucial role in understanding the complicated interaction between the land surface and atmosphere [221]. Understanding the water and energy cycles leads to improved knowledge of available water resources for human beings as well as ecosystems.

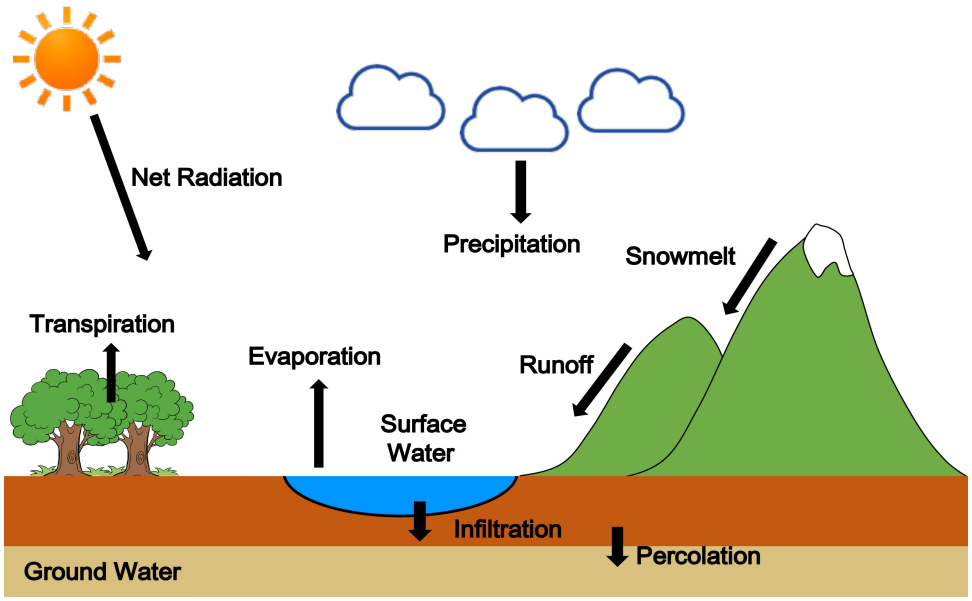

Figure 1.1: Schematic of hydrological cycle.

The water cycle is composed of different hydro-meteorological variables such as precipitation, evapotranspiration, soil moisture, snow, and runoff (Figure 1.1).

Among these variables, both soil moisture and snow are regarded as important variables to estimate or predict the seasonal streamflow [113]. Soil moisture is defined as a water stored in the soil above the water table [24]. Snow has been known as "water tower" as it stores winter precipitation and discharges it through snowmelt during springtime [125]. It supplies freshwater to more than 1.2 billion people (approximately one-sixth of the world's population) for agricultural and human usage [13,20,197]. Seasonal variation of both soil moisture and snow directly influence to the runoff. Snowmelt during the springtime significantly increases streamflow, which influences the terrestrial hydrological cycle. In case of soil moisture, it directly influences the partitioning of surface energy fluxes (latent heat and sensible heat fluxes) as well as precipitation fluxes, and in turn, exerts a first-order control on streamflow [72]. More specifically, when the intensity of precipitation and snowfall exceeds the infiltration capacity during saturated soil moisture conditions, it leads to the generation the surface runoff [196, 229].

1.1.1 Measurement of Terrestrial Hydrologic Cycle

In order to measure these hydro-meteorological variables, ground-based networks (e.g., Soil Climate Analysis Network [SCAN], Snowpack Telemetry [SNOTEL], Global Surface Summary of the Day [GSOD], and FLUXNET) have been extensively utilized with an advantage of direct quantification and high accuracy at the point-scale, which leads to the application of ground-based measurements to help evaluate hydrologic states estimated from satellite-based retrievals as well as from

land surface models [19, 25, 38, 43, 59, 135, 137, 193]. However, ground-based measurements are limited in terms of spatio-temporal coverage of hydro-meteorological variables at all locations in space and time. More specifically, the limited spatial footprint and sparse and/or uneven distribution of ground-based stations makes it difficult to accurately discern the spatial variation of hydro-meteorological variables. As an alternative, remote sensing observations are a feasible option to discern the spatio-temporal variations of hydro-meteorological variables over large areas without direct physical contact.

1.2 Microwave Remote Sensing Observations

In recent decades, satellite observations have been regarded as a vital information source to capture the spatio-temporal variation of land surface state and fluxes, which leads to their wide application across different hydrological fields [184, 201]. Satellite observations provide complete global coverage that helps overcome many of the sparsity issues that plague ground-based observational networks. Satellite observations can be subdivided into different frequencies (e.g., visible, infrared, and microwave) depending on the range of wavelength, λ, within the electromagnetic spectrum. Among the different types of observations, the microwave portion (1 mm$\leq \lambda \leq$ 1 m) of the spectrum offers tremendous potential for monitoring several hydro-meteorological variables including land surface temperature [94, 143], precipitation [99, 103], soil moisture [156, 214], and terrestrial snow [33, 106, 200]. Compared with the visible and infrared spectrums, microwave (MW) observations have a rel-

atively long wavelength that is effectively transparent to atmospheric conditions (e.g., cloud cover and dust), hence, can view more of the terrestrial environment as compared to relatively shorter wavelengths such as visible or thermal infrared. In addition, water molecules are highly interactive with MW photons, which can be exploited for hydrological research applications.

MW remote sensing sensors can be classified into passive (e.g., radiometers) and active (e.g., radars) observations based on the type of instrument [211]. Passive microwave (PMW) sensors measure the naturally emitted radiance from the environment, including the land surface. This observational variable is commonly provided as a brightness temperature. Brightness temperature (T_b) is defined as the equivalent temperature of thermally emitted microwave radiation from the object [90] and is computed as the physical temperature times the emissivity. In terms of active microwave (AMW), the sensor sends out a microwave pulse and measures the returning signal from the measured object (e.g., land surface). This observational variable is commonly returned to as the backscatter coefficient (σ^0). The underlying principle for using MW observations to study hydrological variables is based on the different electromagnetic response depending on the dielectric properties of the surface [12]. Due to the strong interaction of MW radiation (within a specific portion of the MW spectrum), the presence or absence of water is often a first-order control on the electromagnetic response of that MW radiation, be it passive or active in nature.

1.3 Land Surface Modeling

A land surface model (LSM) is another option to overcoming the spatio-temporal limitations of ground-based measurements. A LSM yields estimates of the water and energy fluxes at the land surface across various spatial and temporal scales by solving the physical equations of water and energy conservation related to complex land-atmosphere interactions and near-surface boundary conditions [68]. Many LSMs have been developed and utilized in hydrology including the Community Land Model (CLM; [46]), Mosaic Land Surface Model [114], Variable Infiltration Capacity (VIC; [130]), Joint UK Land Environment Simulator (JULES; [16]), and NOAH-Multiparameterization (NOAH-MP; [154]). Land surface estimates from LSMs has been extensively evaluated by comparing against ground-based measurements across the globe (e.g., [19,25,135,193]). Moreover, LSM outputs can be utilized for the purpose of evaluating remote sensing-based hydrometeorological variables [63, 167, 193]. However, hydrological states estimated from LSMs contain their own inherent uncertainties triggered from the different model parameterization schemes, model boundary conditions, and initial conditions [49, 176].

1.4 Data Assimilation Framework

Data assimilation (DA) is defined as a series of statistical algorithms that jointly use the theoretical (*a priori*) knowledge of the system model along with observations (or retrievals) in order to improve the knowledge of the past, present,

and future system states [175]. DA has been widely applied in hydrological fields due to the limitation in collecting high-quality fluxes from the hydrological cycle over extensive areas [144]. Estimates of hydrological states from a land surface (geophysical) model have advantages in providing spatio-temporal variations in each of the states while measurements generally provides less-biased information than the model or remote sensing-based products alone. Thus, the main goal of DA is to produce optimal estimates of geophysical variables that are superior to both model-alone estimates and remote sensing observations [144].

A DA framework can be divided into two general categories: variational data assimilation and sequential data assimilation. The main difference between variational and sequential data assimilation is the length of assimilation window: variational data assimilation (e.g., 3D-var and 4D-Var) fits the dynamic model with all available observations during a period of interest while sequential data assimilation (e.g., Kalman-type filters) updates the state at each observation time (a.k.a., on-line approach) [151]. In this dissertation, the focus is on the sequential data assimilation based on the advantage of relatively lower computational expense and the flexibility to couple hydrologic models with comparable or better accuracy than variational data assimilation [198].

Typical examples of sequential data assimilation include the Kalman filter, extended Kalman filter, and ensemble Kalman filter (EnKF) [71]. EnKF is a classical sequential data assimilation frameworks that implements a finite number of ensemble replicates to serve as a low-dimensional approximation of the conditional probability density function (PDF) of state error covariance using a Monte Carlo approach [71].

The general idea of the EnKF is illustrated in Figure 1.2.

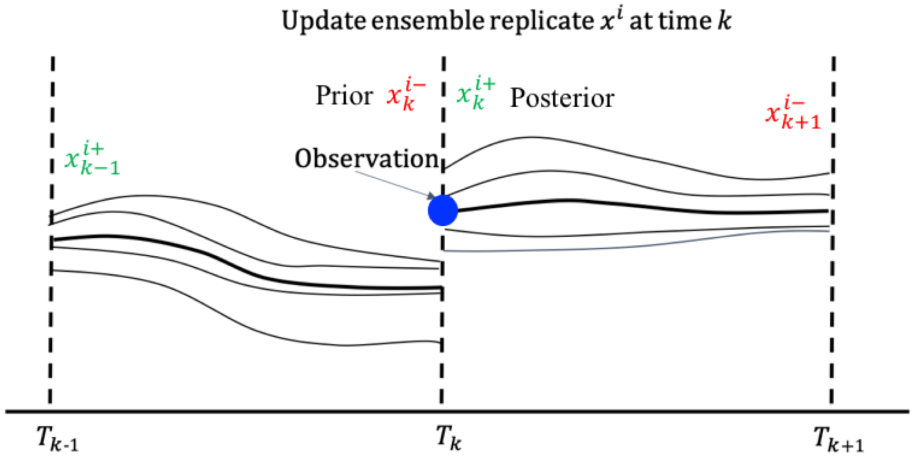

Figure 1.2: Schematic of the ensemble Kalman filter (EnKF).

As part of the the EnKF routine, ensemble replicates are propagated in time and updates of model states are determined by the mean and spread of the ensemble that approximates the state distribution. The use of ensemble replicates has an advantage in reducing the problem dimension using a low-rank approximation of the error covariance matrix and by reducing the associated computational expense [71]. The update and propagation of the EnKF is processed with a relatively small number of ensembles, which serves as a low-dimensional approximation of the conditional probability density function of the state error covariance matrix. Moreover, the EnKF does not require the underlying assumption of standard Kalman filter, which is limited in application only to linear models with assumption of mutually independent, Gaussian errors.

The EnKF consists of various components including the forward model (a.k.a., state system), state and observation matrices, model and observation error terms,

and the observation operator (Figure 1.3). Among these components, the observation operator is regarded as one of the most essential components. The main role of the observation operator is to bridge the model state space and observation space. It significantly influences the performance of the EnKF as it is highly connected to the determination of the amount of update as well as the error characterization in the EnKF. Detailed formulation and description of the EnKF is provided in Section 4.2.3.

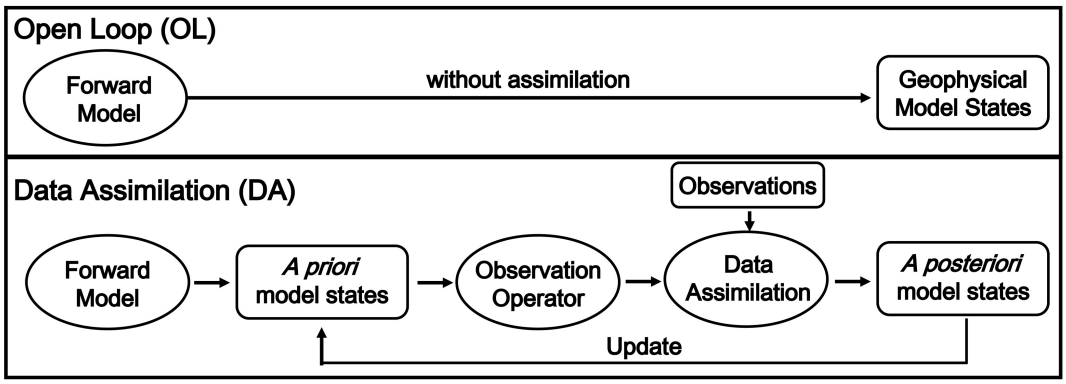

Figure 1.3: General schematic of the Open Loop (OL; model-only simulation) and data assimilation procedures.

1.5 Methodological Review of Soil Moisture

1.5.1 Remote Sensing of Soil Moisture

Emitted MW radiation from the soil surface is sensitive to various traits of the soil such as surface roughness, soil texture, vegetation cover, and moisture content [122, 155]. Among these components, soil moisture content at the soil surface is one of the crucial components influencing the different electromagnetic response. In the

lower portion of the MW spectrum (e.g., 3 cm $\leq \lambda \leq$ 30 cm), the dielectric constant of water and dry soil is known as 80 and 3.5, respectively [155]. This difference leads to differences in the emissivities between dry and wet soil (approximately 0.6 and 0.95, respectively), and hence, results in significant differences in T_b depending, in part, on the amount of soil moisture present [183].

Among the wide spectrum of microwave frequencies, wavelengths longer than 10 cm have been applied for retrieving soil moisture as a longer wavelength minimizes the effect of vegetation and surface roughness on T_b [163]. For example, several space-borne L-band radiometers have been successfully launched in order to retrieve soil moisture. In November 2010, the Soil Moisture and Ocean Salinity (SMOS) mission was launched by the European Space Agency (ESA) with a primary objective of monitoring global soil moisture and sea surface salinity [109, 110]. SMOS retrieves soil moisture every three days with spatial resolution ranged from 27 km to 55 km.

The U.S. National Aeronautics and Space Administration (NASA) launched the Soil Moisture Active Passive (SMAP) mission at 31 January 2015 in order to monitor the surface soil moisture and freeze/thaw status using an L-band radiometer, which provides a spatial and temporal resolution of $\sim$10 km and $\sim$3 days, respectively [69]. One of the main differences between SMOS and SMAP is that the former measures T_b at a single incidence angle while the latter uses the T_b observed at various incidence angles.

SMOS and SMAP soil moisture have been extensively evaluated across the globe and have shown reasonable agreement with the ground-based soil moisture

observations [43, 101, 137]. Jackson et al. [101] compared the soil moisture retrieved from SMOS and the Advanced Microwave Scanning Radiometer for the Earth Observing System (AMSR-E) against the in-situ surface ($\sim$ 5 cm) soil moisture observations from four experimental watersheds established by United States Department of Agriculture (USDA). Results showed that SMOS demonstrated better correlation coefficient (R) and root mean square error (RMSE) than the AMSR-E observations. In general, R and RMSE ranged from 0.7 to 0.8 and 0.030 m^3m^{-3} to 0.049 m^3m^{-3} for the SMOS soil moisture product. Collow et al. [43] also evaluated the soil moisture retrieved from SMOS by comparing with multiple in-situ observational networks (e.g., U.S Climate Reference Network (USCRN), SCAN, Oklahoma Mesonet, and Cosmic Ray) surface soil moisture observations ($\sim$ 5 cm) over the Great Plains of the United States. Statistical comparisons showed that the R ranged from 0.5 to 0.9 while SMOS soil moisture yielded a dry bias over the study area. Ma et al. [137] assessed the soil moisture from SMAP, SMOS, AMSR2, and ESA Climate Change Initiative (CCI) products across the globe through comparison with soil moisture from several ground-based networks. The results confirmed that SMOS and SMAP products showed superior statistical performance in most of the regions with R higher than 0.72, in general. In terms of bias and unbiased RMSE, SMAP showed better agreement with ground-based observation than SMOS in most regions. However, soil moisture retrieval via L-band radiometer images still contains uncertainties triggered by various parameters such as surface roughness, soil texture, and vegetation parameters (e.g., vegetation optical depth) and other environmental conditions (e.g., precipitation) [31, 39]

1.5.2 Data Assimilation of Soil Moisture

Another method to estimate the soil moisture is to implement the L-band MW observations into land surface models through a data assimilation (DA) framework. Typically, a radiative transfer model (RTM) is implemented as the observation operator in DA framework [29, 52, 53, 132]. The RTM is a physically-based model that accounts for the interactions among land surface, vegetation, and atmosphere states by prescribing specific process-based equations to the various components including dielectric properties of the land surface, surface roughness, and microwave emission and scattering by vegetation and near-surface soil [153, 159]. Examples of commonly-used RTMs include the L-band Microwave Emission of the Biosphere (L-MEB; [217]), Land Parameter Retrieval Model (LPRM; [158]), Land Surface Microwave Emission Model (LSMEM; [64]), and the Community Microwave Modeling Platform (CMEM; [55]).

Prior to conducting DA, previous research has evaluated the capability of the RTM to calculate accurate T_b so that it can adequately serve as observation operator in DA. Pellarin et al. [161] used the L-MEB model to generate L-band T_b predictions by employing land surface estimates from the Interactions between Soil, Biosphere, and Atmosphere (ISBA) model using atmospheric forcings from the International Satellite Land Surface Climatology Project Initiative I (ISLSCP I) and soil and vegetation characteristics from ECOCLIMAP. Drusch et al. [65] used the CMEM model to calculate the L-band T_b over the globe with the European Centre for Medium-Range Weather Forecasts (ECMWF) reanalysis datasets, vegetation information

from ECOCLIMAP, and soil texture and density from Food and Agricultural Organization (FAO). CMEM-based T_b was evaluated through the comparison against the Skylab S-194 T_b observations from 1990 to 2000 across North America and South America. This study employed 10 different calibration schemes for the RTM parameters such as surface roughness and vegetation-related parameters. The results confirmed that the overall domain-averaged biases for North America and South America were revealed as 10.7 K and 9.8 K, respectively. De Lannoy et al. [53] coupled a zero-order tau-omega RTM into the NASA Goddard Earth Observing System (GEOS) Catchment Land Surface Model (Koster et al. [115]) to compute L-band T_b worldwide. This paper utilized two different schemes in terms of dealing with various RTM parameters: 1) look-up table based parameterization and 2) calibration of parameters with SMOS T_b observation from July 2011 to July 2012 using a particle swarm optimization scheme, a metaheuristic optimization scheme implemented with swarms of different parameter values to solve complex problem [48]. Evaluation of RTM-based T_b with SMOS T_b observations that were not used for calibration (e.g., July 2010 to July 2011) confirmed that the global mean absolute bias of T_b calculated without calibration was revealed as 7.1 K. However, RTM-derived T_b with the SMOS calibration schemes showed significant improvement with a global average of absolute bias as 2.7 K.

The aforementioned studies showed the capability of using a RTM to produce accurate T_b estimates. Soil moisture DA was then conducted by employing the RTM to map the geophyiscal states (e.g., soil temperature, soil moisture, and vegetation water content) from the LSMs into observation space (i.e., T_b). De Lannoy and

Reichle [52] assimilated SMOS T_b observations into Catchment Land Surface Model (herein referred to as Catchment) coupled to a RTM using an ensemble Kalman Filter (EnKF) to improve soil moisture estimates across the North America. The RTM uses the land surface estimates computed from Catchment using boundary conditions provided by the Modern-Era Retrospective Analysis for Research and Application (MERRA) product [177]. In addition, RTM parameters were calibrated with SMOS v620 T_b observations using a similar scheme as conducted in De Lannoy et al. [53]. Soil moisture from the Open Loop (i.e., model-only simulation) and assimilated soil moisture were compared against in-situ measurements from the SCAN and US Climate Reference Network (USCRN). The results confirmed that approximately 80% and 65% of improvement was observed in the surface soil moisture and root-zone soil moisture estimates, respectively, with unbiased root mean square difference ranging from -0.004 m^3/m^3 to -0.001 m^3/m^3. Hostache et al. [96] assimilated SMOS T_b observations (from 2010 to 2015) into the SUPERFLEX hydrological model [73] by implementing the CMEM version 5.1 RTM to improve the overall accuracy of soil moisture across the Murray-Darling basin in Australia. Hostache et al. [96] implemented the local ensemble transformation Kalman filter for data assimilation. For the operation of the SUPERFLEX model, the ERA-Interim reanalysis datasets were used as boundary conditions and vegetation information from ECOCLIMAP was employed. Comparison of the Open Loop (OL) and DA-based soil moisture conducted with ground-based soil moisture observation revealed that updated soil moisture via DA showed improved statistics (e.g., correlation coefficient, root mean square deviation [RMSD], and unbiased RMSD) over the OL results. Furthermore,

the correlation coefficient was improved in both surface soil moisture (from 0.78 to 0.80) and root-zone soil moisture (from 0.70 to 0.73).

1.6 Methodological Review of Snow

1.6.1 Remote Sensing of Snow

Passive microwave observations have also been used to characterize snow mass using T_b over snow-covered terrain as snow mass is closely related to the behavior of emitted microwave radiation from the terrestrial surface [104]. Namely, T_b over snow-covered terrain is highly influenced by the physical properties of snowpack such as snow depth, snow density, snow stratigraphy, snow grain size, snow grain shape, and liquid water content. Retrieval of snow water equivalent (SWE) and snow depth from PMW generally relies on the spectral gradient as a difference between two or more brightness temperatures (T_b) at two or more different frequencies. A relatively low frequency (18-19 GHz) is transparent in the snowpack and emitted radiation reaches the radiometer while a higher frequency (36-37 GHz) undergoes more scattering, which reduces the arrival of emitted radiation to radiometer [42]. These aforementioned first-order physics lead to developing the simple quasi-linear algorithm for SWE retrieval using various PMW imagery such as Scanning Multi-channel Microwave Radiometer (SMMR) [33], Special Sensor Microwave Imager (SSM/I) [78], AMSR-E [105].

Given the plethora of PMW-based SWE products, many researchers have evaluated the accuracy of these SWE products through a comparison with ground-based

measurements [40, 59, 202]. These papers demonstrated that even though PMW imagery has a relatively coarser spatial resolution, SWE from PMW retrievals showed reasonable performance in comparison with ground-based measurements as well as model-based estimates. At the same time, however, it also showed significant uncertainties resulting from complex snow stratigraphy (e.g., deep snow, depth hoar, snow grain size, and internal ice crusts) as well as external conditions (e.g., densely-vegetated regions or sub-grid scale lakes) [42, 59, 78, 202].

AMW has been regarded as an alternative option to retrieve snowpack information (e.g., SWE, snow depth, and snow wetness) through measuring the intensity of the returned signal generated by a radar (a.k.a., backscatter). Spaceborne synthetic aperture radar (SAR) is one type of AMW remote sensing based on an imaging radar onboard on the satellite platform with side-looking geometry [147]. SAR measures the backscatter from a land surface; backscatter is dependent on the dielectric properties of the snow-covered terrain as well as the surface roughness and the geometry of scattering snow media [141, 204, 212]. Figure 1.4 illustrates the typical propagation of microwave photons through a snowpack using an active microwave sensor.

In general, total backscatter from snow-covered terrain (σ^0_{total}) can be observed through the sum of the following three components: 1) backscatter from the air-snow interface, σ^0_{air}, 2) volume scattering within the snowpack, σ^0_{snow}, and 3) backscatter at the underlying snow-land interface, σ^0_{ground}. That is, σ_{total} is computed as:

$$\sigma^0_{total} = \sigma^0_{air} + \sigma^0_{snow} + \sigma^0_{ground} \tag{1.1}$$

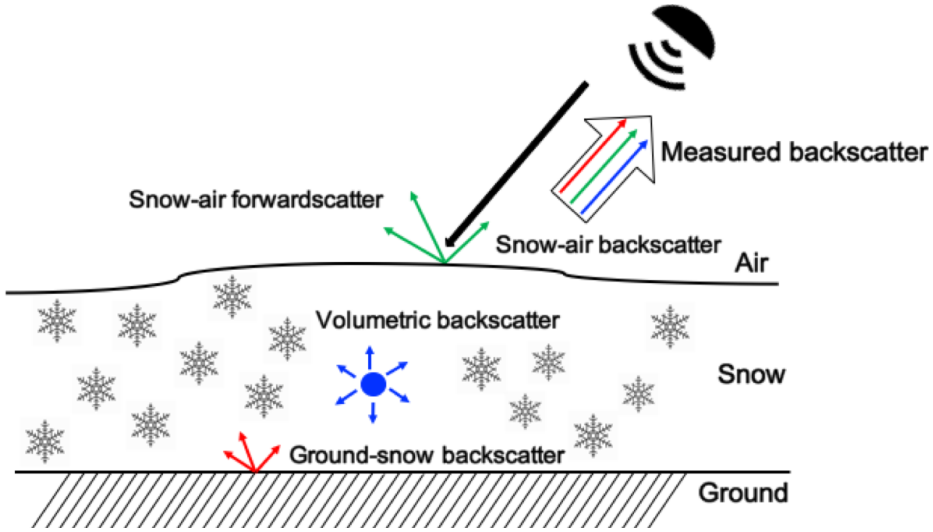

Figure 1.4: Description of scattering mechanisms over snow-covered terrain (based on the [204]).

Radar backscatter over a snow-covered surface is linked to several parameters, including viewing characteristics of the sensor (e.g., frequency, polarization, and geometry), snow structure (e.g., liquid water content, snow grain size, snow grain shape, and snow stratification), and underlying soil (e.g., soil dielectric constant and surface roughness) [14]. For MW frequencies lower than L-band (1.25 GHz), σ^0_{snow} from within the snowpack is minimal as the snow grain size is much smaller than the L-band wavelength [188]. In contrast, the magnitude of σ^0_{snow}, as well as σ^0_{ground} are highly dependent on the dielectric properties of the snowpack at C-band (5.5 GHz) or higher frequencies [129, 188]. The incidence angle, defined as the angle between the incoming signal that is perpendicular to the surface, is another important component as it determines the path of the microwave photon inside the snowpack [14]. According to Snell's law, specifying the change in incidence angle depending on a change of medium, a large incidence angle at the snow-air interface

results in more refraction within the snow layer, which leads to a greater increase in backscatter as detected at the radar receiver [188].

The polarization, which represents the direction of transmission or reception of the electromagnetic wave, is also important in terms of characterizing the underlying snowpack. Polarization can be classified into linear, circular, or elliptical forms based on the amplitude and phase differences [4]. Each polarization can be classified into co-polarized (i.e., vertical transmit and vertical receive; σ^0_{VV}) and cross-polarized (i.e., vertical transmit and horizontal receive; σ^0_{VH}) forms depending on the direction of the transmitted and received signal. When the shape of the snow particle is spherical, the σ^0_{VV} is preferred for use in a snowpack retrieval due to the negligible backscatter in cross-polarization [14]. In reality, however, Yueh et al. [228] showed that σ^0_{VH} can also provide useful information when non-spherical snow particles or densely packed snow layer exists that cause multi-path backscatter. Nager et al. [150] also demonstrated that σ^0_{VH} can help discriminate between wet snow and snow-free condition with less angular dependence at a low incidence angle. However, the σ^0_{VH} at a high incidence angle contains non-negligible noise. Therefore, Nagler et al. [150] suggested the utilization of both σ^0_{VV} and σ^0_{VH} for snow retrievals using SAR.

Based on the fundamental electromagnetic theory that reflected on the backscatter from snow-covered terrain, a variety of different spaceborne SARs have been utilized for estimating snow cover extent, snow depth, and SWE. Table 1.1 summarizes the detailed specification of various spaceborne SAR systems widely used for retrieving snowpack information. SAR imagery has been primarily used to deter-

Table 1.1: Brief description of spaceborne SAR instruments.

Satellite	Frequency [GHz]	Polarization	Temporal Coverage
ERS-1/2	5.3	single	1991/07 $\sim$ 2011/04
RADARSAT-1	5.3	single	1993/11 $\sim$ 2013/03
RADARSAT-2	5.405	single & dual	2007/12 $\sim$ present
Envisat	5.331	single & dual	2002/08 $\sim$ 2010/10
TerraSAR-X	9.65	single & dual	2017/11 $\sim$ present
Sentinel-1A/B	5.405	single & dual	2014/03 $\sim$ present

mine snow cover area (SCA) based on a threshold detection algorithm. For example, Rott and Nagler [180] developed a snow mapping algorithm over mountain areas located in Austria using ERS-1 SAR data. This study proposed the threshold-based classification algorithm, which is based on the threshold calculated as the ratio of backscatter from wet snow cover versus that from snow-free conditions (a.k.a. reference image). When the ratio is less than the threshold value (defined as -3 dB via frequency distribution of the ratio at dry and wet snow surface) the specific area is classified as snow-covered terrain. The application of this algorithm showed reasonable accuracy at classifying wet snow but showed poorer performance during dry snow conditions. Similar research was conducted in the Eastern Alps of Austria using ERS-1/2 and RADARSAT SAR data [148]. They used a similar algorithm introduced in Rott and Nagler [180] except that dry snow at higher elevations was excluded by using a digital elevation map. Comparison of SAR-based snow cover retrieval with Landsat-5 Thematic Mapper showed overall pixel-by-pixel agreement ranged from 81 to 85% while SAR-based snow cover underestimates coverage at the edge of the snowpack. Pivot [166] used RADARSAT and ERS-2 datasets to characterize the snow-covered area in the northern Hudson Bay Lowlands in Canada

during the winter seasons of 1997 and 1998 via comparison with ground-based observations. Backscatter increased with respect to SWE when frost penetrated the first 20 cm of the surface soil while backscatter showed no significant change at locations where backscatter is dominated by scattering at the snow-land interface. Nagler et al. [150] also used a threshold-based segmentation to build snow cover maps based on Sentinel-1 observations over Iceland and the European Alps. Their study used the ratio of snow-covered and snow-free backscatter observation for both co- and cross-polarization separately that is transformed to the unit of dB. Then, these two ratios were combined using a weighting factor, which was a function of the local incidence angle. These calculations lead to the threshold of -2 dB for classifying snow-free and snow-covered regions. Evaluation of Sentinel-1 snow maps using Landsat-7 Enhanced Thematic Mapper (ETM) normalized snow difference index (NDSI) images showed the overall pixel-by-pixel possibility of detection ranged from 0.95 to 0.97. However, Nagler et al. [150] mentioned the presence of significant error and uncertainty in Sentinel-1 snow maps in regions of dense forest as scattering is predominated by the canopy rather than the underlying snow. Hence, rather than using threshold-based approaches, Singh et al. [191] introduced the utilization of a polarization factor, which is the ratio of backscatter from the cross-polarized and co-polarized observations collected by the Advanced Land Observation Satellite (ALOS)-Phased Array-Type L-Band Synthetic Aperture Radar (PARSAR). Singh et al. [191] utilized a supervised classification routine to extract the wet snow regions based on a polarization factor. Results revealed that the newly proposed classification scheme showed better accuracy than other wet snow mapping algorithms when

compared with snow cover maps obtained via optical remote sensing.

There are relatively few studies focused on the estimation of SWE or snow depth using SAR due to the difficulty in capturing the complex scattering mechanisms over snow-covered terrain [126]. Bernier et al. [15] estimated SWE using RADARSAT images during the winter of 1998 and 1999 at La Grande River watershed in eastern Canada. The SWE retrieval algorithm can be divided into two steps: 1) estimate the thermal resistance of the snowpack layer via linear regression with the backscatter ratio of winter (snow-covered) versus fall (snow-free) observations and 2) estimate SWE by multiplying the thermal resistance with a parameter that is a function of mean snow density. Mean SWE from RADARSAT at the watershed scale was similar to that from interpolated SWE maps determined using ground-based measurements. However, point-scale comparisons of RADARSAT-based SWE with ground-based measurements showed a clear overestimation at the lowest and highest incidence angles. Instead of using a linear relationship to obtain SWE, Li et al. [126] estimated snow depth and SWE for dry snow based on SAR interferometry (i.e., synthetic aperture radar interferometry (InSAR) and differential SAR interferometry (DInSAR)) that are based on the phase difference at the air-snow interface, which is influenced by the refraction of the MW radiation penetrating the snowpack layer. This algorithm was applied using Envisat C-band Advanced Synthetic Aperture Radar (ASAR) over the Manas River Basin in China. Evaluation of SWE estimates using Envisat suggests the potential to estimate snow depth and SWE even though uncertainties related to terrain characteristics as well as incidence angle effect still need to be addressed. Conde et al. [44] utilized a similar

approach as Li et al. [126] to obtain the temporal variation of SWE using Sentinel-1 datasets over northeastern Finland from December 29, 2015 to January 22, 2016. Comparison with ground-based SWE measurements showed good accuracy in terms of root mean square error (∼6 mm) but contained uncertainties associated with the presence of wet snow as well as the overlying forest cover.

1.6.2 Snow Estimation using Machine Learning

Machine learning (ML) is defined as an algorithm that can learn a highly-sophisticated relationship between inputs and outputs for a given physical system based on statistical inference [127]. The term learning (a.k.a., training) suggests an optimization procedure that reduces the differences between the observations and the model estimates [195]. ML has advantages in improving computational efficiency by replacing the time-consuming human activity of discovering regularities in the training data by using automated techniques [123]. In this regard, it has been widely applied across a wide range of scientific and engineering fields in the forms of prediction, classification, and pattern recognition [77]. Examples of ML techniques include decision trees, random forests, artificial neural networks (ANNs), and support vector machines (SVMs).

1.6.2.1 ML and Snow Cover Extent

ML techniques have also been applied to snow-related studies. In the context of snow cover mapping, optical remote sensing has been widely used with ML tech-

niques to improve the accuracy of snow-covered area mapping. Simpson and McIntire [190] used a feed-forward recurrent ANN to discriminate snow-covered land from clouds and snow-free land pixels using Advanced Very High Resolution Radiometer (AVHRR) and Geostationary Observing Environmental Satellite (GOES) system. Validation of the snow cover retrieval using SNOTEL measurements showed the high classification accuracy (ranged from 94% to 97%) while it showed significant uncertainty in forest-covered regions with complex terrain. Similarly, Dobreva and Klein [61] applied a multi-layer, feed-forward ANN to estimate the snow cover fraction (SCF) using Moderate Resolution Imaging Spectroradiometer (MODIS) surface reflectances, NDSI, Normalized Difference Vegetation Index (NDVI), and IGBP land cover over North America for the years 2000 to 2003. The comparison of ANN-based and original MOD10 SCF maps with Landsat ETM+ binary snow cover map revealed that both products showed reasonable accuracy with a coefficient of determination ranging from 0.79 to 0.97 and RMSE between 0.12% to 0.23% across the different land cover types. Most notably, the ANN-based SCF map showed relatively higher accuracy than the MOD10 product in deciduous and mixed agriculture and forest land cover types.

1.6.2.2 ML and Snow Mass Estimation

In the case of retrieving SWE and snow depth, PMW datasets have also been used as inputs to ML techniques [34, 47, 208]. Cao et al. [27] utilized an ANN with Bayesian regularization to estimate the snow depth using AMSR-E T_b from 2002 to

2003 over the Qinghai-Tibet Plateau, Tibet. Inputs to the ANN include four T_bs at both vertical and horizontal polarization at either 18.7 GHz or 36.5 GHz. Split samples of the ground-based snow depth measurements were used as training targets and the other subset used for validation. Evaluation of the ANN-based snow depth retrieval was performed with the comparison of snow depth estimated from the [33] algorithm known as the Spectral Polarization Difference algorithm (SPD; [7]) along with a temperature gradient algorithm (i.e., TGI; [120]). The results showed that ANN-based snow depth retrievals yielded reasonable statistics with the highest correlation coefficient and lowest mean square error when compared to ground-based measurements. Tedesco et al. [203] also utilized an ANN to invert SSM/I T_b into SWE and snow depth estimates during the years 1996 to 1999 at 12 different test sites across Finland. T_bs observed at 19 GHz and 37 GHz at both polarizations were selected as inputs, and then ground-based SWE and snow depth measurements were selected as training targets. ANN-based SWE and snow depth were compared among three existing retrieval algorithms (e.g., SPD, Helsinki University of Technology (HUT), and Chang et al. [33] model) against ground-based measurements. The results revealed that ANN-based SWE and snow depth estimates yielded the best statistical results with the lowest root mean square error and the highest coefficient of determination. However, Tedesco et al. [203] highlighted limitations regarding the low applicability to regions without ground-based measurements because successful training of ML techniques is severely limited in data-sparse regions. Xiao et al. [223] introduced support vector machine regression to develop the snow depth retrieval algorithm using T_b from SSM/I and Special Sensor Microwave Im-

ager/Sounder (SSMIS) for a 25 year period (1992-2016) across Eurasia. Utilizing T_bs at different frequencies, other parameters such as latitude, longitude, land cover type, elevation, and day of the year were also selected as input datasets for SVM. The SVM-based snow depth estimates were compared with algorithms introduced in Chang et al. [33], the SPD algorithm, and ANN-based snow depth [203]. Results revealed that SVM-based snow depth yielded the highest correlation coefficient with the lowest root mean square error when compared to ground-based measurements. Overall, the SVM snow depth retrieval showed advantages in improving the accuracy of estimated snow depth, but deficiencies including the influence of terrain and vegetation still need to be addressed.

Rather than estimating SWE or snow depth dependent on point-based measurements as the training dataset, T_b over the snow-covered terrain can be used in conjunction with ML techniques without the need for ground-based information. Forman et al. [75] predicted PMW T_bs with an ANN over snow-covered terrain across North America during the period 2002 to 2011. Inputs to the ANN included land surface geophysical variables relevant to define snowpack conditions using the NASA Catchment land surface model. The ANN was trained using the T_bs observed by AMSR-E at three different frequencies (10.65, 18.7, and 36.5 GHz) and two different polarization (horizontal and vertical). Validation of ANN-based T_bs was conducted by split-sample validation with AMSR-E T_bs that were *not* used for training as well as airborne-derived T_b suggested that ANN could reasonably estimate T_b during both snow accumulation and ablation phases. However, Forman et al. [75] highlighted ML limitations with respect to the condition of input and training datasets. For

example, the modeling of internal ice layers, snow grain shape, or snow grain size is not considered in Catchment while PMW T_b is modulated by such influences. Analogously, Forman and Reichle [74] utilized SVM regression to estimate the T_b over North America using the same inputs and training datasets as Forman et al. [75] and compared the feasibility of SVM and ANN in terms of T_b prediction. The results confirmed that T_b estimated from the SVM was unbiased with an anomaly R of 0.7 across the study area. The main reason for this phenomenon is that SVM is trained for each frequency and polarization with multiple tuning parameters while the ANN was trained with all frequency and polarization combinations simultaneously. Similar results could be found in Forman and Xue [77] that also used both ANN and SVM to predict the PMW T_b observed from SSM/I.

In the case of space-borne SAR, it has rarely been used in ML to estimate the snowpack conditions or snow mass even though AMW imagery provides relatively finer spatial resolution than PMW imagery. He et al. [92] examined the application of an SVM classifier to map snow cover information from the Radarsat-2 Polarimetric SAR datasets over the Tianshan mountains in China during snow accumulation and ablation period in 2013. Validation of the snow cover map with Gaofen-1 wide-field viewer data showed a mean pixel-by-pixel accuracy of 73.6% and 82.7% for snow accumulation and ablation period, respectively. Tsai et al. [207] used Sentinel-1 backscatter and ancillary datasets (e.g., topographic elevation information from Shuttle Radar Topography Mission [SRTM] and land cover information from the European Space Agency Climate Change Initiative) using a random forest (a.k.a., one type of an unsupervised machine learning algorithm) to classify the wet and dry

snow more efficiently. The training period was selected within the first hydrological year (August 2016 to July 2017) and predicted snow classification was validated during the second hydrological year (August 2017 to July 2018). Validation of ML-based snow classification with snow cover information retrieved from Landsat 8 (suggested in Nagler et al. [150]) showed overall pixel-by-pixel comparison ranged from 75% to 90% over the majority of land cover types except for grasslands.

1.6.3 Snow Mass Estimation using Data Assimilation

1.6.3.1 Snow Covered Area Assimilation to Update Snow Mass

Retrieved snow cover information from satellite imagery has been utilized to update the state variables estimated from hydrological models through various DA frameworks, including simple direct insertion, variational approaches, and Kalman-filter based approaches [49]. A number of snowpack-related variables such as SCA, SCF, SWE, and snow depth from in-situ measurements or satellite retrievals have been applied in a DA framework in different forms. Rodell and Houser [178] used direct insertion to assimilate MODIS snow cover retrievals into the Mosaic LSM [114] in order to improve the accuracy of snow-water storage. Roy et al. [181] also integrated snow cover information from MODIS and the NOAA Interactive Multisensor Snow and Ice Mapping System (IMS) into the Modéle Hydrologique Simplifié à l'Extême (MOHYSE) hydrological model using the direct-insertion method in order to improve simulated springtime streamflow in Quebec, Canada. They applied a simple SWE threshold rule: when the model (observation) has more snow

than the observation (model), the former was fixed to the threshold. Evaluation of simulated discharge with ground- and model-based discharge revealed a slight improvement in root mean square error while it did not show improvement in the Nash-Sutcliffe coefficient. Direct insertion has the advantage of simplicity but has significant limitations in the consideration of uncertainties in the observations or geophysical model [206].

As an alternative to direct insertion, Kalman-type filters, including the extended Kalman filter (EKF) and Ensemble Kalman filter (EnKF), have been employed. Andredis and Lettenmaier [3] used an EnKF with a snow depletion curve (serving as the observation operator by converting snow cover fraction into snow water equivalent) to assimilate MODIS snow cover information into the Variable Infiltration Capacity (VIC) model to improve the SWE from 1999 to 2003 across the Snake River basin in the United States. Evaluation of assimilated SWE against ground-based measurements revealed a slight improvement in correlation coefficient and root mean square error with the greatest level of improvement during the snow ablation season. Arsenault et al. [5] compared the ability of direct insertion versus an EnKF to assimilate MODIS SCF retrievals into the Community land surface model (CLM) to improve SWE estimates in Washington state and Colorado. Validation of assimilated SWE against the SNOTEL and National Weather Service Cooperative Observer Program (Co-op) network showed that direct insertion showed slight improvement at lower elevations while it disrupted the regional water mass balance. Alternatively, the EnKF showed good performance over high elevation areas with little violation in water mass balance. De Lannoy et al. [49] also used the EnKF

to assimilate AMSR-E SWE and MODIS snow cover retrievals into the Noah LSM over Northern Colorado from 2002 to 2010. The authors conducted several different experiments, including single sensor assimilation (e.g., AMSR-E SWE or MODIS snow cover only) and multi-sensor assimilation (e.g., with or without downscaling) using the AMSR-E SWE product. Validation of updated (posterior) product SWE and snow cover with ground-based measurements (i.e., SNOTEL and Co-op) revealed marginal improvements in terms of root mean square error and correlation coefficient when the snow was deep or the region was completely snow-covered. SCF assimilation improved the onset timing of snow season, but it did not significantly improve posterior SWE estimates.

1.6.3.2 SWE Assimilation to Update Snow Mass

As assimilation of snow cover information does not significantly improve the quality of SWE estimates, researchers have tried to directly use the SWE retrieved from PMW observations. Dong et al. [62] assimilated SWE retrievals from AMSR-E into a three-layer snow hydrology model using an extended Kalman filter and compared it with Open Loop (i.e., without assimilation) and in-situ measurements. Results showed that assimilated snow depth was superior in accuracy to model-only and satellite-based SWE. However, when the model-based SWE exhibited more than 100 mm at the beginning of the snow season, assimilated SWE did not show any improvement. Montero et al. [146] also assimilated the Satellite Application Facility on Support to Operational Hydrology and Water Management (H-SAF) SWE

retrievals into the Hydrologiska Byråns Vattenbalansavdelning (HBV) conceptual hydrological model [133] in order to improve model accuracy of streamflow. Assimilation was conducted using the Moving Horizon Estimation (MHE) technique, which is classified as a variational assimilation method, over Germany and Turkey during the period of 2010 to 2013. Assimilated SWE showed some improvement in terms of streamflow estimation while it also showed uncertainties related to wet snow conditions as well as to an accurate snow accumulation and ablation period as inferred from the satellite-based product.

After attempting to assimilate SWE retrievals derived from ΔT_b observations, researchers started to directly implement ΔT_b for assimilation as it is revealed as more efficient than utilizing PMW-based SWE retrievals [93]. Graf et al. [86] assimilated ΔT_b retrieved from AMSR-E T_b at 18.7 and 36.5 GHz with horizontal polarization into the Japanese Meteorological Agency (JMA) Simple Biosphere Model (SiB) model to improve the snow depth for the period of November 2002 to March 2003 over Eastern Siberia. Graf et al. [86] used the Microwave Emission Model Layered Snowpack (MEMLS) RTM as the observation operator to convert model states (i.e., snow depth) into observation space (i.e., T_b). The results confirmed that assimilated snow depth showed better performance than the Open Loop (OL) as well as the AMSR-E SWE retrievals. However, several sources of errors such as the lack of known snow grain size as well as model structure error in MEMLS still need to be addressed. Che et al. [36] assimilated ΔT_b between 18.7 and 36.5 GHz from AMSR-E into CLM using an EnKF to improve the accuracy of estimated snow depth over Eastern Siberia from October 2003 to April 2004. The DA framework

showed improvement in snow depth during the snow accumulation period. However, it contained significant uncertainties during the snow ablation period due to the presence of wet snow. Xue et al. [225] also conducted an assimilation experiment using AMSR-E T_b into the NASA Catchment model using an EnKF from 2002 to 2011 across North America. Even though the overall DA framework was similar to research discussed directly above, Xue et al. [225] used a SVM as the observation operator when mapping the model states into T_b space rather than a RTM as done in previous studies. Assimilated SWE and snow depth were compared with in-situ measurements as well as against reference datasets (e.g., Global Snow Monitoring for Climate Research [GlobSnow and Canadian Meteorological Centre [CMC] daily snow depth product). The assessment of assimilated SWE and snow depth showed slightly better statistical performance than the OL which resulted in the improvement of cumulative runoff.

1.6.3.3 SAR Assimilation to Update Snow Mass

Besides snow data assimilation using PMW imagery, SAR observations also have several advantages in terms of improving snowpack estimates given the quasi-independence with atmospheric conditions, high-spatial resolution, and sensitivity toward the presence of volumetric mediums on the land surface [164]. Despite these advantages, there are relatively few studies employing SAR observations into a DA framework to improve snowpack estimates. Nagler et al. [149] assimilated MODIS snow cover information and Envisat ASAR data into a snowmelt-runoff model in

Austrian Alps from 2005 to 2006. Assimilated runoff showed good agreement with ground-based measurements. This assimilation procedure updates the nominal SCA estimates by employing the interpolated weather station datasets at northern Finland from 2004 to 2006. Analysis of assimilated SCA through comparison with MODIS snow cover retrievals showed improvement in RMSE and R. When the forest cover is accounted for prior to assimilation, statistics of assimilated SCA showed more statistical improvement. Laojus et al. [136] improved the snow cover area mapping from RADARSAT through the weather station assimilation method, which is a simple method to update the snow cover area information using satellite-based and ground-based interpolated snow information.

1.7 Research Objectives and Science Questions

Throughout the vein of research introduced above, the potential of microwave observations to explore the soil moisture and snow mass information is demonstrated. At the same time, however, retrieval of soil moisture and snow mass information using microwave observations exhibited uncertainties with regards to vegetation, soil characteristics, and complicated snow stratification. This motivates the application of data assimilation to improve the accuracy of soil moisture and snow mass information. As a part of the data assimilation framework, radiative transfer models and machine learning techniques have been used as the observation operators in data assimilation frameworks with the benefit of providing reasonable estimates of microwave observations.

In response to the potential use of microwave observation to better inform soil moisture and snow mass estimates, the research presented below is intended to help address the overarching scientific question: **"Can radiative transfer model and machine learning techniques serve as effective observation operators in the assimilation of microwave observations into a land surface model to better characterize soil moisture and terrestrial snow mass?"** In order to address the scientific question, the following three specific scientific hypothesis will be addressed:

Scientific Hypothesis 1: A radiative transfer model can serve as an effective observation operator to improve soil moisture by reproducing accurate L-band T_b estimates.

Scientific Hypothesis 2: The accuracy of predicted C-band backscatter using a machine learning algorithm will be influenced by the consideration of first-order physics scattering mechanisms depending on snow conditions as well as the number of available datasets for both training targets and inputs.

Scientific Hypothesis 3: Inclusion of a machine learning algorithm as the observation operator into an advanced land surface model using an ensemble-based DA framework will improve the accuracy (and reduce the uncertainty) of modeled snow mass estimates.

1.8 Structure of Thesis

The overall dissertation is composed of five chapters. In Chapter 1, the importance of acquiring of soil moisture and snow mass information using different techniques (e.g., ground-based measurement, remote sensing, machine learning, and data assimilation) as well as a review of the current literature are discussed. It also outlines the overall objective and detailed scientific hypothesis of this research.

In Chapter 2, the capability of support vector regression is introduced, which is used as an observation operator in the snow DA framework as presented in Chapter 4. More specifically, SVMs were generated with additional physical constraints addressing first-order physics of electromagnetic responses for different snow conditions through considering the influence of training target sets, training window length, and snow wetness conditions. Chapter 2 outlines the integration of the fundamental concepts of scattering mechanisms within the snowpack into the SVM training and prediction procedure, which enhances the accuracy of predicted backscatter. Furthermore, it motivates the application of well-trained support vector regression into a snow DA framework. This chapter has been submitted to the IEEE Journal of Selected Topics in Applied Earth Observations and Remote Sensing entitled as "Prediction of active microwave backscatter over snow-covered terrain across Western Colorado using a land surface model and support vector machine regression".

In Chapter 3, a zero-order radiative transfer model (RTM) implemented into the NASA Goddard Earth Observing System (GEOS) was used to estimate L-band T_b across North America. For the operation of RTM, various RTM parameters (e.g.,

vegetation and surface roughness parameters) were calibrated based on multi-year SMOS observations. RTM-derived T_bs were then assessed through comparison with the daily T_b observations collected by the L-band radiometer onboard the Aquarius satellite. More specifically, RTM-derived T_bs were evaluated as a function of soil hydraulic parameters and vegetation types. The goal of this work was to verify the use of the RTM to estimate L-band T_bs in the context of soil moisture estimation so that Aquarius T_b observations could eventually be included in NASA's data stream to improve modeled surface soil and root zone soil moisture in GEOS-5. This chapter formed a manuscript entitled "Evaluation of GEOS-5 L-Band Microwave Brightness Temperature using Aquarius Observations over Non-Frozen Land across North America" which is in review with the Remote Sensing.

In Chapter 4, C-band backscatter observations from Sentinel-1 were integrated into the Noah-Multiparameterization (Noah-MP) land surface model using well-trained SVMs developed in Chapter 2 in conjunction with a one-dimensional ensemble Kalman filter (EnKF) in order to improve the accuracy of terrestrial snow mass estimates. Evaluation of the assimilation framework is conducted by comparing results from both the Open Loop (OL; model-only run without the benefit of C-band backscatter observations) and data assimilation (DA; model run after merging with C-band backscatter observations) results using in-situ measurements of snow water equivalent and snow depth collected across Western Colorado. The research presented in Chapter 4 is the first known attempt to merge C-band backscatter observations with a land surface model using a SVM as the observation operator for the purpose of improving the accuracy of modeled snow mass estimates. Part of

this chapter is under preparation for submission to a peer-reviewed journal.

Chapter 5 provides the overall conclusions and summary of key findings from the different experiments regarding improvements in soil moisture as well as snow mass information. Moreover, the implications and future directions of research based on these results is discussed, and the new and novel components of this research contributed to the hydrologic science community are also compiled and summarized.

Chapter 2: Prediction of Active Microwave Backscatter over Snow-covered Terrain across Western Colorado using a Land Surface Model and Support Vector Machine Regression

2.1 Overview

Previous research addressed the capability of machine learning (ML) algorithms (e.g., artificial neural network [ANN] and support vector machine regression [SVM]) to reproduce plausible space-borne passive microwave (PMW) T_b observations over snow-covered terrain [2, 74, 77]. In addition, follow-on studies [121, 224] revealed that a SVM can serve as an efficient observation operator to produce predicted PMW T_b as part of a data assimilation framework aimed to improve the snow mass estimates within a land surface model. For backscatter observations, however, ML has been widely utilized as a classifier (e.g., snow free versus snow-covered terrain and dry snow versus wet snow) rather than for backscatter prediction. Therefore, the primary objective of this chapter is to investigate the robustness of a SVM generated with the additional physical constraints addressing the first-order scattering mechanisms over snow-covered terrain in order to predict C-band backscatter as a function of geophysical inputs that reasonably represent the relevant characteristics

of the snowpack. More specifically, SVM prediction will be evaluated as a function of different training targets, training windows, and physical constraints regarding snow wetness. Section 2.2 provides the description of study area, data, and model while Section 2.3 describes the detailed methodological review of developing a physically-constrained SVM over snow-covered terrain. In Section 2.4, the evaluation of SVM prediction is performed based on different criteria (e.g., training targets, training windows, and snow wetness delineation) is described. Lastly, conclusions and a final discussion is presented in Section 2.5.

2.2 Study Area, Data, and Land Surface Model

2.2.1 Study Area

The study domain selected here is Western Colorado within the latitude of 36.875°N and 41.125°N and longitude of 104.375°W and 109.125°W (Fig. 2.1). The study area includes three national forests in the southern Rocky Mountains (i.e., San Juan [7.603 km^2], Rio Grande [7.527 km^2], and Grand Mesa [1.400 km^2]). The range of elevation for the selected study domain lies between 1314 m and 4125 m with over 60% of the total study area at elevations higher than 2250 m. The dominant forest cover in the study domain is lodgepole pine, classified as an evergreen conifer, according to the United States Forest Service forest type map (`https://data.fs.usda.gov/geodata/rastergateway/forest_type`). Annual meteorological characteristics of these regions suggest a wet, rainy season during the summer along with winter storms in high elevations starting from November

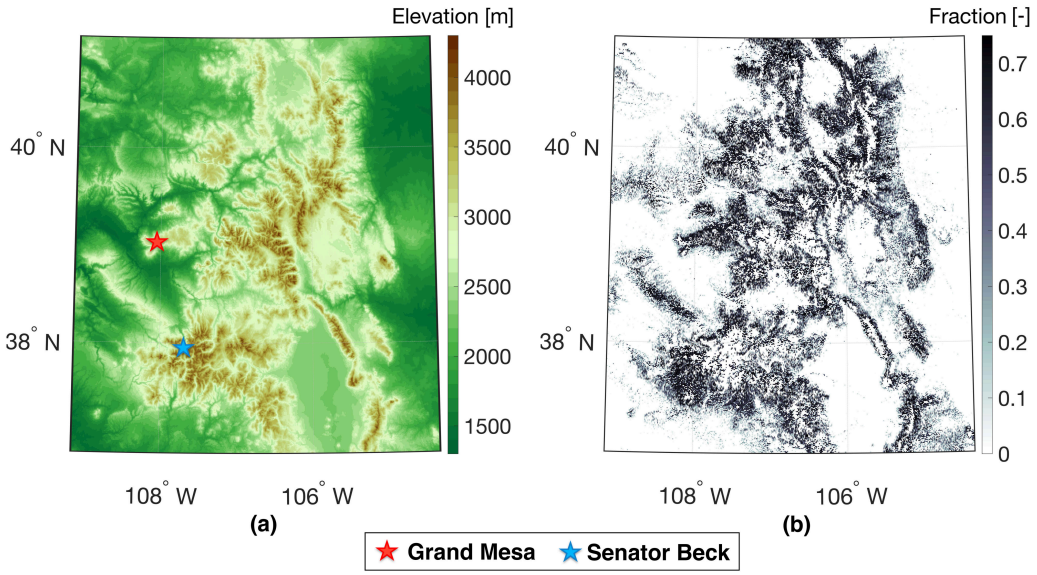

Figure 2.1: Maps of the study domain showing (a) elevation obtained from SRTM 30 m datasets and (b) forest cover fraction obtained from the global forest cover datasets from Hansen et al. [91].

to early May [30]. The primary reason for selecting Western Colorado as study domain is that it contains a variety of snow conditions across a range of topographic and land cover types. Furthermore, the selection of this domain helps leverage the NASA SnowEx campaign, which is a multi-year airborne and ground-based snow campaign with the primary objective to assess the characteristics of snow using in-situ and remotely-sensed observations [111]. Two primary evaluation sites – Grand Mesa and Senator Beck – are located within the study area. Grand Mesa, in particular, is known as one of the largest flat-topped mountains in the world. Since SAR observations generally contain geometric distortions over complex terrain, the investigation of SAR over flat terrain can help minimize the geometric distortion, which is regarded as one of the largest source of uncertainties for the backscatter observations.

2.2.2 Sentinel-1 Observations

Sentinel-1 is a constellation of two satellites (Sentinel-1A and -1B launched in April 2014 and April 2016, respectively) developed by the European Space Agency as a component of the European Copernicus Program [8]. Sentinel-1 ensures the data continuity of previous SAR systems, including ERS-2 and ENVISAT, with the main objective of continuously monitoring the land surface, ocean, and ice during all-weather, day-and-night conditions [170]. Both Sentinel-1A and Sentinel-1B carry C-band SAR sensors with a 180° difference in orbital phase [205]. Sentinel-1 has a revisit frequency of 12 days for each satellite, which results in achieving a 6-day global revisit frequency between the two different satellites. However, it has an irregular data acquisition scenario over North America until 2017 due to the evolving observation (operational) scenarios, and as a result, impacts the availability of Sentinel-1A and -1B products in these regions [131].

Table 2.1: Main characteristics of Sentinel-1 data acquisition mode.

Parameters	Stripmap	Interferometric wide (IW)	Extra wide (EW)	Wave (WV)
Polarization	Single	Dual	Dual	Dual
Swath Width	80 km	250 km	400 km	20 km × 20 km
Spatial resolution	$5m \times 5m$	$5m \times 20m$	$20m \times 40m$	$5m \times 5m$
Application	Small island	Land	Sea ice Polar zone Maritime	Ocean

Sentinel-1 provides four exclusive image acquisition modes (e.g., Strip-map, Interferometric Wide swath [IW], Extra Wide swath, and Wave [WV] mode). Table 2.1 describes the main differences and characteristics of each mode. In the case of

Table 2.2: Main characteristics of Sentinel-1 IW ground range detected (GRD) products.

Product Type	GRD-High
Center Frequency	5.407 GHz
Swath Width	250 km
Incidence Angle	18.3° – 46.8°
Resolution	20 m × 22 m
Pixel Spacing	10 m × 10 m

IW and EW modes, a relatively large swath can be obtained by virtue of terrain observation with a progressive scan SAR (TOPSAR) technique. TOPSAR allows the antenna steering in both azimuth and range directions, which enables the acquisition of more information from the target with different sub-swaths [56].

Along with the data acquisition modes, Sentinel-1 has three different processing levels: 1) Level-0 product providing the unfocused and compressed backscatter observations, 2) Level-1 data (Single Look Complex; SLC and Ground Range Detected; GRD) that utilizes baseline processing algorithms, and 3) Level-2 data (Ocean; OCN) products that apply advanced processing algorithms to the Level-1 products for wind, wave, and other applications. As the primary focus of this research is to apply C-band backscatter in analyzing terrestrial snowpack characteristics, the Sentinel-1 IW GRD datasets are used here. Table 2.2 describes the main characteristics of the Sentinel-1 IW GRD datasets.

Before applying the Sentinel-1 imagery to this analysis, it is essential to first preprocess the datasets in order to remove several sources of noise such as geometric distortion, speckle, and thermal noise [80,160]. Accordingly, standard pre-processing

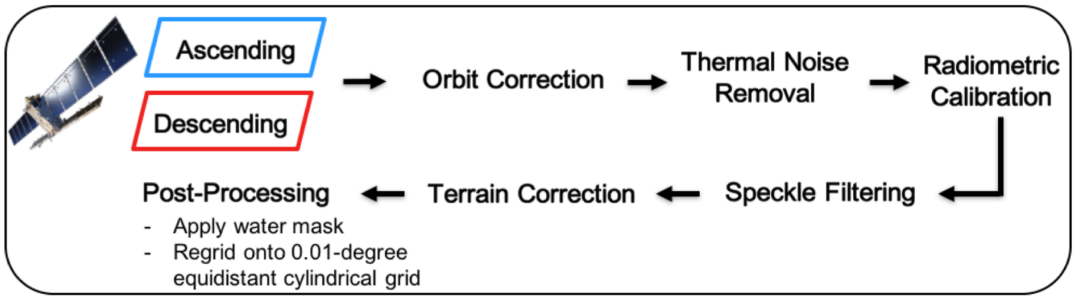

Figure 2.2: Description of Sentinel-1 preprocessing steps conducted through the google earth engine.

steps (Figure 2.2) were employed using Google Earth Engine with an additional incidence angle normalization step following the procedures as outlined in Lievens et al. [131]. The pre-processed Sentinel-1 imagery was then regridded (as an arithmetic average) onto a 0.01-degree equidistant cylindrical grid in order to match the resolution of the land surface model used in this analysis (see Section 2.2.3 for more details).

2.2.3 Land Information System

The NASA Land Information System (LIS) is a software framework developed at the NASA Goddard Space Flight Center to integrate a suite of land surface models (LSMs), satellite observations, ground-based measurements, and data assimilation in order to obtain improved posterior estimates of land surface states and fluxes [118]. The main advantage of the LIS framework is the flexibility and high-performance computing capabilities, including advanced software techniques, that enables computational tractability in integrating and assimilating observations across regional and global scales. LIS is comprised of three main components: 1)

the Land surface Data Toolkit (LDT), 2) LIS core, and 3) Land Validation Toolkit (LVT). LDT is the prepocessor for LIS, which processes the input datasets to use in the LSMs [6]. It also allows the processing of model parameters, meteorological forcing datasets, and initial conditions to meet the needs of DA-related data processing requirements. LIS core is the main infrastructure that enables the various LSMs including Noah-MP, CLM, VIC, and Community Atmosphere Biosphere Land Exchange (CABLE) with high performance computation using input datasets generated via LDT [118]. The last component in LIS system is LVT, which is designed to conduct evaluation and intercomparison of the simulated geophysical variables from LIS with large validation datasets including ground-based measurements, remotely-sensed datasets, and reanalyses [119]. It also enables the analysis of estimates from LIS subsystems including DA, optimization, and radiative transfer models.

Among the various suite of LSMs included in LIS, Noah-MP was selected for use in this study. Noah-MP is based on the Noah LSM and allows for multiple parameterizations of the different processes (e.g., energy balance within the vegetation canopy, snowpack metamorphosis, frozen soil and infiltration, and interaction between soil moisture and ground water) of land-atmospheric interactions [154]. Niu et al. [154] discussed how Noah-MP employs a three-layer, physically-based snow model that considers melting and refreezing of snow, which results in a more accurate quantification of snow mass than those from different land surface models [199, 226]. The NASA Modern-Era Retrospective analysis for Research and Application, version 2 (MERRA-2) [82] product was selected for use as the meteorological boundary conditions. The input datasets (e.g., land cover type, soil texture, and topography)

were processed using the Land Data Toolkit [6] and initial conditions were adjusted during the spin-up period, starting from January 1980 to March 2015. After the spin-up period, all subsequent experiments utilize the same initial conditions in an effort to minimize initial condition errors and uncertainty. Geophysical variables derived from LIS have a spatial and temporal resolution of 0.01° (equidistant cylindrical projection) and daily (averaged 15-minute model estimates), respectively.

2.3 Experimental Setup

2.3.1 Support Vector Machine

Machine learning (ML) is rapidly becoming an essential research tool to improve the knowledge of complex hydrologic processes [28]. ML is an algorithm that can learn a highly sophisticated, non-linear relationship between inputs and outputs for a given physical system based on statistical inference [127]. The term learning (a.k.a., training) suggests an optimization procedure that reduces the differences between the observations and the model estimates [195]. ML has advantages in improving computational efficiency by replacing the time-consuming human activity of discovering regularities in the training data by using automated techniques [123]. Examples of ML techniques include decision trees, random forests, artificial neural networks, and support vector machines.

Support vector machine (SVM) regression is one of the supervised machine learning algorithms that maps the input space into higher dimensional feature space using a kernel function [213]. SVMs have been widely utilized in hydrologic fields

with a variety of purposes such as spatial pattern recognition [128,179], classification [92,168], and temporal prediction [2,74,77,87,121,227].

He et al. [92] examined the application of a SVM classifier to map snow cover using Radarsat-2 Polarimetric SAR over the Tianshan mountains in China. Xiao et al. [223] explored snow depth retrieval with support vector machine regression using brightness temperatures (T_b) from the SSM/I and Special Sensor Microwave Imager/Sounder across Eurasia. Ahmad et al. [2], Forman and Reichle [74], and Forman and Xue [77] utilized SVMs to predict T_b over snow-covered terrain using observed T_b from different passive microwave radiometers. This study here focuses on predicting C-band backscatter over snow-covered terrain using SVM regression. The overall framework, in general, follows that of Forman and Reichle [74], although it uses different training targets and LSMs along with different physical considerations in the context of active versus passive remote sensing of snow. A detailed description of the SVM training and prediction procedure is introduced below.

2.3.2 SVM Regression

Figure 2.3 shows the general schematic of support vector machine regression used in this study. Assume a $[M \times N]$ training matrix, x, such that it contains N = 4 different geophysical variables simulated from Noah-MP for characterizing the physical conditions of snow at M different times for a given location in space. The training target (z; Sentinel-1 backscatter observations in this paper) has a size of $[M \times 1]$. Suppose the $[1 \times \mathrm{N}]$ input vector (y) is comprised of geophysical

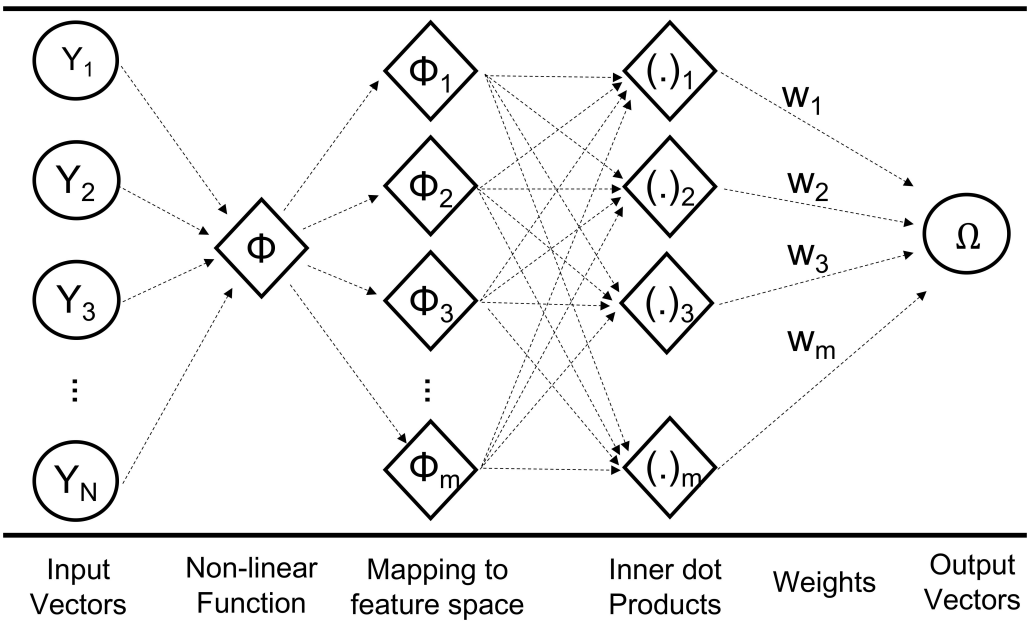

Figure 2.3: General schematic of support vector machine regression.

variables estimated from the LSM to characterize the physical properties of snow at a given time and location. When the input datasets are trained based on the co-polarized (i.e., vertical transmit and vertical receive; σ^0_{VV}) and cross-polarized (i.e., vertical transmit and horizontal receive; σ^0_{VH}) backscatter observations from Sentinel-1, predicted backscatter at co- ($\hat{\sigma}^0_{VV}$) and cross-polarization ($\hat{\sigma}^0_{VH}$) can be computed through the nonlinear SVM expressed as follows:

$$\begin{bmatrix} \hat{\sigma}^0_{VV} \\ \\ \hat{\sigma}^0_{VH} \end{bmatrix} = f(x) = \sum_{i=1}^{M} (\alpha_i - \alpha_i^*) k(x_i, y) + \delta \tag{2.1}$$

where M indicates the number of available training target sets in time at a given location in space; α_i and α_i^* represents the dual Lagrangian multipliers at time i; and δ represents the bias (a.k.a., offset) coefficients that are all defined during the training procedure. x is the training matrix with a size of [M $\times$ N] comprising model input

vectors x at the times of the M training targets [74]. $k(x_i, y) = \exp\{-\gamma||x_i - y||^2\}$ is a scalar radial basis kernel function (RBF) that helps map the geophysical inputs into the observation space. The rationale for choosing a RBF for the kernel in this study is based on previous research proved that showed a RBF yielded satisfactory performance in solving complicated, nonlinear hydrologic problems [9,60]. The solution to equation (2.1) is calculated by employing the LIBSVM library [35], which is an open source machine learning library developed by National Taiwan University. Please see Appendix B for more details on the SVM regression procedure

2.3.3 SVM Inputs, Training Targets, and Outputs

One of the most important steps to develop a well-designed ML algorithm is the selection of relevant input variables [22]. Thus, an exhaustive sensitivity analysis was first conducted with nine geophysical variables from Noah-MP (Figure 2.4) to select the most appropriate combination of input datasets for SVM regression. Here, the normalized sensitivity coefficient (NSC; Willis and Yeh [219]) was utilized to assess the sensitivity of predicted backscatter from the SVM to each state variable used from Noah-MP. NSC can be calculated as follows:

$$NSC_{i,j} = \frac{\partial M_j}{\partial P_i} \times \frac{P_i^o}{M_j^o} \approx \frac{M_j^i - M_j^o}{\Delta P_i} \times \frac{P_i^o}{M_j^o} \tag{2.2}$$

where M_j^o and P_j^o is the initial metric and state value, respectively. M_j^i indicate the perturbed metric value and ∂P_i is the amount of perturbation. Note that i and j indicate the index for state and output metric, respectively. In this study, each LIS input state was perturbed $\pm 2.5\,\%$ one at a time. Here, we assume the independence

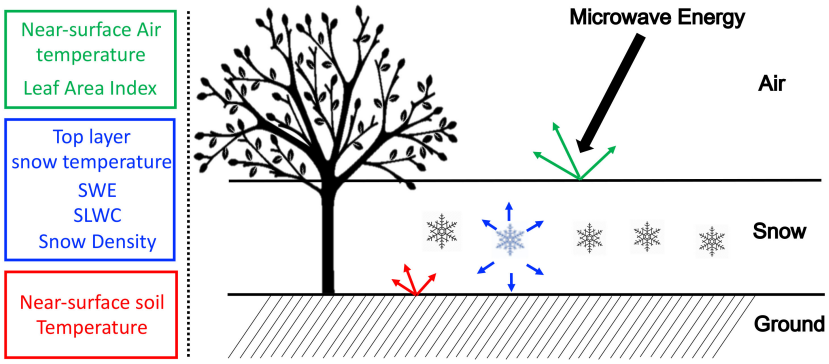

Figure 2.4: List of input datasets for SVM regression with corresponding scattering algorithm.

between any two states even if the NSC is still dependent throughout all states. Comparison of NSCs from different states can provide valuable information as to verify the theoretical scattering mechanisms in the snow-covered terrain as well as choose reasonable input datasets for predicting backscatter with SVM.

Table 2.3: Geophysical states used as input for SVM training and prediction.

Model State	**Unit**	**Unit conversion factor**
Snow Water Equivalent	m	10
Snow Density	kg/m^3	0.01
Snow Liquid Water Content	mm	1
Top-layer snow temperature	K	0.01
Near surface temperature	K	0.01
Leaf Area Index	[-]	1
Bottom-layer snow temperature	K	0.01
Top-layer soil temperature	K	0.01
Top-layer soil moisture	m^3/m^3	10

Figure 2.5 exhibits the NSCs of each state vector for dry snow (e.g., December, January, and February) and wet snow (e.g., March, April, and May) period. The results revealed that both snow density and SWE showed the highest NSCs during both seasons. In the case of SLWC, it showed the third highest sensitivity (co-pol:

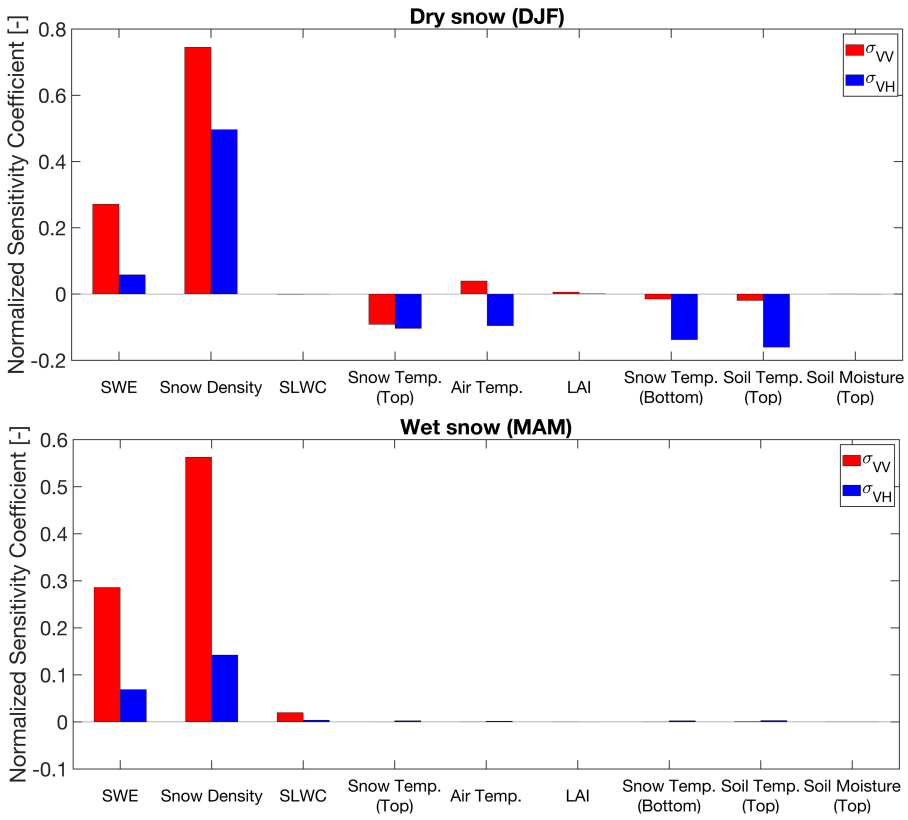

Figure 2.5: Summary of domain-averaged Normalized Sensitivity Coefficients of predicted backscatter during (a) dry and (b) wet snow seasons for both co- and cross-polarized observations.

0.02 and cross-pol: 0.004) during the spring season (Figure 2.5(b)) while the dry snow season showed sensitivity near zero at both polarizations (Figure 2.5(a)). This result is reasonable given wet snow has more liquid water inside the snowpack than dry snow due to the snow melting. In addition to NSCs, statistical metrics (e.g., bias, relative bias, RMSE, unbiased RMSE, and standard error ratio) were computed with respect to different input states from Noah-MP. The selection of input states followed the order represented in Table 2.3. For example, the number of datasets as five represents that it used 1) SWE, 2) snow density, 3) SLWC, 4) top layer snow temperature, and 5) leaf area index as inputs for training. Dimensioned statistics (e.g., bias, RMSE, and ubRMSE) as well as relative bias showed that utilizing four input states (e.g., SWE, snow density, SLWC, and top layer snow temperature) produced the most reasonable accuracy of predicted backscatter (Table 2.4). Moreover, all statistics (including both dimensioned and dimensionless) approached asymptotic values after four input states. These results provided rationale that using a selection of four input states (listed in Table 2.5) for SVM regression was the most appropriate.

As the four variables have different ranges of magnitude, each variable was first rescaled using a scale factor in order to remove the different orders of magnitude, which will significantly influence the weights and SVM prediction capability. In addition to the LSM state variables, the Interactive Multisensor Snow and Ice Mapping (IMS) [152] binary snow cover product was used to further constrain the SVM training only when snow cover is positively detected using the visible and thermal-based snow cover estimation algorithm.

Table 2.4: Statistical summary of evaluation metrics as a function of the input states.

(a) σ_{VV}	1	2	3	4	5	6	7	8	9
Bias	-0.53	-0.48	-0.49	-0.16	-0.32	-0.32	-0.32	-0.32	-0.32
Relative Bias	4.79	4.39	4.46	1.43	2.92	2.89	2.89	2.89	2.89
RMSE	1.46	1.45	1.43	1.38	1.34	1.34	1.34	1.34	1.34
ubRMSE	1.17	1.17	1.16	1.03	1.14	1.14	1.14	1.14	1.14
Standard Error Ratio	1.21	1.20	1.18	1.14	1.11	1.11	1.11	1.11	1.11
(b) σ_{VH}	1	2	3	4	5	6	7	8	9
Bias	-0.55	-0.52	-0.53	-0.47	-0.4	-0.4	-0.4	-0.4	-0.4
Relative Bias	3.01	2.83	2.92	3.10	2.56	2.55	2.55	2.55	2.55
RMSE	1.40	1.38	1.37	1.12	1.15	1.15	1.15	1.15	1.15
ubRMSE	1.12	1.12	1.10	0.73	0.94	0.94	0.94	0.94	0.94
Standard Error Ratio	1.11	1.10	1.09	0.89	0.92	0.92	0.92	0.92	0.92

Note:Units for bias, RMSE, and ubRMSE are dB. Relative bias has units of % and standard error ratio is dimensionless.

Training targets (and outputs) for the SVM were selected as σ^0_{VV} and σ^0_{VH} as observed by Sentinel-1 over snow-covered terrain. Backscatter coefficients observed at different polarizations contain different information about terrestrial snow. Generally, σ^0_{VV} for dry snow tends to have limited sensitivity to snow as the backscatter

Table 2.5: SVM Inputs and Outputs.

Inputs	**Unit**	**Scale Factor**
Snow Water Equivalent	m	10
Snow Density[a]	$\mathrm{kg\,m^{-3}}$	0.01
Snow Liquid Water Content[a]	mm	1
Top layer Snow Temperature	K	0.01
Outputs	**Unit**	**Scale Factor**
$\hat{\sigma}^0_{VV}$	dB	none
$\hat{\sigma}^0_{VH}$	dB	none

[a] Column-integrated estimates.

from the snow-land interface often dominates over snow volume scattering [10]. Nevertheless, the sensitivity of σ^0_{VV} during wet snow conditions is relatively high due to the significant absorption and reflection from the snowpack [131, 150]. In terms of σ^0_{VH}, it generally shows more sensitivity than σ^0_{VV} during both dry and wet snow conditions due to the depolarization of the microwave signal caused by multiple scatterings within the snowpack [228]. Based on these different characteristics, backscatter at different polarizations were trained separately.

2.3.4 Training Procedures

A SVM was trained at each 0.01° equidistant cylindrical model grid location in order to explicitly consider the heterogeneity of regional climatology, land cover type, and topography. At each pixel, a separate SVM was generated for producing predicted co-polarized ($\hat{\sigma}^0_{VV}$) and cross-polarized ($\hat{\sigma}^0_{VH}$) backscatter separately. Available Sentinel-1 observations from April 2015 to August 2016 and September 2017 to August 2018 were utilized for training, which includes two complete winter seasons. Sentinel-1 observations from September 2016 to August 2017 were excluded in order to be used to evaluate the SVM prediction, which is described further in Section 2.3.5.

There are numerous considerations when developing a physically–constrained, well–designed SVM, including parameter setups, input datasets, training targets, and training windows. Accordingly, the first experiment was conducted to analyze the influence of different training targets on SVM prediction performance. Sentinel-

1 observes backscatter along ascending and descending overpasses. One of the main differences between the ascending and descending overpass is the local overpass time. Ascending measures backscatter at approximately 6 p.m. local time while descending measures backscatter at approximately 6 a.m. local time. Moreover, the ascending and descending tracks have different incidence and azimuth angles in complex terrain, which leads to a different backscatter intensity [182]. Normalizing the incidence angle for both ascending and descending overpasses during the pre-processing step (previously described in Section 2.2.2) reduces the influence of the local incidence angle. Hence, more available training targets (which, in general, is advantageous given a sparse training set) can be obtained by combining both the ascending and descending overpasses. However, it remains to be seen if combining different overpasses is advantageous or disadvantageous. Consequently, Sentinel-1 backscatter from the ascending node versus the descending node versus the combined overpasses were trained separately in order to explore the different impacts on SVM performance.

The second experiment is designed to examine the influence of different training windows on the prediction accuracy of the SVM across which to collect the Sentinel-1 training targets. Figure 2.6 shows the concept of three different training windows: 1) fortnightly, 2) monthly, and 3) seasonal. The fortnightly training procedure includes 2-weeks of overlap before and after the specific fortnight (14-day period) in order to reduce temporal discontinuities between different SVMs [75]. Analogously, the monthly training period includes the month before and month after the specific month of training during the collection of the training targets. In the

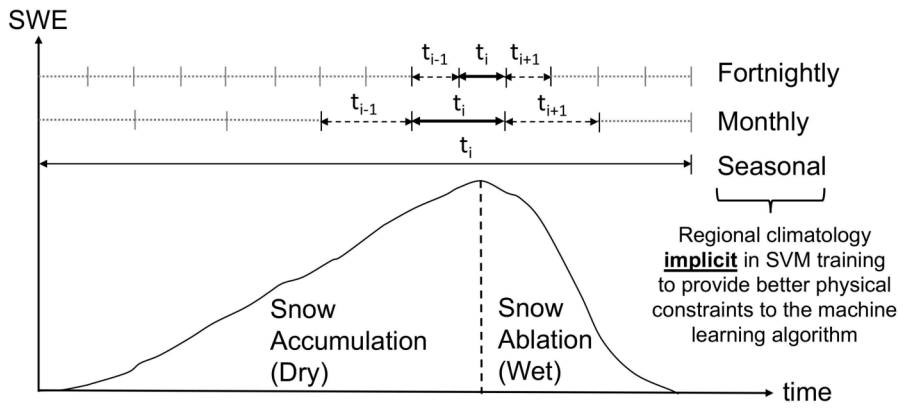

Figure 2.6: Schematic description of fortnightly versus monthly versus seasonal training approaches. Different training windows provide different degrees of wet versus dry snow delineation. Bold arrows indicate the training period and dashed arrows represent the temporal overlap. The gray dotted lines represent periods of time *not* included in the training data for the period t_i. The shorter window provides better discrimination, but the trade-off is a less robust SVM due to fewer training targets as a function of time.

case of a seasonal training window, it includes the Sentinel-1 observations during the entire snow season (e.g., from September to May). The underlying rationale of the fortnightly training window is to generate a physically-constrained SVM that more carefully considers the first-order control on the different electromagnetic responses from dry snow versus wet snow. Dry snow is regarded as a scatterer of MW radiation while wet snow is regarded as an absorber given that the presence of liquid water within the snowpack results in a large increase in permittivity [186]. Thus, a shorter training window can enhance the delineation between dry versus wet snow. On the other hand, elongating the length of the training window ensures more available training data for the SVM even though there is more possibility to comingle the observations containing a different electromagnetic regime.

Lastly, explicit SVM training for dry snow versus wet snow conditions was conducted separately in order to explicitly analyze the influence of snow wetness on

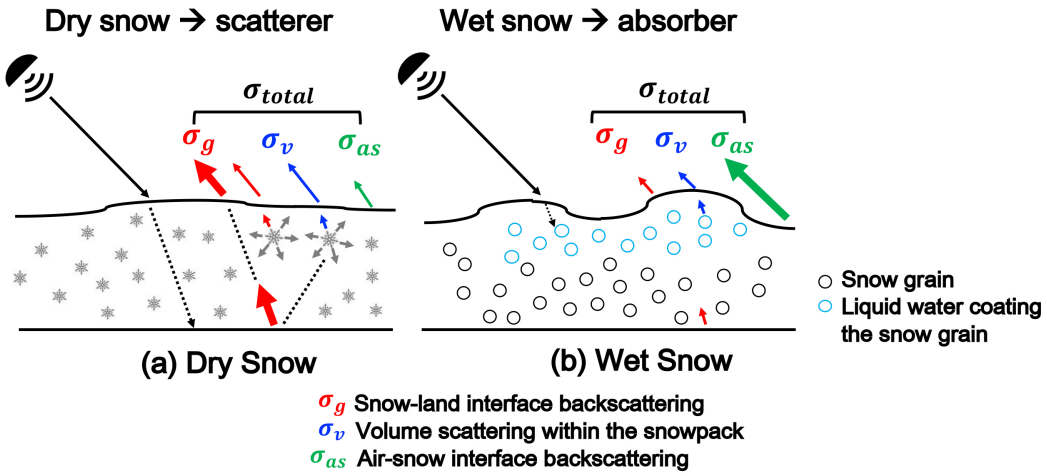

Figure 2.7: Conceptual model of active MW backscattering mechanisms during (a) dry snow conditions and (b) wet snow conditions (modified from [67]).

SVM prediction efficacy. Figure 2.7 illustrates the different scattering mechanisms over dry and wet snow conditions. During dry snow conditions, a snowpack is a mixture of air and ice. Microwave radiation can penetrate deeper into a dry snowpack (i.e., less absorption) than during wet snow conditions. Accordingly, backscatter from the underlying ground is more influential on the total observed backscatter relative to other scattering components (Figure 2.7(a)). When the snow depth or snow surface roughness increases, the influence of backscatter from within the snowpack as well as at the air-snow interface increases. Correspondingly, the influence of backscatter from the underlying ground is reduced [220]. In the case of wet snow, which is now a heterogeneous mixture of air, ice, and water, the photons cannot penetrate as deeply into the snow due to the decrease in scattering albedo and the corresponding increase in the absorption of microwave radiation associated with the existence of liquid water inside the snowpack [187, 220]. Accordingly, backscatter over wet snow is primarily dominated by backscatter at the air-snow interface in

most situations (Figure 2.7(b)). However, during the ripening stage, backscatter over wet snow can also be increased due to the complex wet snow metamorphism, including an increase in snow surface roughness and an increase in the snow grain size during overnight refreezing [139]. Considering the different electromagnetic responses of C-band radiation during for dry snow versus wet snow conditions (based on the snow wetness in the *a priori* LSM estimates) provides one more mechanism to explore different physically-constrained training techniques to the machine learning procedure.

2.3.5 Evaluation Scheme

Predicted backscatter for both polarizations were evaluated by comparing against Sentinel-1 backscatter observations *not* used during training (i.e., from Sep 2016 to Aug 2017). This ensures that the validation dataset is entirely independent from the Sentinel-1 datasets used for training. One of the main reasons to select Sep 2016 to Aug 2017 for validation is that this period was considered as a typical snow year for the available years in Sentinel-1 records.

In order to quantitatively evaluate the predicted backscatter from the SVM, domain-averaged bias, root mean square error (RMSE), and unbiased RMSE (ubRMSE) were computed by averaging the metrics across the snow-covered grid cells in this study domain. Bias is calculated as follows:

$$\text{bias} = \frac{1}{n}\sum_{i=1}^{n}(\hat{\sigma}^0_{pol} - \sigma^0_{pol}) \tag{2.3}$$

where n is the number of predicted and observed backscatter values collocated at a

given location in space and time and $\hat{\sigma}^0_{pol}$ [dB] and σ^0_{pol} [dB] represents the predicted and observed backscatter at a given polarization, respectively. Bias is one of the goodness-of-fit statics that explains the systematic error. RMSE is a dimensionless statistic representing both systematic and non-systematic errors that can be calculated as:

$$\text{RMSE} = \sqrt{\frac{1}{n}\sum_{i=1}^{n}(\hat{\sigma}^0_{pol} - \sigma^0_{pol})^2} \tag{2.4}$$

In addition, ubRMSE is utilized to identify the random error by removing the bias from RMSE as:

$$\text{ubRMSE}^2 = \text{RMSE}^2 - \text{bias}^2 \tag{2.5}$$

These statistics were calculated over the course of the entire validation period. In addition, statistics during the snow accumulation and snow ablation periods were calculated separately as the delineation of dry snow versus wet snow motivates three different experiments outlined in Section 2.3.4. Seasonal snow, in general, can be divided into a snow accumulation period and a snow ablation period. The snow accumulation period typically has relatively dry snow conditions while the snow ablation period has relatively wetter snow conditions. When considering the regional climatology of Western Colorado, December, January, and February (DJF) are treated here as the snow accumulation period and March, April, and May (MAM) are treated here as the snow ablation period [185].

As part of the statistical evaluation, the presence of statistically significant differences between the various domain-averaged statistics was conducted using the two-sided Wilcoxon signed rank sum test [218]. Wilcoxon signed rank test is a non-

parametric hypothesis test to examine the null hypothesis that central tendencies of two samples are not different [142]. The main reason for selecting the Wilcoxon signed rank test is that the predicted and observed backscatter is non-Gaussian, which violates the assumption for the two-sample t-test.

2.4 Results and Discussions

2.4.1 Influence of Training Targets on SVM Prediction

The influence of different training target sets on the robustness of SVM prediction over snow-covered terrain was explored by using three different training target sets: 1) Sentinel-1 observations from ascending (6 p.m. local time) overpasses only, 2) descending (6 a.m. local time) overpasses only, and 3) the combination of the two different overpasses. In this section, the same geophysical inputs acquired from LIS (listed in Table 2.5) were utilized for SVM regression and a fortnightly training window was selected for each of the three different scenarios. With these experimental setups, predicted backscatter from the different sets of training targets were evaluated by comparing against Sentinel-1 observations during Sep. 2016 to Aug. 2017, which were not used for SVM training. Table 2.6 summarizes the spatial coverage as well as the domain-averaged statistics of predicted $\hat{\sigma}^0_{VV}$ and $\hat{\sigma}^0_{VH}$ using the three different training sets for the validation period.

Among the three different training target sets, predicted backscatter using the descending-only overpasses showed the lowest magnitude of domain-averaged bias at both co- and cross-polarizations. The computed bias for the descending-only

Table 2.6: Domain-averaged statistics of predicted backscatter from ascending-only, descending-only, and the combination of both ascending and descending overpasses compared against the Sentinel-1 observations from Sep 2016 to Aug 2017 *not* used during training.

	Bias		**RMSE**		**ubRMSE**		**Spatial Coverage**
Datasets	$\hat{\sigma}^0_{VV}$	$\hat{\sigma}^0_{VH}$	$\hat{\sigma}^0_{VV}$	$\hat{\sigma}^0_{VH}$	$\hat{\sigma}^0_{VV}$	$\hat{\sigma}^0_{VH}$	[%]
Ascending-only	-0.89	-0.84	1.64	1.36	0.91	0.73	7.2
Descending-only	-0.74	-0.82	1.58	1.36	1.16	0.80	11.9
Combination	-0.83	-0.95	2.54	2.06	2.08	1.54	15.2

Note: All statistics are different at $p = 0.05$ *using Wilcoxon signed rank sum test.*

training targets were within the range from -5.37 to 4.86 dB with a spatial mean of -0.74 dB for $\hat{\sigma}^0_{VV}$. Similarly, the bias of $\hat{\sigma}^0_{VH}$ with descending-only training targets ranged from -4.92 to 3.85 dB with the spatial mean of -0.82 dB. In the case of ascending-only and combined training target sets, it revealed a relatively wider range of biases than descending-only training sets at both polarizations. For example, predicted backscatter of $\hat{\sigma}^0_{VV}$ with ascending-only training sets and combined training sets showed the bias ranging from -12.3 dB to 11.7 dB and -10.2 dB to 14.5 dB, respectively. This difference in the range of bias resulted in exhibiting the lowest mean RMSE at both polarizations over the study area when descending-only training targets were used (Table 2.6). Among the three different training target sets, the combined training target set showed the highest RMSE and ubRMSE at both polarizations. This result is also confirmed in the first row of Figure 2.8 in that combined training targets showed wider spread than other training target sets.

Different statistical behavior for ascending and descending overpasses is a consequence of the different electromagnetic responses from the snowpack in accordance

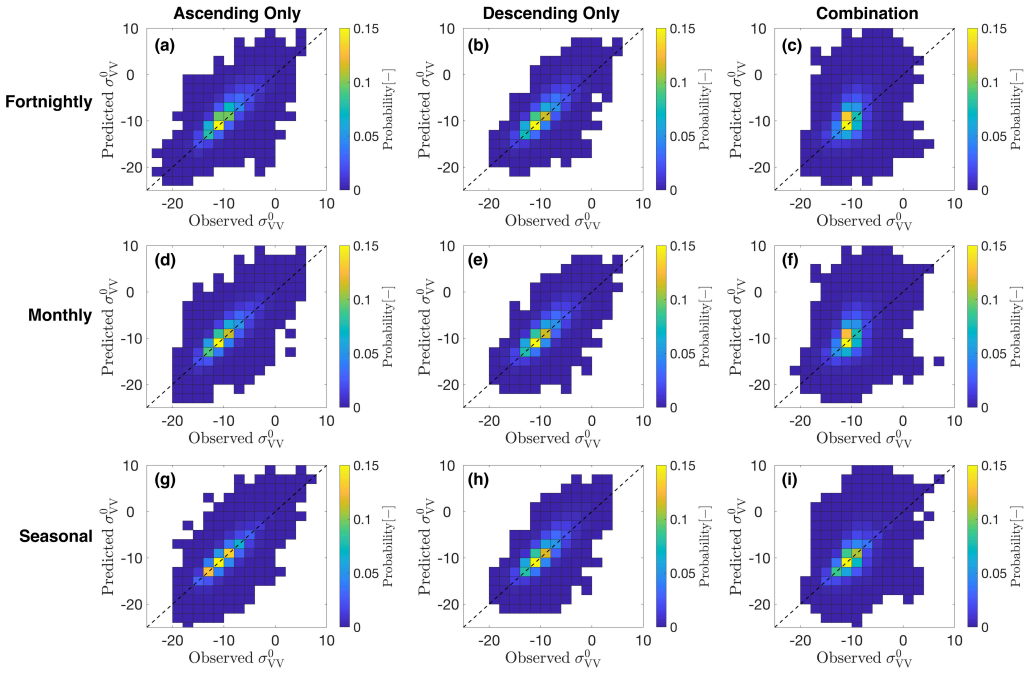

Figure 2.8: Probability plots of observed and predicted co-polarized backscatter during the validation period collected in both time and space. The different columns represent the different training targets: ascending-only (left column), descending-only (middle-column), and combination of ascending and descending (right column). The different rows represent the different training windows (fortnightly, monthly, and seasonal training period from the top to bottom). The dashed line represents the 1:1 line.

with the data acquisition times. As discussed earlier in Section 2.3.3, the local time of ascending and descending overpass is approximately 6 p.m. and 6 a.m., respectively. Differences in observation time often results in having different snow conditions based on the diurnal melt-refreeze metamorphism. Diurnal variation of the air temperature results in small amounts of diurnal melting and refreezing at the snow surface. Accordingly, the descending acquisitions prior to sunrise (∼6 a.m. local time) tends to minimize wet snow conditions and are relatively dry given refreezing while ascending acquisitions following sunset (∼6 p.m. local time) are often relatively wet at the surface by comparison. In the case of combined training targets, the mixture of signals from ascending and descending overpasses within a single training matrix resulted in producing more uncertainties, which is revealed as relatively larger RMSE and ubRMSE than the other training target sets.

Figure 2.9 illustrates the spatial distribution of bias, RMSE, and ubRMSE using three different training target sets over the study domain. Notably, the combined training set showed the highest percentage of spatial coverage as more training datasets are available through combining observations from ascending as well as descending overpasses. At the same time, however, higher magnitudes of bias, RMSE, and ubRMSE were seen in the predicted backscatter when using the combined training target set. More specifically, comparison of Figure 2.9 with the elevation map presented in Figure 2.1(a) suggests that a relatively large magnitude of negative bias was observed within the elevation range of 2500 m to 3500 m. Throughout the different training target sets, all three sets commonly showed that more than 69% (77.5% for ascending-only, 71.9% for descending-only, and 69.5% for combined) of

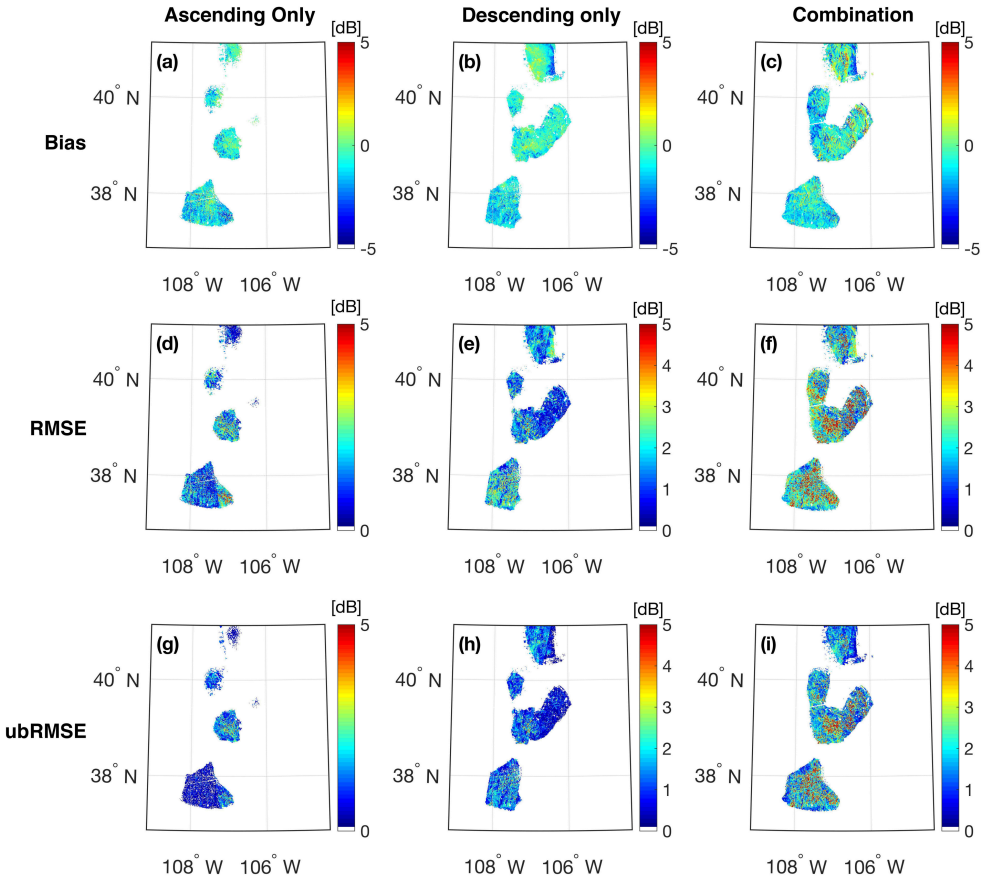

Figure 2.9: Spatial distribution of bias (top row), RMSE (middle row), and ubRMSE (bottom row) of co-polarized backscatter ($\hat{\sigma}^0_{VV}$) for the validation period Sep. 2016 to Aug. 2017. The different columns represent the training target sets for ascending only (left column), descending only (middle column), and combination of ascending and descending (right column). The white space in each map represents where there are no available SVM predictions at locations due to either no existence of snow in the LSM or insufficient Sentinel-1 observations for use during training.

pixels with a larger magnitude of negative bias (relative to the lower decile of bias) were located within the specific elevation range. This phenomenon is likely caused by the influence of vegetation on C-band backscatter. Comparison of the elevation map (Figure 2.1(a)) with the forest cover fraction illustrated in Figure 2.1(b) showed that most of the pixels with high forest cover fraction are located within the elevation range of 2500 m to 3500 m. Huang and Andereeg [98] stated that this specific elevation band contained heterogeneous forest with aspen tress and mountain snowberry as under-story species. Westman and Paris [216] and Dedieu et al. [58] mentioned that backscatter observed over the heterogeneous forest is highly influenced by vegetation-related scattering components such as multiple scatterings within the canopy and scattering from the forest floor, which results in reducing the sensitivity of C-band backscatter toward the snow.

In terms of the percent spatial coverage among the different training target sets, the combination of ascending and descending observations showed the highest spatial coverage followed by descending-only and ascending-only observations (Table 2.6 and Figure 2.9). The explanation for this behavior is that the the combination of two different sets of overpasses increases the number of available training targets, which results in more predicted backscatter at more locations across the study area.

Figure 2.10 summarizes the domain-averaged statistics of predicted $\hat{\sigma}^0_{VV}$ and $\hat{\sigma}^0_{VH}$ during the snow accumulation and ablation periods. Comparing the two different periods, the accuracy of predicted backscatter during the snow ablation (wet) period showed more negative bias than the snow accumulation (dry) period. The magnitude of bias during the snow accumulation period ranged from -0.93 to -0.64

dB and was less negative than for the snow ablation period that ranged from -1.15 to -0.72 dB. In terms of different training target sets, the descending-only set showed slightly smaller absolute bias, RMSE, and ubRMSE at both polarizations than did the ascending-only set or the combined set during both the snow accumulation period and snow ablation periods (Figure 2.10). Statistics from the descending-only training set showed a modest range of bias from -0.84 to -0.64 dB. Similarly, RMSE and ubRMSE also yielded moderate results relative to the other training target sets and ranged from -0.84 to -0.64 dB and 1.28 to 1.68 dB for RMSE and ubRMSE, respectively. In the case of the combined training set, ubRMSE was relatively large during both the snow accumulation (1.84 dB for $\hat{\sigma}^0_{VV}$ and 1.31 dB for $\hat{\sigma}^0_{VH}$) and the snow ablation (2.10 dB for $\hat{\sigma}^0_{VV}$ and 1.56 dB for $\hat{\sigma}^0_{VH}$) periods (Figure 2.10).

Distinctive statistical behaviors during snow accumulation and ablation periods are largely governed by the different physical characteristics of the snow depending during the different observation times. That is, snowpack during the snow ablation period is apt to have deeper and wetter snow than during the snow accumulation period, which introduces more heterogeneity within the snowpack given the presence of internal ice crusts, depth hoar, and wind slabs. Moreover, during the snow ablation period starting from March, in general, tends to have wetter snow surface as the top layer of snowpack experiences some degree of melt during the afternoon given more incoming solar radiation reaching the snow surface coupled with relatively warmer air temperatures. As mentioned in Section 2.3.3, the ascending and descending overpass times are 6 p.m. and 6 a.m. local time, respectively. As a result, the top of the snow surface will be relatively wetter during the ascending over-

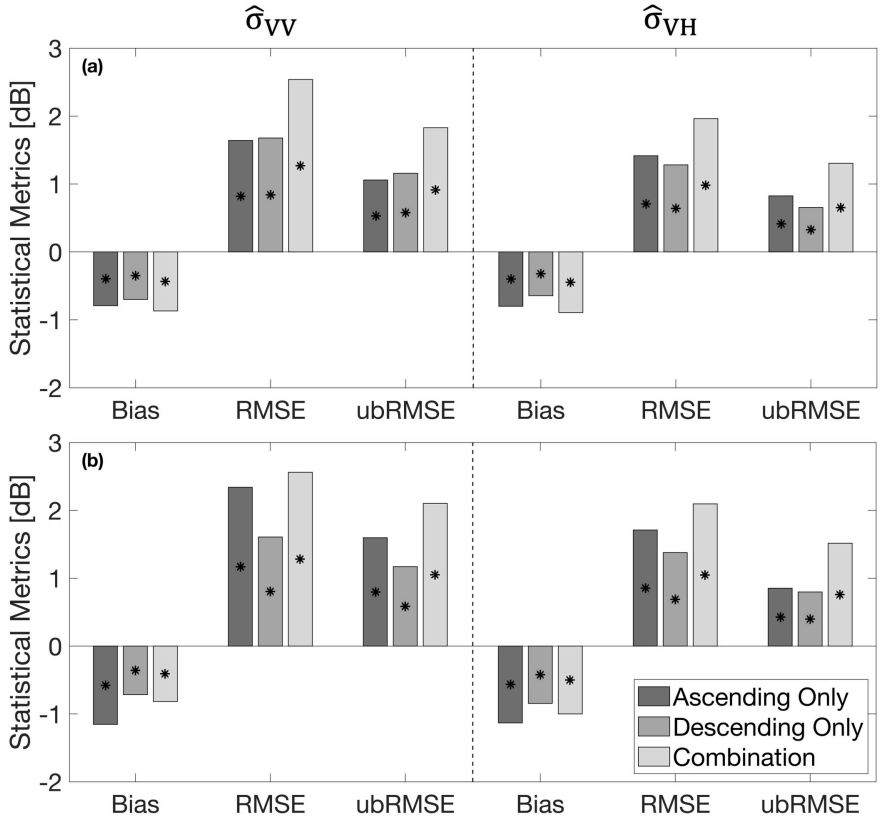

Figure 2.10: Domain-averaged statistics of predicted backscatter for three different training target sets during the (a) snow accumulation (December, January, and February) period and (b) snow ablation (March, April, and May) period. Asterisks indicate statistically significant differences between all pairs using the Wilcoxon signed rank sum test ($p < 0.05$).

pass (6 p.m. local time) while colder air temperatures during the nighttime cause the refreezing of any wet snow at the surface prior to sunrise, which corresponds to the descending overpass time (6 a.m. local time). These different conditions at the snow surface lead to the different electromagnetic responses as described in Section 2.3.4, and in turn, result in different statistical behavior for the ascending and descending overpasses. Furthermore, merging observations acquired from both ascending and descending overpasses tends to introduce more random errors related to different electromagnetic responses given the difference in snow conditions (e.g., daytime versus nighttime observations) as well as differences in viewing geometry.

2.4.2 Influence of Training Window Length on SVM Prediction

The spatial distribution of bias calculated by comparing the predicted backscatter, $\hat{\sigma}^0_{VV}$, against the corresponding Sentinel-1 observations *not* used during the training for different training windows and training sets across the validation period is depicted in Figure 2.11. Overall results showed that the magnitude of bias was reduced in accordance with an increase in the training window. For example, elongating the training window from fortnightly to seasonal resulted in reducing the magnitude of bias in the south-western and middle portions of the study area (Figure 2.11). Domain-averaged bias for ascending-only training sets also revealed significant improvement in bias comparing fortnightly training (-0.89 dB) and seasonal training (0.04 dB). Similar statistical behavior was observed for both descending-only and combined training sets in both co- and cross-polarizations. However, compar-

ing Figure 2.11(a) with 2.11(g) and Figure 2.11(c) with 2.11(i), the southern and northwestern regions of the study domain using seasonal training period showed a relatively larger, positive bias (approximately 4–5 dB) than in other parts of study area.

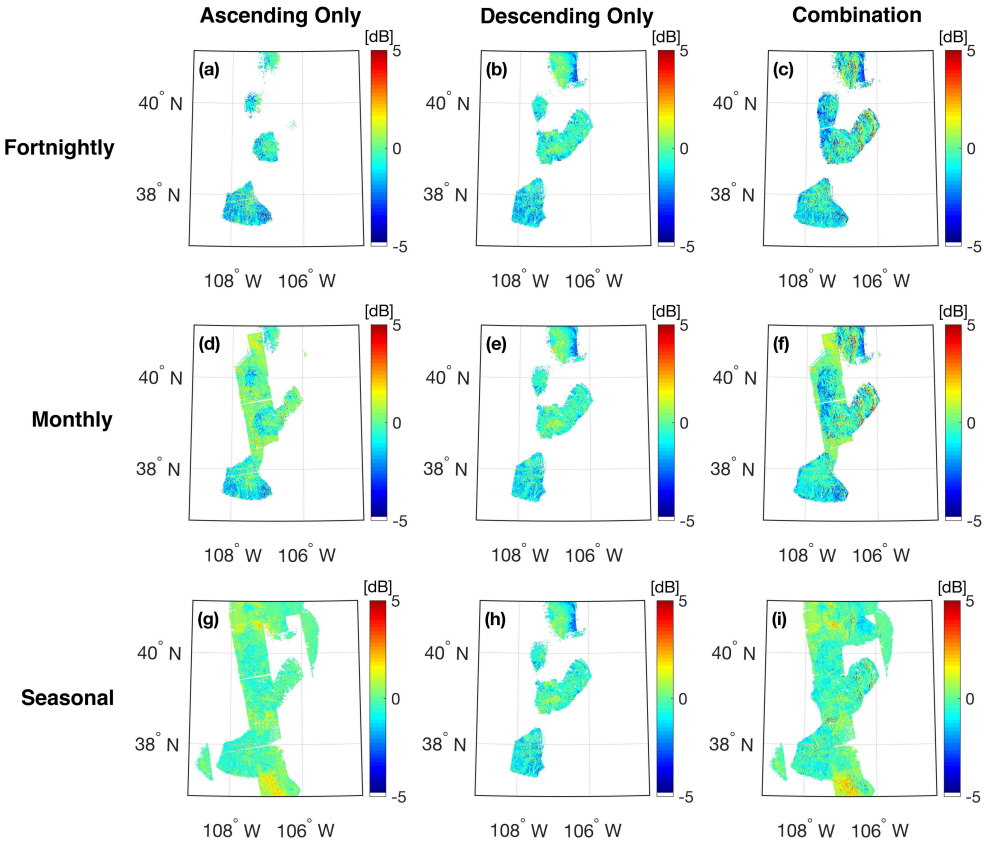

Figure 2.11: Spatial distribution of bias for co-polarized backscatter ($\hat{\sigma}^0_{VV}$) during the validation period from Sep. 2016 to Aug. 2017. The different columns represent the different training target sets: ascending-only (left column), descending-only (middle column), and combination of ascending and descending (right column). The different rows represent the different training windows (fortnightly, monthly, and seasonal from the top to bottom).

In terms of spatial coverage, the elongation of the training window resulted in the increase of spatial coverage (Figure 2.11). In general, the increased generation of SVMs makes it possible to make more predictions across the study domain when

there are more available training datasets as a function of time and space. More specifically, ascending-only and combined training sets showed a significant increase in SVM spatial coverage in comparison with descending-only training set. For instance, spatial coverage for the combined training sets was revealed as 15.3%, 20.3%, and 33.9% for fortnightly, monthly, and seasonal training periods, respectively. Similarly, spatial coverage of combined training sets (30.1%) was significantly expanded comparing with the fortnightly training period (7.18%) for ascending-only training sets. This provides clear evidence that elongation of the training window leads to an increase in availability of training data, and in turn, results in generating more SVMs at more locations as well as providing more predicted backscatter at more locations. In the case of descending-only training sets, the seasonal training period showed a slight increase in spatial coverage from fortnightly training while there was no difference in spatial coverage between monthly and seasonal training period. The fortnightly, monthly, and seasonal training period yielded a spatial coverage of 11.9%, 12.2%, and 12.2%, respectively. This behavior was highly influenced by the limited number of descending observations over the study area during the study period. Potin et al. [169] mentioned that the initial stage of Sentinel-1 operations primarily focused on the European continent based on the pre-defined observation scenario. Accordingly, Sentinel-1 observations obtained from descending nodes have significant gaps prior to May 2017 within the Western Colorado study area based on the evolving Sentinel-1 (operational) observation scenario designed by ESA. More specifically, dual-polarized (i.e., $\hat{\sigma}^0_{VV}$ and $\hat{\sigma}^0_{VH}$) Sentinel-1 observation with IW mode were mostly observed by ascending overpasses prior to May 2017. Thus, the oper-

ational limitation of dual-polarized observations during IW mode over descending overpasses limits the available training period to the 2017-18 winter season for generating SVMs over study domain. This operational issue prior to May 2017 is the cause of the limited increase in the amount of spatial coverage for the descending-only training activities.

Overall, including more training data via increasing the length of the training window enables the existence of more SVMs, and in turn, resulted in more predicted backscatter across the study domain. At the same time, however, increasing the training matrix also resulted in introducing more uncertainties due to a more diverse electromagnetic response during a larger variety of snowpack conditions. For instance, a seasonal training window utilizes Sentinel-1 observations from the spring (i.e., March, April, and May) and fall (i.e., September, October, and November) in order to predict the backscatter during the winter season (i.e., December, January, and February). However, it is known that fall and spring have distinctively different snowpack characteristics. The snowpack is relatively shallow and dry during the fall season while the spring season has relatively deeper and wetter snow, which leads to more complex snow stratigraphy with internal ice crusts. Accordingly, elongation of the training window resulted in including the mixture of electromagnetic response from dry, shallow snow mixed with deeper, wetter snow in a single training matrix that tends to weaken the robustness of the SVM predictions, and hence, results in worsening the accuracy of predicted backscatter.

Figure 2.12 and Figure 2.13 summarized the domain-averaged statistics (e.g., bias, RMSE, and ubRMSE) of predicted backscatter at both co- and cross-polarization

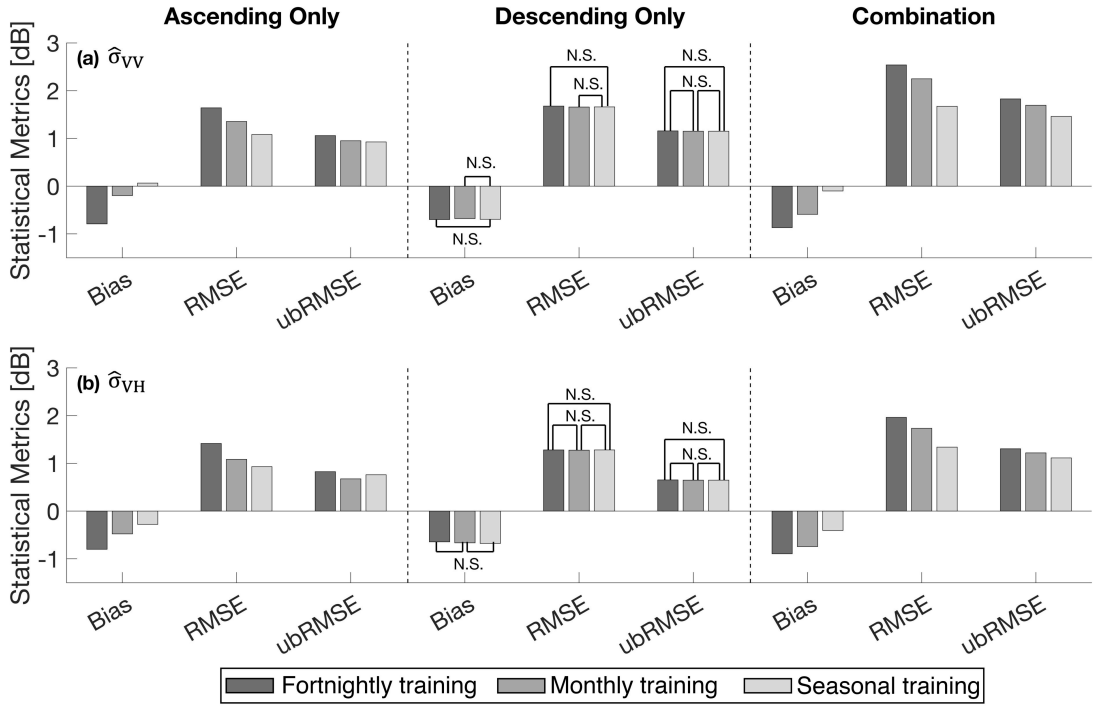

Figure 2.12: Summary of domain-averaged statistics (e.g., bias, RMSE, and ubRMSE) of predicted backscatter for fortnightly, monthly, and seasonal training windows during the snow accumulation (December, January, and February) period. N.S. represents no statistically-significant difference between pairs at p=0.05 using the Wilcoxon signed rank sum test. Other datasets achieved statistically-significant differences at p=0.05 if not marked. Left-most column used ascending-only training targets; middle column used descending-only training targets; right-most column used a combination of the two. The different bar colors represent different training window lengths. Top and bottom rows represent the co-polarized ($\hat{\sigma}^0_{VV}$) and cross-polarized ($\hat{\sigma}^0_{VH}$) backscatter.

using the three different training target sets and three training periods during the snow accumulation and ablation periods, respectively. According to Figure 2.12, the magnitude of bias, RMSE, and ubRMSE was reduced, in general, as the training period elongated from fortnightly to seasonal. For the predicted co-polarized backscatter, $\hat{\sigma}^0_{VV}$, at ascending overpasses, the magnitude of bias decreased from -0.79 dB (fortnightly training) to 0.07 dB (seasonal training). Similar behavior was observed for RMSE (1.64 dB for fortnightly training and 1.08 dB for seasonal train-

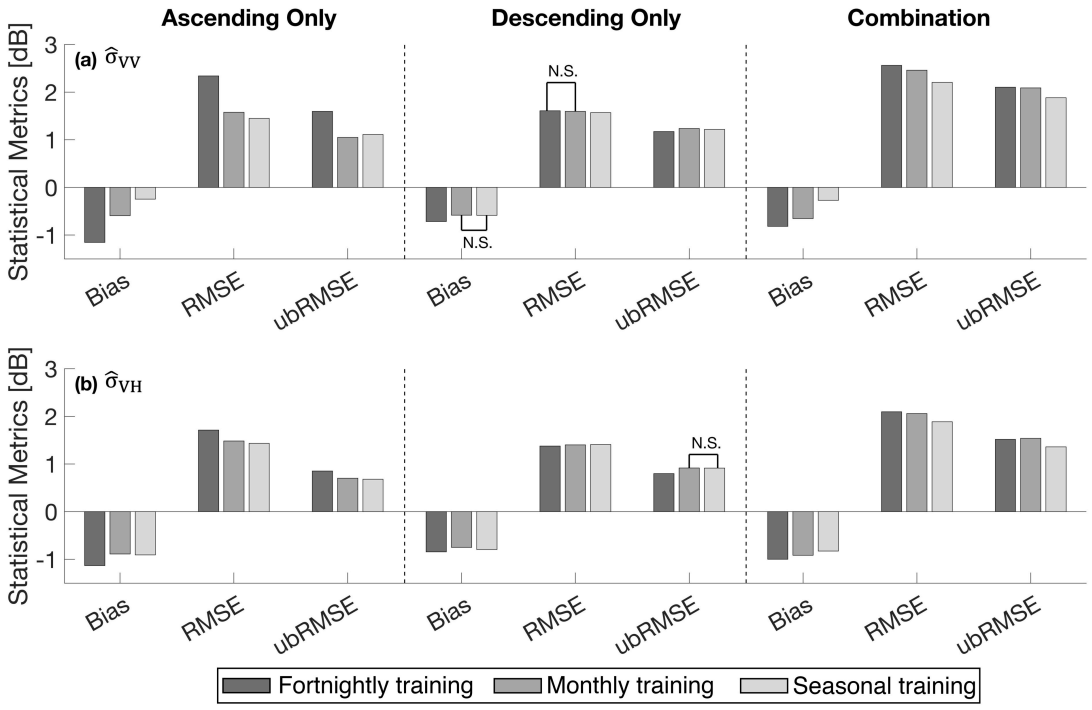

Figure 2.13: Same as Figure 2.12 except for the snow ablation (March, April, and May) period.

ing) as well as ubRMSE (1.06 dB for fortnightly training and 0.93 dB for seasonal training). In the case of combined training target sets, bias for predicted $\hat{\sigma}^0_{VV}$ showed gradual decreasing pattern (e.g., -0.87 dB, -0.59 dB, and -0.10 dB for fortnightly, monthly, and seasonal training, respectively) in accordance with the increase of the training window length. Similar results were revealed for RMSE and ubRMSE in that fortnightly training showed highest magnitude while seasonal training showed the lowest magnitude. These statistical results illustrate that more training data with a given temporally sparse datasets often results in generating a more robust SVM although the training matrix becomes more complex containing information from different types of snow (e.g., wet versus dry, shallow versus deep).

Domain-averaged statistics during the snow ablation depicted in Figure 2.13

depicted analogous statistical behavior with that of the snow accumulation period in that magnitude of bias, RMSE, and ubRMSE from three different training target sets were decreased in accordance with the elongation of training window, in general. For example, predicted $\hat{\sigma}_{VV}$ using ascending-only and combined training target sets revealed a decreasing trend in bias and RMSE. Similar behavior was observed for $\hat{\sigma}_{VH}$ using the combined training set such that bias decreased from -1.00 dB to -0.83 dB, 2.09 dB to 1.88 dB, and 1.52 dB to 1.36 dB for bias, RMSE, and ubRMSE, respectively. At the same time, however, an opposite statistical behavior was sometimes observed during the snow ablation period in that the magnitude of statistics were increased as the length of training window elongated. For instance, the magnitude of bias from predicted $\hat{\sigma}_{VH}$ using ascending-only training set was increased from monthly training (-0.89 dB) to seasonal training (-0.91 dB). Similarly, ubRMSE of $\hat{\sigma}_{VV}$ using ascending-only training was slightly increased from monthly training (1.05 dB) to seasonal training (1.11 dB) even if seasonal training contains the largest number of training data at a given location. Further, ubRMSE for the combined training set for $\hat{\sigma}^0_{VH}$ also showed a slight increasing trend as the training window was elongated from fortnightly to monthly (Figure 2.13). These phenomena provide evidence that merging observations from different snow conditions within the same training matrix introduces more random errors in the predicted backscatter. Overall, the results bring up questions regarding which training window is the most adequate for a robust SVM. Among the different training window approaches, the fortnightly training period has the best likelihood of physically constraining either a dry snow or wet snow signal within the single training matrix. On the other

hand, the monthly and seasonal training periods have a higher likelihood of containing a mixture of wet and dry snow conditions, which leads to a mixture of scattering (dry) and absorbing (wet) electromagnetic responses for the same location that than leads to a SVM with less predictive efficacy. This brings about the conundrum of quality of training data versus the number of training data within a sparse set of training targets in both space and time. In the limit as the number of training data approach infinity, the physically-constrained approaches should be superior, but is not always evident given the severity of the data sparsity in this study.

2.4.3 Influence of Separate Training for Dry versus Wet Snow Conditions

Statistical analysis of predicted backscatter using different sets of training targets (i.e., ascending-only, descending-only, and combined datasets) and training windows (i.e., fortnightly, monthly, and seasonal) emphasized that the mixture of different electromagnetic responses from different snow conditions resulted in weakened SVM performance. Section 2.3.3 also highlighted the inherent characteristics of C-band signal during dry versus wet snow conditions. The focus here is on examining the influence of different snow wetness conditions toward SVM prediction by comparing the statistics of predicted backscatter with and without explicit dry snow and wet snow delineation based on Noah-MP snow liquid water content estimates.

Previous research has used a variety of methods to characterize snowmelt. For example, diurnal amplitude variation [102] and cross-polarized gradient ratio [1] has

been used for PMW observations to detect snowmelt. In this study, however, snow liquid water content from the Noah-MP simulation was utilized as a constraint for delineating dry snow versus wet snow. More specifically, SVMs for dry snow and wet snow pixels were generated separately while four input datasets (e.g., SWE, snow density, snow liquid water content, and top layer snow temperature) remained the same. Note that snow wetness estimates from Noah-MP are not perfect. However, considering the absence of ground-based snow wetness measurements, it is assumed here that the model-based estimates are a feasible proxy. Using the Noah-MP snow wetness estimates, wet snow is defined here simply as when the snow liquid water content was greater than zero. Similar to the previous sections, three different sets of training targets (i.e., ascending-only, descending-only, and combined training sets) were used separately in this section.

Figure 2.14 shows the spatial distribution of bias for predicted co-polarized backscatter, $\hat{\sigma}^0_{VV}$, using the three different training sets without and with dry snow versus wet snow delineation via Noah-MP. Note that the increase in white space in the bottom row (relative to the top row) is due to fewer training targets being available, and hence, fewer SVMs that can be generated due to the increased data sparsity. The use of modeled liquid water content from Noah-MP added another physical constraint during SVM training. As such, the size of the training matrix was further reduced, which resulted in fewer trained SVMs that in turn reduced the spatial coverage. Comparing Figure 2.14(a)-(c) with Figure 2.14(d)-(f), generating separate SVMs for dry and wet snow pixels modestly resulted in reducing the magnitude of bias. Table 2.7 also shows that separate training for dry and wet snow

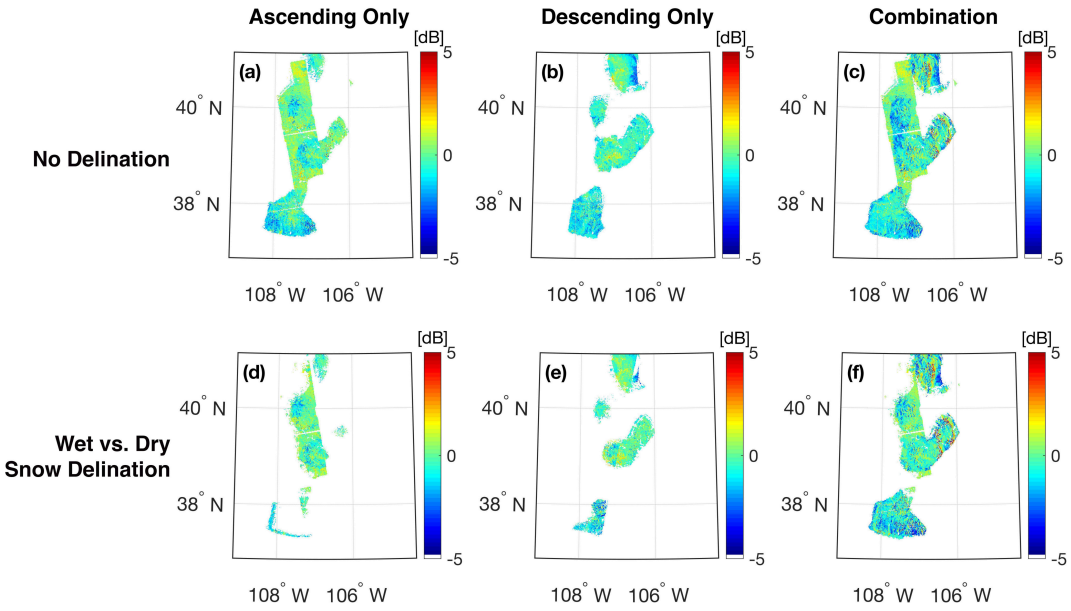

Figure 2.14: Spatial distribution for bias of predicted $\hat{\sigma}^0_{VV}$ without explicit dry versus wet snow delineation (top row) and with explicit dry versus wet snow delineation (bottom row) from Sep. 2016 to Aug. 2017. The different columns represent the training sets for ascending only (left column), descending only (middle column), and combination of ascending and descending (right column).

resulted in improving most of the domain-averaged statistics of predicted backscatter at both polarizations in spite of the reduced number of targets for use during training. For the ascending-only and descending-only training target sets, the bias, RMSE, and ubRMSE were slightly improved only when using the explicit dry versus wet snow delineation during training. Most notably, $\hat{\sigma}^0_{VH}$ from the descending-only training set showed significant improvement in bias from -0.72 dB to -0.40 dB. Even though the combined training set also showed slight improvement in ubRMSE for both $\hat{\sigma}^0_{VV}$ and $\hat{\sigma}^0_{VH}$, the bias and RMSE were slightly increased when using the explicit dry versus wet delineation during training. This phenomenon was due, in large part, to the different observation times for ascending and descending overpasses. As

Table 2.7: Domain-averaged statistics of predicted backscatter using the three different training sets (a) without dry versus wet snow classification and (b) with dry versus wet snow classification based on Noah-MP. Statistical evaluations are based on comparison to Sentinel-1 observations from Sep. 2016 to Aug. 2017 *not* used during training.

(a)	**Bias [dB]**		**RMSE [dB]**		**ubRMSE [dB]**	
Datasets	$\hat{\sigma}^0_{VV}$	$\hat{\sigma}^0_{VH}$	$\hat{\sigma}^0_{VV}$	$\hat{\sigma}^0_{VH}$	$\hat{\sigma}^0_{VV}$	$\hat{\sigma}^0_{VH}$
Ascending-only	-0.16	-0.48	1.38	1.12	1.03	0.73
Descending-only	-0.60	-0.72	1.58	1.36	1.23	0.90
Combination	-0.48	-0.72	2.22	1.77	1.86	1.36
(b)	**Bias [dB]**		**RMSE [dB]**		**ubRMSE [dB]**	
Datasets	$\hat{\sigma}_{VV}$	$\hat{\sigma}_{VH}$	$\hat{\sigma}_{VV}$	$\hat{\sigma}_{VH}$	$\hat{\sigma}_{VV}$	$\hat{\sigma}_{VH}$
Ascending-only	-0.12	-0.39	1.37	1.09	1.05	0.69
Descending-only	-0.30	-0.40	1.52	1.23	1.16	0.88
Combination	-0.54	-0.67	2.30	1.78	1.59	1.14

Note: All statistics are different at $p = 0.05$ *using Wilcoxon signed rank sum test*

mentioned earlier, the different observations at different times (overpasses) will often have different snow conditions depending on the diurnal melting and refreezing cycle. Accordingly, even if the specific pixel is classified as a wet or dry snow pixel based on the modeled snow liquid water content, the combined overpass training set is often composed of a mixture of both wet snow and dry snow signals.

In addition to the comparison of accuracy before and after applying the dry versus wet snow delineation, statistics of predicted backscatter based on *explicit* dry versus wet snow delineation were classified into dry and wet snow pixels and analyzed in order to evaluate the efficacy of the physically-constrained SVM (Figure 2.15). Separation of dry and wet snow pixels also relies on the liquid water content estimates from Noah-MP. For the domain-averaged bias, dry snow periods showed

slightly better performance than for wet snow. $\hat{\sigma}^0_{VV}$ over dry snow pixels yielded a bias of -0.15 dB while wet snow pixels showed comparable or slightly higher magnitude of bias with -0.31 dB. The results showed that predicted backscatter over dry snow and wet snow pixels using ascending-only training exhibited comparable statistical performance. Similar behavior was observed with $\hat{\sigma}^0_{VH}$ with a domain-averaged bias of -0.43 dB and -0.51 dB for dry and wet snow, respectively. In terms of RMSE and ubRMSE, dry and wet snow pixels showed comparable statistical results. For example, $\hat{\sigma}^0_{VV}$ over dry snow pixels yielded RMSE and ubRMSE of 1.38 dB, and 1.09 dB, respectively, which were similar for wet snow pixels (1.37 dB for RMSE and 1.13 dB for ubRMSE). Similarly, RMSE of $\hat{\sigma}^0_{VH}$ over dry snow pixels was 1.08 dB which showed similar statistical performance as for wet snow pixels (1.09 dB). As mentioned earlier, ascending overpasses often have relatively wetter surface snow conditions due to the small amount of diurnal melting during the afternoon. It is believed that this leads to the similar statistical behavior over dry snow pixels versus wet snow pixels using the ascending-only training set.

In the case of descending-only and combined training sets, wet snow pixels showed a lower magnitude of bias than did dry snow pixels. Bias of $\hat{\sigma}^0_{VV}$ and $\hat{\sigma}^0_{VH}$ using the descending-only training set was -1.45 dB and -1.40 dB for dry snow while it was reduced to -0.11 dB and -0.23 dB during wet snow conditions. Similar behavior was observed for combined training sets in that bias of wet snow pixels (-0.16 and -0.25 dB for $\hat{\sigma}^0_{VV}$ and $\hat{\sigma}^0_{VH}$, respectively) showed a smaller magnitude than that of dry snow pixels (-0.82 and -0.96 dB for $\hat{\sigma}^0_{VV}$ and $\hat{\sigma}^0_{VH}$, respectively). Moreover, descending-only training sets showed lower RMSE at wet snow pixels

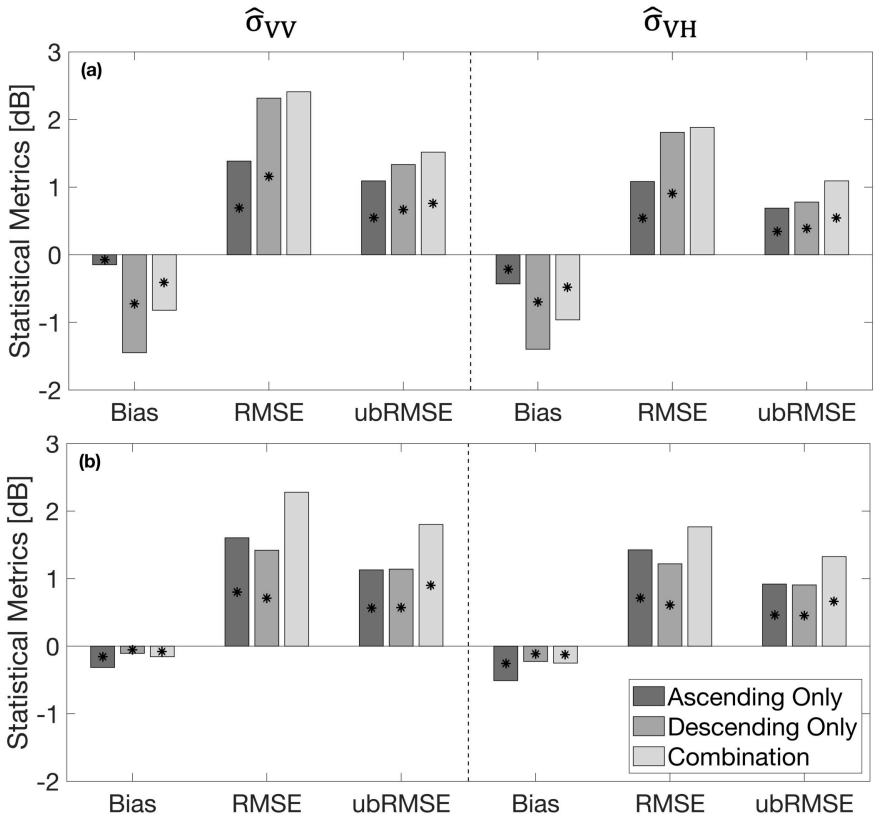

Figure 2.15: Domain-averaged statistics of predicted backscatter for three different training approaches at (a) dry snow locations and (b) wet snow locations during the validation period of Sep. 2016 to Aug. 2017. Asterisks indicate statistically significant differences between all pairs using the Wilcoxon signed rank sum test ($p < 0.05$).

than dry snow pixels at both polarizations (Figure 2.15).

In general, C-band backscatter has a deeper penetration depth for dry snow ($\sim$20 m) than wet snow ($\sim$3 cm) due to the difference in snowpack properties (i.e., snow grain size, snow density, and snow liquid water content) [140]. Furthermore, C-band backscatter during dry snow conditions, in general, is dominated by backscatter at the snow-land interface compared to other components listed in Equation 1.1 (i.e., volume scattering or air-snow interface scattering) [129]. This behavior leads to no significant difference between backscatter from snow-free conditions versus shal-

low, dry snow conditions [150], while volume scattering (and hence backscatter) still plays an important role to total backscatter during deep, dry snow conditions [131]. Conversely, backscatter during wet snow conditions is generally controlled by either backscatter from the air-snow interface or by volume scattering depending on the snow wetness [129]. At the same time, the influence of backscatter from the snow-ground interface is minimized due to the increase of absorption. Hence, the backscatter has a relatively larger variability during wet snow conditions as C-band radiation undergoes a large amount of absorption and/or reflection (Figure 2.7). This increased sensitivity during wet snow conditions provides more information content for the SVM to yield better predictions regarding C-band backscatter (and its relation to snow mass) as compared to the SVM predictions during dry snow conditions when C-band backscatter is predicated more on backscatter from the snow-land interface rather than volume scattering associated with terrestrial snow mass. These differences in the fundamental physics result in a better statistical performance as related to snow mass when the snow is wet rather than dry.

2.5 Conclusions and Future Work

The main goal of this paper was to assess the feasibility of physically-constrained SVMs to predict C-band backscatter over snow-covered terrain in Western Colorado. When considering the first-order physics of scattering and absorption over snow-covered terrain, the influence of training target sets, training window length, and dry versus wet snow delineation on SVM efficacy were examined to develop a

well-trained SVM. Backscatter coefficients observed from Sentinel-1 as well as geophysical variables from Noah-MP over the snow-covered regions were utilized as training targets and input vectors for SVM training, respectively.

Predicted backscatter using the different sets of training targets commonly showed that over 69% of locations with larger negative bias than the lower decile were located within the elevation range of 2500 m to 3500 m. This suggests the reduced sensitivity of C-band backscatter to snow due to the influence of volume scattering in regions with overlying heterogeneous forest cover. Among the different training target sets (e.g., ascending-only, descending-only, and the combination of the two), combining both ascending and descending datasets showed advantages in extending the spatial coverage of prediction (15.2%) due to an increased number of points in time for training. However, this approach degraded the RMSE (2.54 dB for $\hat{\sigma}^0_{VV}$ and 2.06 dB for $\hat{\sigma}^0_{VH}$) and ubRMSE (2.08 dB for $\hat{\sigma}^0_{VV}$ and 1.54 dB for $\hat{\sigma}^0_{VH}$) due to the mixture of different signals during different snow conditions (i.e., dry scattering snow mixed with wet absorbing snow). Ascending-only and descending-only training sets yielded more robust SVM-based predictions during the snow accumulation and ablation periods based on the relationship between diurnal melt, diurnal refreezing, and the corresponding overpass time.

Elongation of the training window length also allows for the usage of more available training data (in time) for SVM training, which results in an increase in the spatial extent of predicted backscatter via the SVMs. More specifically, the spatial coverage of predicted backscatter using the combined training target set and seasonal training window was maximized up to 33.9%. In terms of statistical behavior,

seasonal training showed, in general, slightly better statistical improvements in all three training target sets throughout the validation year. More specifically, the magnitude of bias from the combined training sets with a seasonal training window (-0.10 dB for $\hat{\sigma}^0_{VV}$ and -0.50 dB for $\hat{\sigma}^0_{VH}$) was significantly decreased when compared with that using the fortnightly training window (-0.83 dB for $\hat{\sigma}^0_{VV}$ and -0.95 dB for $\hat{\sigma}^0_{VH}$). Similar behavior was shown when comparing the statistics from the snow accumulation and snow ablation periods while RMSE and ubRMSE for ascending-only and descending-only training sets tended to increase along with elongation of training window. These results suggest that elongation of the training window length can improve the accuracy of predicted backscatter by obtaining more training target sets in space and time. At the same time, however, it was evident that the elongated training window also resulted in a slight degradation in the seasonal variability of the snowpack due to a mixture of signals from different (i.e., dry versus wet; shallow versus deep) snow conditions.

Considering the behavior of C-band backscatter and its dependence on liquid water content within the snowpack, dry and wet snow pixels were trained separately using modeled snow liquid water content from Noah-MP. The results confirmed that separate training of dry versus wet snow pixels resulted in reducing the magnitude of bias, RMSE, and ubRMSE of ascending-only and descending-only training sets. For example, the bias of descending-only was reduced from -0.60 to -0.30 dB for $\hat{\sigma}^0_{VV}$ and -0.72 to 0.40 dB for $\hat{\sigma}^0_{VH}$. Moreover, separate training for dry versus wet snow pixels, and the physical constraints associated with the different electromagnetic responses of the snow, demonstrated different performance at wet snow locations

versus dry snow locations. For instance, the bias of the combined training target set showed -0.82 dB for $\hat{\sigma}^0_{VV}$ and -0.96 dB for $\hat{\sigma}^0_{VH}$ while wet snow pixels showed much lower biases with -0.16 dB for $\hat{\sigma}^0_{VV}$ and -0.25 dB for $\hat{\sigma}^0_{VH}$. This implies that C-band backscatter showed relatively higher sensitivity toward wet snow than dry snow due to the different electromagnetic responses (e.g., scattering versus absorption) depending on the different snow conditions, which influences the penetration depth as well as the dominant scattering component.

In summary, prediction of C-band backscatter over snow-covered land using a physically-constrained machine learning approach suggests that explicit consideration of the first-order physics as related to different scattering mechanisms in accordance with snow conditions is essential in achieving reasonable accuracy. Further, this paper provides a fundamental framework utilizing SVM regression as an observation operator within a data assimilation system to be pursued in a follow-on study in order to improve model-derived snow mass information based on a Bayesian merger of an advanced land surface model with C-band backscatter observations. This paper also highlights the necessity of considering the first-order physics during machine learning training in order to ensure the machine learning algorithm produces the right answer for the right reason.

Chapter 3: Evaluation of GEOS L-Band Microwave Brightness Temperatures using Aquarius Observations over Non-Frozen Land across North America

3.1 Overview

Previous research showed that L-band brightness temperatures (T_b) from SMOS and SMAP demonstrated skill in retrieving soil moisture estimates across the globe while also containing significant uncertainty over densely vegetated areas [45]. This motivates merging L-band microwave observations into a land surface model using a radiative transfer model (RTM) as the observation operator. RTMs have shown the ability to reasonably reproduce L-band T_b [65, 161]. However, prior to conducting a data assimilation experiment to enhance soil moisture estimates, it is important to first explore the error characteristics and uncertainties in the observation operator (RTM in this case) prior to conducting assimilation.

The overall objective of this chapter is to investigate the performance of the zero-order tau-omega RTM embedded in the Goddard Earth Observation System (GEOS) through comparison with T_b observations collected by the Aquarius L-band radiometer over North America. More specifically, performance of RTM-derived T_b

was investigated in terms of soil hydraulic parameters (e.g., porosity and wilting point) and vegetation types. Section 3.2 describes the zero-order tau-omega RTM as well as the calibration schemes of RTM parameters. Section 3.3 provides the datasets utilized as part of this study. Section 3.4 describes the statistical indices used for evaluating RTM-derived T_b. Description of the the statistical performance of RTM-derived T_b is presented in Section 3.5 and key findings and conclusions are summarized in Section 3.6.

3.2 L-band Radiative Transfer Model

3.2.1 Zero-Order Tau-Omega Model

A radiative transfer model (RTM) is a mathematical formulation describing the propagation of electromagnetic radiation through a medium accounting for emission, absorption, transmission, and scattering [32]. A zero-order tau-omega model is one of the widely used solutions to solve the radiative transfer equations and estimate L-band T_b [145]. Figure 3.1 describes the schematic of a tau-omega model to estimate L-band T_b. Brightness temperature at the top of the atmosphere, $T_{b,TOA}$, consists of upward and downward atmospheric radiation along with surface and vegetation components. The tau-omega model simplifies T_b estimation at the top of atmosphere $T_{b,TOA}$, at polarization $p = (H, V)$ as:

$$T_{b,TOV,p} = T_s(1 - r_p)A_p + T_c(1 - \omega_p)(1 - A_p)(1 + r_p A_p) + T_{b,ad,p} r_p A_p^2 \quad (3.1)$$

$$T_{b,TOA,p} = T_{b,au,p} + T_{b,TOV,p} \times \exp(-\tau_{atm,p}) \quad (3.2)$$

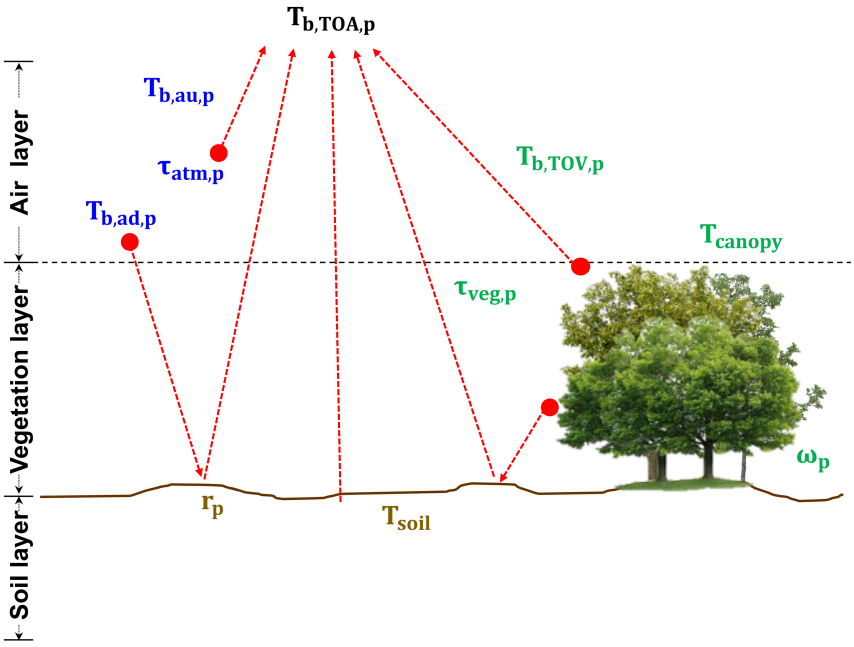

Figure 3.1: Conceptual drawing for the tau-omega model used to estimate L-band T_b.

where $T_{b,TOV,p}$ [K] is the brightness temperature at top of the vegetation, T_s [K] is the surface soil temperature, and T_c [K] is the canopy temperature that is assumed to equal T_s [53]. $T_{b,au,p}$ [K] and $T_{b,ad,p}$ [K] are the upward and downward atmospheric radiation, respectively. r_p [-] is the rough surface soil reflectivity, ω_p [-] is the scattering albedo, A_p [-] is the vegetation attenuation, and $\tau_{atm,p}$ [-] is the atmospheric optical depth used for representing atmospheric attenuation. Note that atmospheric components (e.g., $T_{b,au,p}$, $T_{b,ad,p}$, and $\tau_{atm,p}$) follows the Pellarine et al. [161].

Vegetation attenuation, A_p, is calculated through the vegetation opacity model

proposed by Jackson and Shumugge (1991) [100] as:

$$A_p = \exp(-\frac{\tau_{veg,p}}{\cos\theta}) \tag{3.3}$$

$$\tau_{veg,p} = b_p \times VWC = b_p \times LEWT \times LAI \tag{3.4}$$

where θ [rad] is the incidence angle and $\tau_{veg,p}$ is the vegetation opacity at nadir. $\tau_{veg,p}$ [-] is a function of the vegetation structure parameter b_p [-] and the vegetation water content VWC [kg m^{-2}]. VWC is calculated as the product of leaf equivalent water thickness, $LEWT$ [kg m^{-2}], and leaf area index, LAI [m^2 m^{-2}]. The rough surface reflectivity r_p in Equation (3.1) is calculated as a function of smooth surface reflectivity R_p via:

$$r_p = [(1-Q)R_p + QR_q]\exp(-h\cos^N\theta) \tag{3.5}$$

where Q [-] is the polarization mixing factor due to surface roughness, N [-] is the angular dependence, and q indicates polarizations (V, H) when $p = (H, V)$. The smooth surface reflectivity, R_p, is computed from the Fresnel equations, which is dependent on the soil dielectric constant that varies with soil moisture [209]. The dielectric constant formulation used in the RTM is based on Wang and Schmugge [215]. h [-] is the effective roughness height parameterized with stepwise function where:

$$h = \begin{cases} h_{max} & \text{SM} \leq \text{wt} \\ h_{max} + \frac{h_{min}-h_{max}}{poros-wt}(SM - wt), & \text{wt} < \text{SM} \leq \text{poros} \end{cases} \tag{3.6}$$

where $poros$ [m^3 m^{-3}] represents porosity and wt [m^3 m^{-3}] is the transitional soil moisture calculated as a function of wilting point [215]. h_{max} and h_{min} represent

the roughness height when soil moisture is at saturation and less than transitional soil moisture, respectively. Based on Equation 3.6, effective roughness height is dependent on the soil moisture as different amounts of liquid water results in a variation of the dielectric constant, and in turn, influences the effective roughness height.

From Equation (3.1), it is evident that vegetation attenuates the microwave emission from the soil and simultaneously adds its own contribution to the measured microwave T_b. In addition, precipitation interception by overlying vegetation and ground litter also affects microwave emission from the soil [88]. The RTM employed in this study neglects interception and littering effects [53].

3.2.2 RTM Parameter Calibration Scheme

The GEOS RTM utilizes several state variables (e.g., soil temperature, surface soil temperature, and vegetation water content) from the NASA Catchment Land Surface Model [115]. As the RTM is composed of various parameters described in Section 3.2.1, calibration of the RTM parameters is essential to obtain the climatologically unbiased T_b estimates from the model [53]. Among the various parameters, effective roughness height (h), scattering albedo (ω), and the vegetation structure parameter (b_p) are regarded as important parameters in terms of reducing the uncertainties for RTM-derived T_b [53,171]. Accordingly, these parameters were calibrated against multi-angular SMOS Level 1 version 504 T_b observations to compute the T_b estimates at the top of vegetation for both horizontal and vertical polarizations.

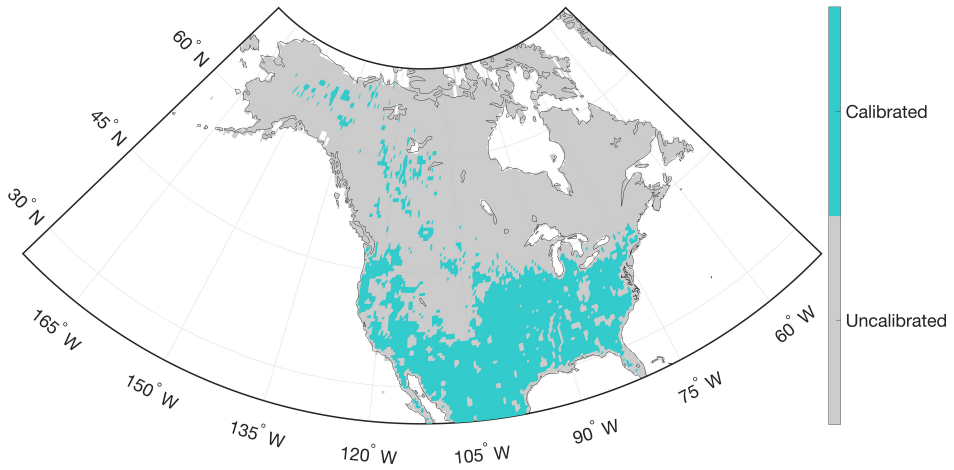

Figure 3.2: Maps of calibrated and uncalibrated area across the study domain.

During the calibration, a particle swarm optimization search algorithm [107] was employed in order to remove the long-term mean and standard deviation of T_b, and in turn, resulted in minimizing the climatological difference between different datasets [53]. Figure 3.2 depicts the maps of calibrated and uncalibrated regions across the study domain. Note that the regions near inland water bodies and the northern part of the study area were not included for calibration scheme as these areas have limited number of SMOS observations during non-frozen soil conditions for use during calibration. For the regions where SMOS observations are unavailable for calibration, these RTM parameters were filled in by using an average of calibrated parameters for other regions with the same vegetation class.

There are several parameters not selected for the calibration. For example, parameters regarding soil hydraulic parameters (e.g., porosity and wilting point) were not included in calibration scheme in order to maintain the consistency with

soil temperature and soil moisture derived from GEOS [53]. Moreover, several RTM parameters such as leaf equivalent water thickness (LEWT) and angular dependence (N_{r_p}) were not selected for calibration as these parameters are indirectly calibrated using the effective roughness height (h) and vegetation structure parameter (b_p). For these parameters, literature-based lookup tables which were used in SMAP soil moisture calculation as well as other RTMs (e.g., L-MEB, LSMEM, and CMEM) values associated with each vegetation class were assigned.

RTM T_b estimates are generated globally every 3 hours on the 36-km Equal EASE grid [23] in terrestrial areas with non-frozen soil conditions. Prior to calibration, the available SMOS observations underwent extensive quality control. L-band microwave signals are often prone to contamination by radio frequency interference (RFI) [157] that arises from a variety of transmitters used in communication applications. As the accuracy of L-band T_b is significantly degraded due to the RFI corruption, large portions of Europe and Asia were masked out due to strong RFI contamination. During the RTM calibration process using SMOS, further quality control was applied during frozen soil conditions when the model-based land surface temperature was less than 273.4 K. The tau-omega model used here [53] is only applicable during non-frozen soil conditions. Furthermore, SMOS observations collected near water bodies, during intense precipitation events (i.e., precipitation $>$ 10 mm/h), or in the presence of snow cover (i.e., snow water equivalent $> 10^{-4}$ kg m^{-2}) were excluded from calibration.

3.3 Datasets

3.3.1 Aquarius Satellite Mission

The Aquarius mission is a joint collaboration between NASA and the Argentinian space agency, Comisión Nacional de Actividades Espaciales (CONAE), with participation from Brazil, Canada, France, and Italy. Aquarius was launched on 10 June 2011 and ended on 8 June 2015 due to a hardware failure [124]. The primary objective of the Aquarius mission was to monitor the seasonal variation of sea surface salinity in global scale. The Aquarius instrument is onboard the Argentine Satellite de Applicaciones Cientificas-D (SAC-D) observatory, a sun-synchronous, polar-orbiting satellite with an altitude of 657 km [17]. Aquarius is a combination of three L-band (1.413 GHz) passive radiometers and L-band active scatterometer (1.26 GHz). The T_b observations employed in this study are derived only from the passive radiometers.

L-band T_b observations in this study are obtained from radiometers over the non-frozen soils because the primary focus in this chapter is soil moisture. Three passive radiometers provide T_b observations at a spatial resolution (i.e., approximate field-of-view) of 76 km $\times$ 94 km, 84 km $\times$ 120 km, and 96 km $\times$ 156 km, with incident angles of 29.36°, 38.49°, and 46.29°, respectively. These incident angles are denoted as beam #1, beam #2, and beam #3, respectively. The minor axis of each beam is in the along-track direction while the major axis is aligned in the cross-track direction. Each radiometer is directed toward the night side of the Earth in order to

avoid sun glint. Aquarius observations have a 7-day revisit frequency with ascending and descending overpasses around 6 a.m. and 6 p.m. local time, respectively.

The Aquarius instrument went through a pre-launch and post-launch calibration in order to improve the accuracy of observed T_b [165]. Pre-launch calibration includes the internal and external (a.k.a. laboratory test) receiver calibration as well as calibration of the antenna switch-matrix. Post-launch calibration includes the correction of diode temperature, exponential drift, antenna patterns, RFI, and cold-sky calibration [18]. After the pre- and post-launch calibration, the atmospheric contribution was removed when processing the Level-1 product to a Level-2 T_b product. This study utilized Level-2, version-4 Aquarius T_b provided by the NASA Jet Propulsion Laboratory (JPL; `ftp://podaac.jpl.nasa.gov`) in the Hierarchical Data Format (HDF5).

3.3.2 Preprocessing of Aquarius Observation

Besides the calibration, Aquarius T_b underwent post-processing. As the primary objective of this chapter is to evaluate the RTM-derived T_b, the individual Aquarius overpasses were resampled onto the 36-km Equal-Area Scalable Earth (EASE) grid [23], which is the same grid used for the Catchment simulations. For a given orbital track, the individual Aquarius T_b observations that were centered within a particular EASE grid cell were identified and then used to compute a mean T_b value for that EASE grid cell. If more than one Aquarius observation (over a collection period of a few seconds) fell within a single EASE grid cell, then the arith-

metic average was applied to that entire cell. In addition, the value applied at a single cell center was also applied to the relevant neighboring cells (as a function of look angle) such that the approximate field-of-view for each of the three beams was correspondingly approximated on the relatively fine-scale 36-km EASE grid. The process was repeated for each of the three beams for every Aquarius overpass during the period 25 Aug 2011 through 8 Jun 2015, which represents the entire Aquarius measurement record.

After preprocessing, both the RTM-based T_b estimates (for all three beams) and the Aquarius T_b observations were properly geolocated in space and time for subsequent statistical analysis. In order to focus on terrestrial soil moisture estimates, 36-km EASE grid cells with a water fraction greater than 0.05 were excluded from the analysis because the observed Aquarius T_b's did not represent the same physical processes as the RTM output (i.e., the RTM does not account for the presence of surface water impoundments). In addition, grid cells with fewer than 40 observations collected over the course of the four-year study period were excluded from the analysis in order to yield statistically significant statistics.

3.3.3 Soil Classification and Soil Hydraulic Parameters

Soil information used in this chapter was based on the updated soil classification scheme addressed in [50]. This scheme was developed based on the Harmonized World Soil Database version 1.21 provided by Food and Agricultural Organization and the State Soil Geographic (STATSGO2) database from U.S. Department of

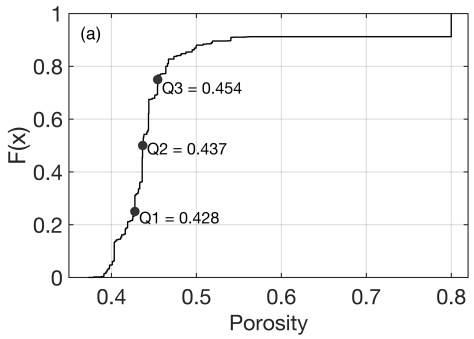

Porosity Range	# of pixels
[0 Q1)	4538
[Q1 Q2)	2733
[Q2 Q3)	3273
[Q3 1]	4022

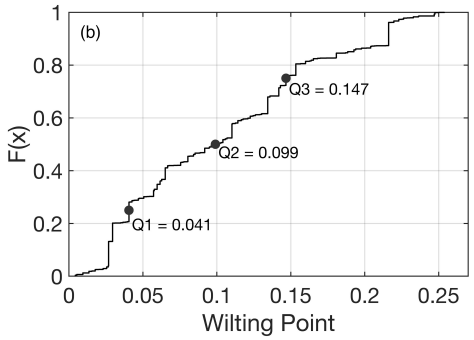

Wilting Point Range	# of pixels
[0 Q1)	4095
[Q1 Q2)	3145
[Q2 Q3)	3692
[Q3 1]	3634

Figure 3.3: Cumulative Distribution Function, F(x), of (a) porosity and (b) wilting point across the study area, including the sampling density of each category. Q1 to Q3 represents the end points of the first to third quartiles, respectively, and define the four categories in subsequent statistical analyses.

Agriculture (USDA) in order to update the soil classification schemes by explicitly considering soil organic content. This classification contains 253 soil classes, including 252 classes from three sets of low to moderate organic carbon categories with 84 different mineral classes defined from the refined soil texture triangle plus one additional peat class with a very high organic content. Based on the updated soil classification scheme, soil hydraulic parameters (SHPs) are determined through the pedotransfer functions suggested by Wosten et al. [222] using the percentage of clay, silt, and organic matter [50]. Among the SHPs, porosity and wilting point are

selected for investigation in this paper as these parameters directly influence the dielectric constant and surface roughness variables that are used within the RTM. For the analysis, porosity and wilting point were divided into four different categories based on the quartile values drawn from the cumulative distribution function of each variable across our study domain (Figure 3.3). For example, Category I collects the value within the range of the zero to first quartile (0% to 25%) while Category IV collects the value from third to fourth quartile (75% to 100%).

3.3.4 Vegetation and Irrigation Data

For the calculation of RTM-derived T_b, land cover information from the Moderate Resolution Imaging Spectroradiometer (MOD12Q1 collection 4 with 500 m spatial resolution) International Geosphere-Biosphere Programme (IGBP) classification schemes [79] was employed. However, the NASA Catchment Land Surface Model (Catchment) uses six broad land cover classes (i.e., Broadleaf evergreen, Broadleaf deciduous, needleleaf, grassland, shrub, and dwarf) which are based on the GLOBCOVER 2009 datasets [138]. Accordingly, 16 global IGBP classes were mapped into six dominant land cover classes across North America in order to subsequently analyze the performance of RTM T_b over different vegetation types. Figure 3.4(a) represents the vegetation classes across the North America. Note that broadleaf evergreen forest was excluded from subsequent analysis as it accounts for less than 5% across the study domain.

Furthermore, as cropland is lumped into the grassland category in the Catch-

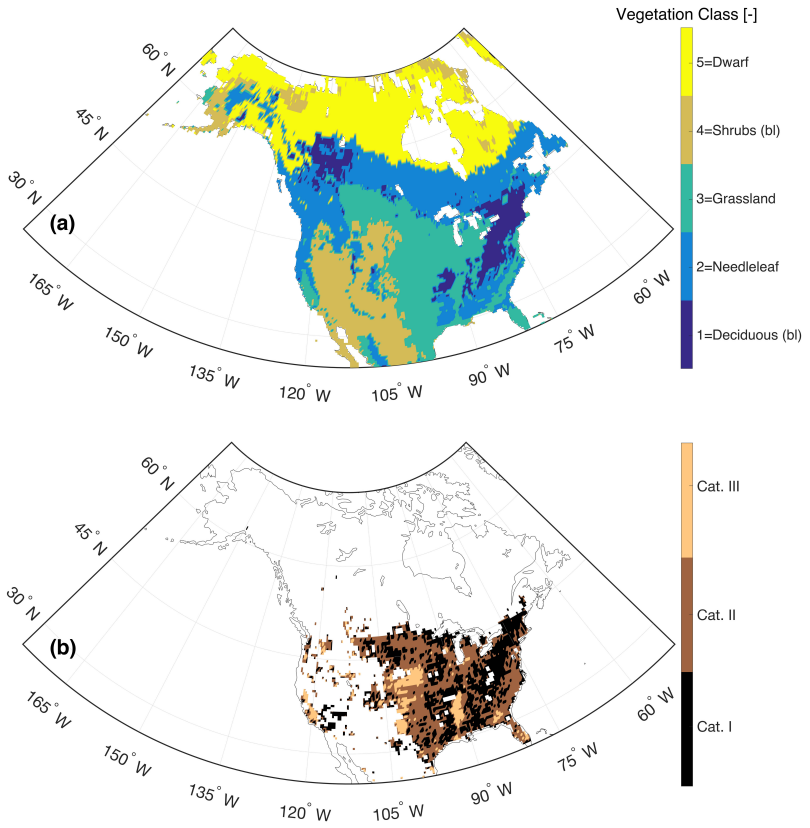

Figure 3.4: Map of (a) vegetation classes discretized based on the Catchment model and (b) irrigation classes based on Global Map of Irrigation Area (GMIA) dataset across the North America. Five sub-categories are divided based on the percentage of irrigation area (e.g., 0-0.1%, 0.1-10%, 10-100%).

ment model, the Global Map of Irrigation Area (GMIA; Siebert et al. [189]) dataset is used to illustrate the percentage of area with actual irrigation relative to the total area in order to analyze the influence of irrigation over the grassland regions in the RTM-derived T_b. As the GMIA dataset has a spatial resolution of 5 arc minutes by 5 arc minutes, it is resampled onto the 36 km EASE grid in order to coincide with the Catchment model. Further, the GMIA dataset was discretized into three sub-categories (i.e., 0-0.1%, 0.1-10%, 10-100%) (Figure 3.4b) based on the derived

CDF.

3.4 Evaluation Metrics

Statistical evaluation of the RTM-based $T_{b,RTM}$ was conducted by calculating bias and root mean square error (RMSE) through comparison with Aquarius T_b observation which can be calculated as:

$$bias = \frac{1}{n}\sum_{i=1}^{n}(T_{b,RTM} - T_{b,obs}) \tag{3.7}$$

$$RMSE = \sqrt{\frac{1}{n}\sum_{i=1}^{n}(T_{b,RTM} - T_{b,obs})^2} \tag{3.8}$$

where n is the number of colocated (in space and time) brightness temperature observations and predictions, $T_{b,RTM}$ [K] is the brightness temperature predicted by the RTM, and $T_{b,obs}$ [K] is the brightness temperature observed by Aquarius. In general, *bias* is a measure of systematic error that indicates the over- or under-prediction of the observation while RMSE accounts for both systematic and non-systematic (random) errors [142]. Additionally, unbiased root mean square error (ubRMSE) [70] was computed, which is the RMSE after first removing the bias.

3.5 Results and Discussions

3.5.1 Comparison between RTM, SMOS, and Aquarius Brightness Temperatures

Prior to analyzing the RTM-derived T_b, Aquarius T_b observations were compared to both SMOS Level 1 version 504 and RTM-derived T_bs colocated in space and time. This analysis is valuable in that different T_b behavior, according to incidence angle, influences the soil moisture retrieval as well as the data assimilation framework. Kerr et al. [108] mentioned that angular dependency of T_b critically influences the determination of surface roughness and vegetation structure parameters, which in turn, affects the accuracy of retrieved soil moisture. Moreover, this analysis can provide potential insights to determine off-diagonal components in RTM-derived T_b error covariance as cross correlations between different incidence angles and polarizations are non-negligible in future DA framework [52].

Figure 3.5 highlights the angular dependency of the spatio-temporal mean T_b across North America from co-located values among SMOS-, RTM-, and Aquarius-based T_b's. The SMOS incidence angles that were closest to the corresponding Aquarius incidence angles are selected for comparison. In general, the mean T_b at horizontal polarization decreases with increasing incidence angle. Conversely, the mean T_b at vertical polarization generally increases in accordance with increasing incidence angle. In terms of the difference among different T_bs, an increase of incidence angle resulted in more difference of RTM T_b versus either SMOS or Aquarius

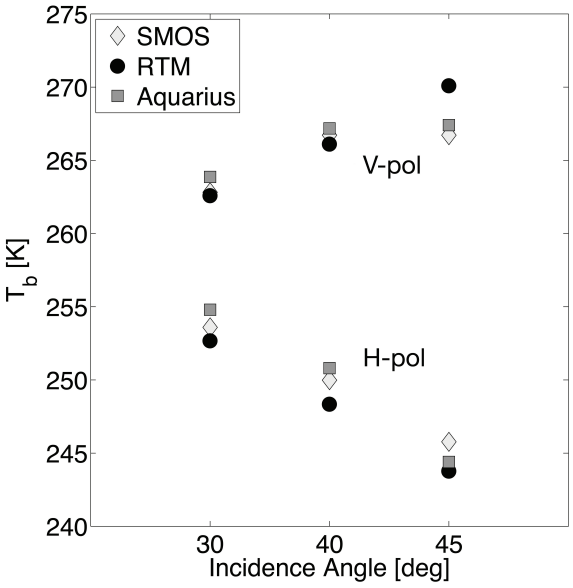

Figure 3.5: Spatio-temporally averaged T_b across the study period (from 25 August 2011 to 7 June 2015) over North America as a function of incidence angle from SMOS, RTM, and Aquarius.

T_b. Kornelsen et al. [112] explained that the increase of incidence angle influences the microwave attenuation from the soil surface as well as the dielectric roughness, which can lead to a higher difference in T_b at higher incidence angle. However, T_b from both SMOS and Aquarius showed little sensitivity (i.e., less than 1 K) from 40° to 45° at vertical polarization.

Figure 3.6 highlights the maps of bias, RMSE, and ubRMSE of the RTM-based estimates for beam #1 at horizontal polarization (relative to Aquarius) with ascending and descending overpasses across North America. Overall computed bias for ascending overpasses ranged from -8.13 K to 8.58 K with domain-averaged bias of 0.79 K (Figure 3.6(a)). In the case of descending overpasses, it showed more negative bias than ascending overpasses (as shown in Figure 3.6(c)) with the bias ranged

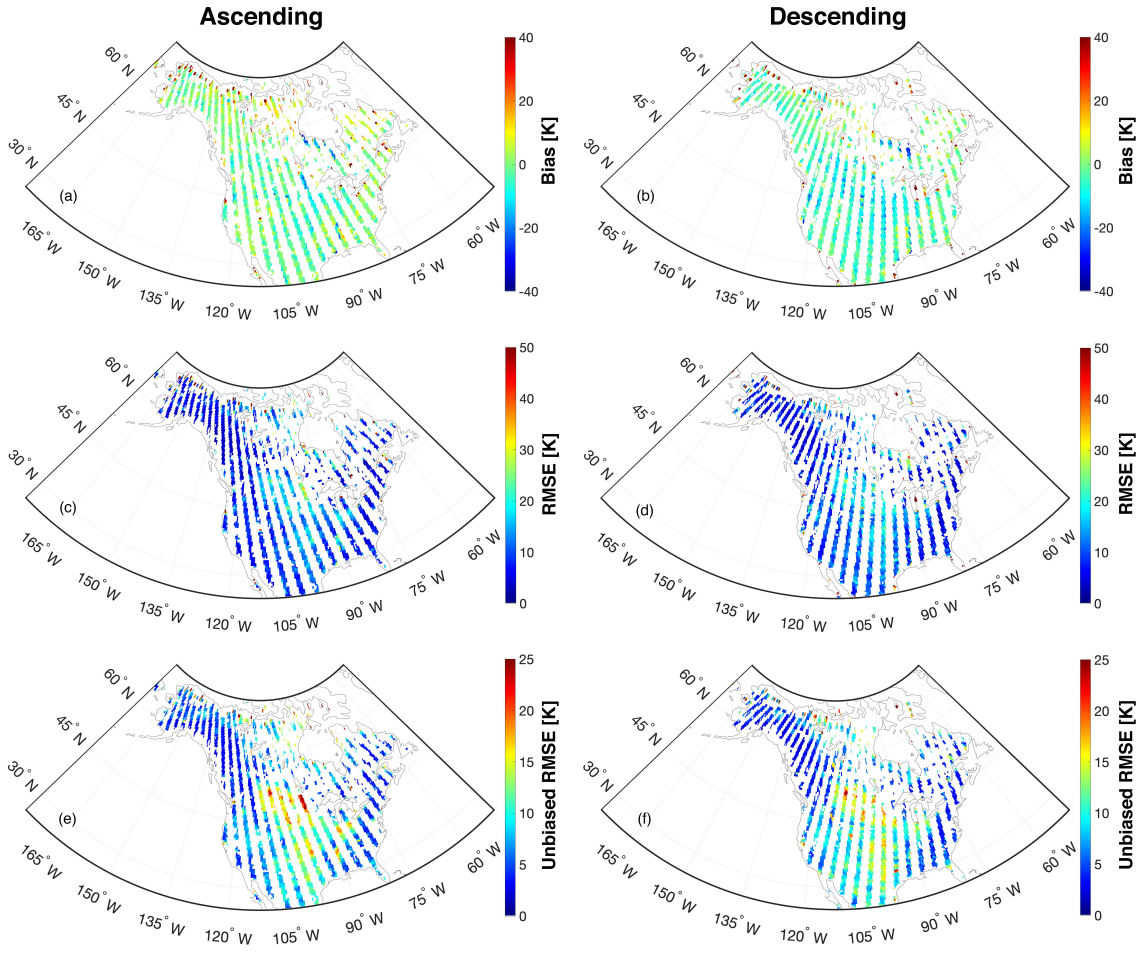

Figure 3.6: Statistical maps of bias (top row), RMSE (middle row), and unbiased RMSE (bottom row) between Aquarius and RTM T_b during the study period (from 25 August 2011 to 7 June 2015) over North America for beam #1 at H-polarization. Left and right columns represent the ascending and descending overpasses, respectively.

between -11.7 K to 4.55 K and a domain-averaged bias of -2.79 K. Similar behavior was observed for both beam #2 and beam #3 across the ascending and descending overpasses with bias ranged from -12.8 K to 8.85 K and -14.1 K to 8.40 K for beam #2 and beam #3, respectively. Opposite signs of biases calculated from ascending and descending overpasses resulted from the different observation times. Aquarius has ascending and descending overpasses around 6 a.m. and 6 p.m. in local time, respectively. Holmes et al. [95] and De Lannoy et al. [53] suggested that the opposite sign of bias from ascending and descending overpasses could result from the large magnitude of diurnal biases in the soil temperature estimated from the land surface model. The northern part of Canada near Lake Winnipeg and Hudson Bay has a relatively high magnitude of negative bias (i.e., greater than -13.3 K) throughout the different beams and polarizations. Locations immediately next to water bodies near the Great Lakes, Great Salt Lake, Lake Winnipeg, and Hudson Bay represented anomalously large, positive biases (approximately 40 K). In addition, some large areas in and around the boreal forest regions in northern Canada show higher bias (18.6 K and 12.7 K for ascending and descending overpasses, respectively), which is also likely due to the presence of significant numbers of sub-grid scale lakes. These phenomena are further exacerbated by the resampling of the Aquarius T_b onto a relatively finer scale grid. That is, Aquarius T_b was oversampled onto the 36-km EASE grid in order to facilitate the comparison with RTM-derived T_b. However, when the footprint of the Aquarius T_b includes open water bodies that extend beyond a particular 36-km EASE grid cell, the resampled, neighboring pixels will still contain information partially contaminated by the nearby open water bodies. Ad-

ditionally, the lack of a module for open water in the current RTM also resulted in some strongly biased T_b simulation results.

RMSE (Figure 3.6(c) and 3.6(d)) and ubRMSE (Figure 3.6(e) and 3.6(f)) statistics for beam #1 ascending and descending overpasses at horizontal polarization showed similar patterns of bias. RMSE of beam #1 at horizontal polarization ranged from 3.99 K to 17.4 K across the different overpasses with domain-averaged RMSE of 11.6 K and 14.9 K for ascending and descending overpasses, respectively. Similarly, ubRMSE mostly ranged from the 2.20 K to 13.1 K throughout the ascending and descending overpasses with domain-averaged ubRMSE of 7.93 K and 7.85 K, respectively. Nearly identical patterns are witnessed for the other beams and polarization combinations (not shown). The RMSEs are mostly within the range of 4.13 K to 18.9 K for both ascending and descending overpasses across the study domain for all three beams at horizontal polarization. However, vertical polarization RMSE results are, in general, smaller than their horizontal polarization counterparts with RMSE values generally ranging from 3.99 to 16.4 K, 4.14 to 15.2 K, and 3.83 to 14.8 K for beams #1, #2, and #3, respectively (not shown). Large RMSE values are found in the northern part of Canada and near large water bodies associated with correspondingly large bias values (see Figure 3.6(a) and 3.6(b).) Unbiased RMSE results are shown in Figure 3.6(e) and 3.6(f) for beam #1 at horizontal polarization, and typically range from 0 to 14.2 K, except in the central United States and Canada, where values typically range from 12.0 to 17.7 K for both ascending and descending overpasses. Similar ranges of unbiased RMSE were found for beams #2 and #3 at horizontal polarization. The ubRMSE values are slightly smaller at ver-

tical polarization and typically range between 10.1 to 15.2 K in the Central United States and between 1.39 to 5.43 K everywhere else.

Besides the statistics over all the pixels across the study domain, statistical performance of calibrated and uncalibrated grid cells using SMOS T_b observations (illustrated in Figure 3.2) were separately evaluated for the purpose of analyzing the influence of calibration on the RTM T_b accuracy. Figure 3.8 and Figure 3.9 represent the statistical performance of ascending and descending overpasses over calibrated and uncalibrated grid cells (depicted in Figure 3.2), respectively. The overall result confirmed that calibrated pixels showed better bias, RMSE, and ubRMSE than uncalibrated pixels. For example, the computed bias for ascending overpass mostly ranged from -7.03 K to 4.00 K (calibrated pixel) and -7.48 K to 8.33 K (uncalibrated pixel) with domain-averaged bias of 0.79 K and 2.17 K for calibrated and uncalibrated pixels, respectively. The descending overpass also showed similar behavior as the ascending overpasses with the calculated bias ranged from -10.1 K to 0.92 K and -9.73 K to 3.43 K for calibrated and uncalibrated pixels, respectively. As most of the regions near water bodies and northern boreal forest were excluded from the calibration (Figure 3.2), results showed a relatively high magnitude of bias, RMSE, and ubRMSE as compared to other regions. In the case of the regions with a high percentage of irrigation (Figure 3.4(b)), both calibrated (Figure 3.7) and uncalibrated (Figure 3.8) pixels showed relatively high bias, RMSE, and ubRMSE as compared to other regions across the different overpasses. Comparing calibrated and uncalibrated pixels, statistics over calibrated pixels showed slight improvement in comparison with uncalibrated regions. Detailed discussion about performance

over irrigated areas is provided in Section 3.5.3.

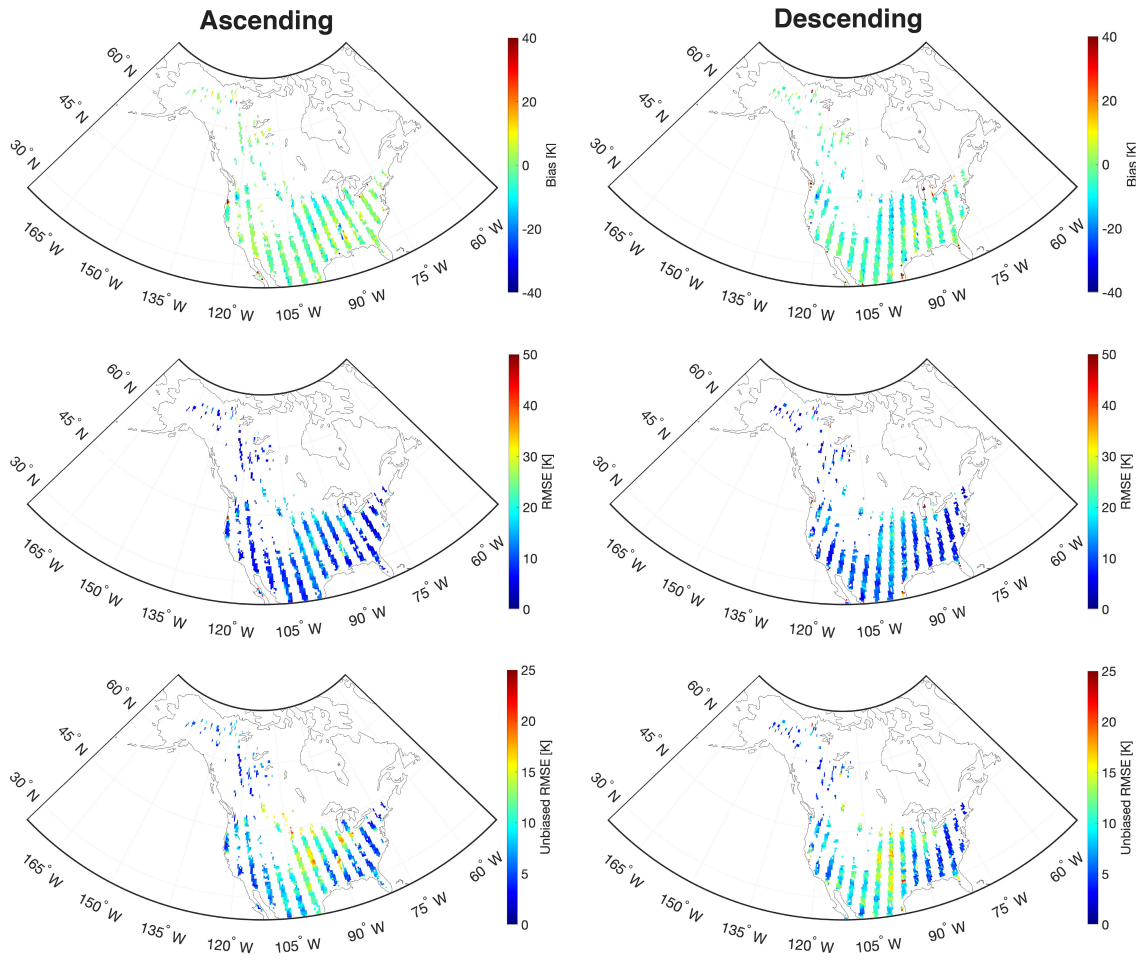

Figure 3.7: Statistical maps of bias (top row), RMSE (middle row), and unbiased RMSE (bottom row) between Aquarius and RTM T_b during study period (from 25 August 2011 to 7 June 2015) at calibrated regions over North America for beam #1 at H-polarization. Left and right columns represent the ascending and descending overpasses, respectively.

3.5.2 Performance as a Function of Soil Hydraulic Parameters

Performance of the RTM-derived T_b is evaluated as a function of soil hydraulic properties (SHPs) across the study domain. Figure 3.9 and Figure 3.10 show the statistical results of the comparison between RTM and Aquarius T_b as a function

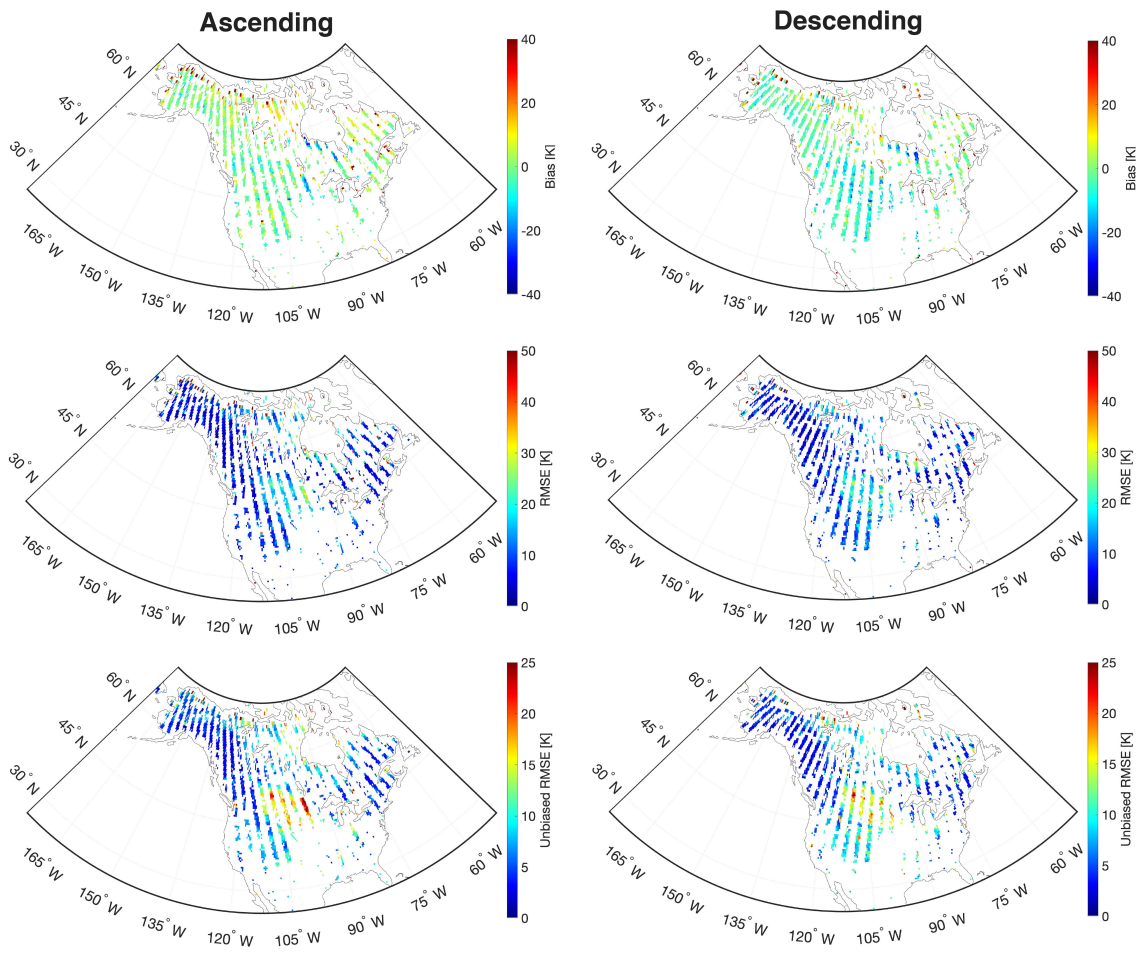

Figure 3.8: Statistical maps of bias (top row), RMSE (middle row), and unbiased RMSE (bottom row) between Aquarius and RTM T_b during study period (from 25 August 2011 to 7 June 2015) at uncalibrated regions over North America for beam #1 at H-polarization. Left and right columns represent the ascending and descending overpasses, respectively.

of porosity and wilting point, respectively. The whisker ranges from the 5th to 95th percentiles of the computed statistics whereas the boxplot highlights the 75th, 50th, and 25th percentiles. According to Figure 3.9, the median bias (i.e., 50th percentile of the boxes shown in the leftmost column of the subplots) is lowest in Category III for ascending overpasses with a value of -0.05 K and Category II for descending overpasses with a value of -1.58 K. Across the different overpasses, the

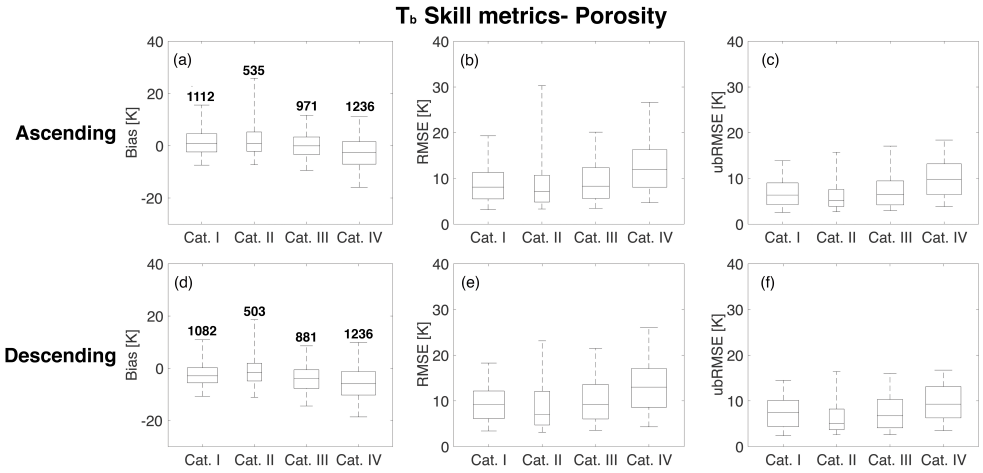

Figure 3.9: Statistical comparison for different porosity categories divided based on the CDF (Figure 3.4a) for beam #1 at H-polarization. The different rows show results for ascending and descending overpasses. The different columns represent the results of bias, RMSE, and unbiased RMSE. Note that numbers above the boxes indicate the number of samples for each category.

highest porosity (Category IV) corresponds to the poorest agreement between the RTM T_b estimates and the Aquarius T_b observations for both ascending (-2.62 K) and descending (-5.94 K) overpasses. RMSE and ubRMSE plots presented in the second and third columns of Figure 3.9 also revealed that the highest porosity category showed the highest median values of 11.9 K (RMSE) and 9.83 K (ubRMSE) for ascending and 13.0 K (RMSE) and 9.31 K (ubRMSE) for descending overpasses. Statistics over calibrated pixels also showed similar behavior in that the highest porosity category revealed the highest median bias.

Similar to the behavior of porosity, a higher wilting point, in general, corresponds to a weaker agreement between the RTM T_b estimates and the Aquarius T_b observations (Figure 3.10). Median bias for these four categories are 1.41 K, 0.50

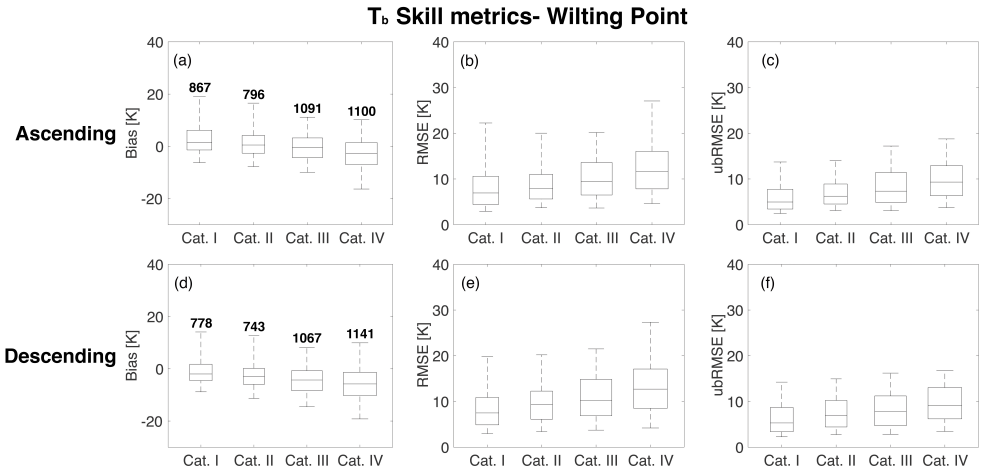

Figure 3.10: Statistical comparison for different wilting point categories divided based on the CDF (Figure 3.4b) for beam #1 at H-polarization. The different rows show results for ascending and descending overpasses. The different columns represent the results of bias, RMSE, and unbiased RMSE. Note that numbers above the boxes indicate the number of samples for each category.

K, -0.40 K, and -2.67 K for ascending overpasses and -1.98 K, -2.89 K, -4.29 K, and -5.80 K for descending overpasses, respectively. Similar behavior was shown for calibrated pixels over both ascending and descending overpasses in that the highest median bias was shown at the highest wilting point category (Category IV). RMSE and ubRMSE for the different wilting point categories also suggest more RTM uncertainty in the highest wilting point category (Category IV) with values of 11.7 K (RMSE) and 9.32 K (ubRMSE) for ascending and 12.7 K (RMSE) and 9.15 K (ubRMSE) for descending overpasses, respectively.

High values of uncertainties for RTM T_b in soils with large porosity or large wilting point can be explained through the influence on the surface roughness and dielectric constant. Soils with higher porosity or wilting point tend to have a higher

fraction of clay [215]. As clay has a large surface to volume ratio (relative to silt), it has an affinity for binding a greater percentage of water molecules, which causes a variation in the dielectric constant [155]. Additionally, an increase in wilting point or porosity will influence the calculation of effective roughness height in the RTM (Equation 3.6) when the soil moisture is within the range of transition point and porosity [53]. Improper parameter estimation of effective roughness height significantly influences the calculation of surface reflectivity, and in turn, results in reduced accuracy of RTM derived T_b. Another possible cause is related to the lack of SMOS observations for use during calibration over regions parameterized as peat, which features high porosity values (approximately 0.8). Furthermore, because peatlands are typically also water-rich, the screening of SMOS data for open water fractions less than 0.05 yielded a limited number of observations in these areas.

3.5.3 Performance as a Function of Vegetation Type

In a similar manner as conducted for soil hydraulic parameters, a statistical evaluation of predicted T_b performance was conducted as a function of vegetation type over ascending and descending overpasses separately. Statistical comparisons for horizontal polarization are shown in Figure 3.5.3. Two forest classes (e.g., broadleaf deciduous and needleleaf forest) showed better agreement with lower median bias, RMSE, and ubRMSE between the RTM and Aquarius observations relative to other vegetation classes. For beam #1 at H-polarization, ascending overpasses showed a median bias of 1.37 K and -0.49 K and descending overpasses showed

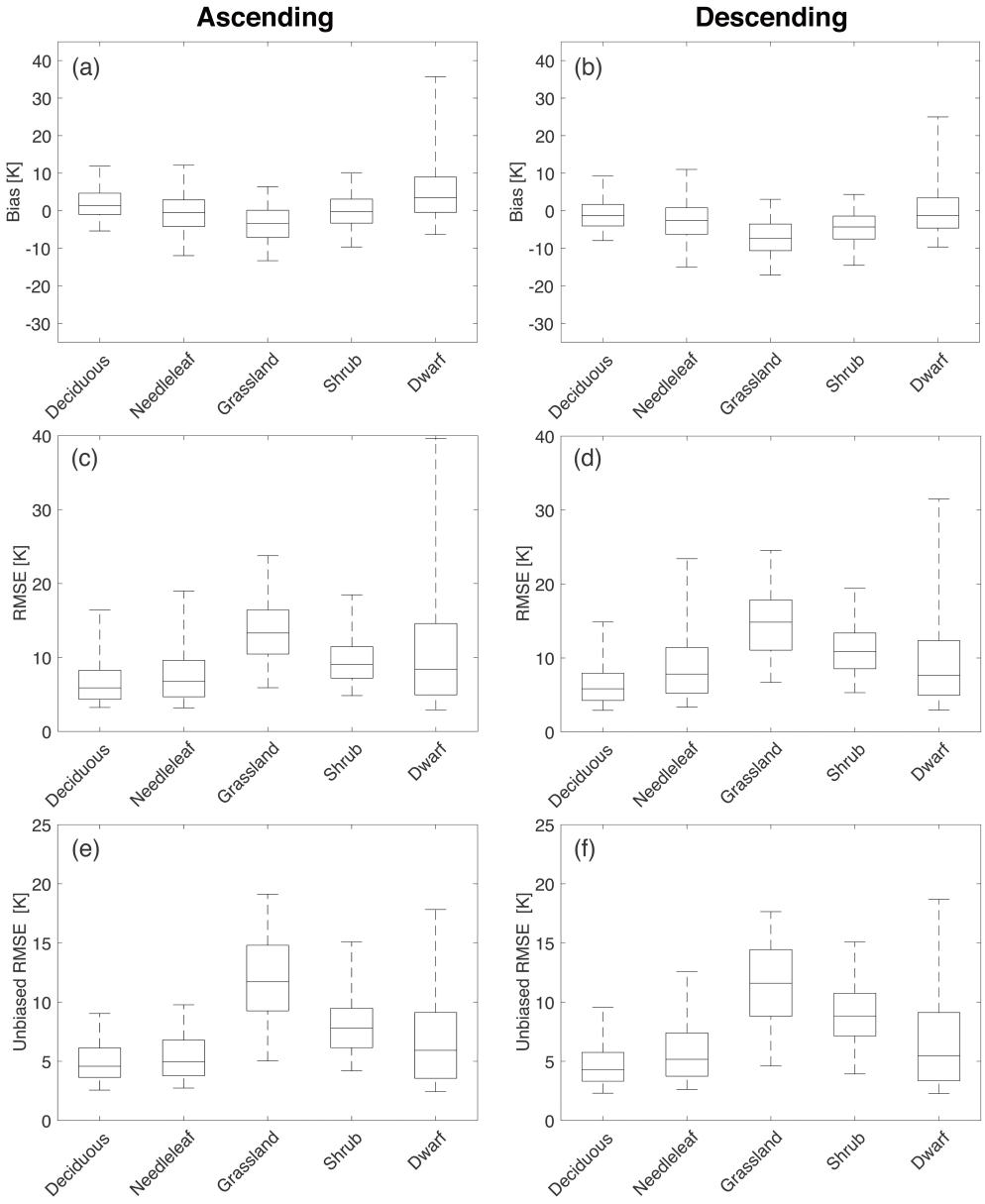

Figure 3.11: Statistical comparison over the dominant vegetation classes (Figure 3.4) for beam #1 at H-polarization. The different rows show results of bias, RMSE, and unbiased RMSE. The different columns show results for ascending and descending overpasses. The upper and lower whiskers represent 95th and 5th percentiles, respectively, whereas the boxes show the median line along with 75th and 25th percentiles.

a median bias of -1.30 K and -2.63 K for broadleaf deciduous and needleleaf forest, respectively. In terms of the range between the 5th and 95th percentile values of bias and RMSE, the grassland and shrub vegetation types showed a more narrow range than did dwarf vegetation. Among the different vegetation classes, grassland showed the largest magnitude of bias, RMSE, and ubRMSE for both ascending and descending overpasses across the study domain. Median biases for ascending and descending overpasses were -3.4 K and -7.35 K, respectively. Similarly, the RMSE and ubRMSE plots presented in Figure 3.5.3(c) through Figure 3.5.3(f) showed poor performance in T_b estimation in grasslands. Ascending overpasses showed the range of RMSE and ubRMSE as 7.42 K to 19.9 K and 5.97 K to 17.4 K, respectively. Similarly, descending overpasses showed the range of RMSE and ubRMSE from 8.31 K to 21.5 K and 5.88 K to 16.2 K, respectively.

De Lannoy et al. [53] also revealed similar behavior in that T_b estimates from the RTM exhibited low uncertainties over dense vegetation while large uncertainties were observed over regions with grassland. Poor performance in grassland regions might result from poorly parameterized agricultural croplands. Mahanama et al. [138] mentioned that irrigated croplands, rainfed croplands, and Mosaic cropland (50-70%) are classified as grassland in the Catchment model. Accordingly, additional analysis was conducted through statistical comparisons for different categories of irrigation area percentage introduced in Section 3.3.3.

Statistical comparison of Aquarius and RTM T_b in accordance with different percentages of irrigated areas within a pixel (via GMIA) revealed that pixels with more than 80% of irrigated area showed the highest bias for ascending and descend-

Table 3.1: Statistical comparison of RTM-derived T_b at beam #1 horizontal polarization depending on the different percentage of pixel with irrigation scheme (I) provided by GMIA datasets. Units for bias, RMSE, and ubRMSE are K.

(a) Ascending	I≥10%	0.1%≤I<10%	I <0.1%
# of samples	138	521	202
bias	-4.95	-3.29	-2.80
RMSE	14.3	14.0	13.8
ubRMSE	12.0	11.8	12.5
(b) Descending	I≥10%	0.1%≤I<10%	I <0.1%
# of samples	192	494	159
bias	-7.81	-6.06	-6.03
RMSE	16.7	15.4	13.5
ubRMSE	11.8	11.6	11.0

ing overpasses (Table 3.1). Moreover, according to Figure 3.4, major irrigation-dominated regions including parts of Nebraska, the Lower Mississippi River Basin, and the California Central Valley [162] are classified as grassland even though they are intensively irrigated croplands. De Lannoy and Reichle [52] and Rains et al. [172] revealed that SMOS observations have potential capability of containing information regarding the irrigation. This result suggests that predicted T_b will likely be less accurate due to a lack of an explicit irrigation scheme in the land surface model (and hence not considered in the RTM) [54]. Irrigation, in general, makes soil moisture wetter and physical temperature lower via relatively cool water added to warm soil in conjunction with evaporative cooling, which leads to a lower T_b. Because irrigation is not explicitly accounted for the Catchment model, uncertainties of soil moisture during irrigation tend to increase. As the soil moisture underestimates in the model, it leads to an overestimate of the effectiveness roughness height in the RTM based on Equation 3.6 depending on the magnitude of soil moisture in comparison with wilting point and porosity. These phenomenon result in underestimation of surface

reflectivity (Equation 3.5), and in turn, underestimation of surface reflectivity as well as the brightness temperature at the top of atmosphere (Equation 3.1).

3.6 Conclusions and Future Work

The overall objective of the research was to evaluate the RTM-based L-band T_b estimates through comparison with Aquarius T_b observations collected by a space-borne L-band radiometer over North America. The evaluation process was performed as a function of soil hydraulic parameters and vegetation types, which are regarded as two essential factors to be considered when using T_b to retrieve soil moisture. Overall evaluation was conducted for the entire Aquarius period from 25 August 2011 to 7 June 2015. Analyses were performed at all three incidence angles (29.36°, 38.49°, and 46.29°, a.k.a., beams #1, #2, and #3) from Aquarius at both horizontal and vertical polarizations, and for ascending and descending overpasses.

Overall comparison of RTM-derived T_b with Aquarius T_b observations (for both ascending and descending overpasses) revealed that RTM-derived T_b showed good performance with Aquarius T_b across the study domain except within some regions that are not included in the calibration scheme due to a lack of available SMOS observations. Areas near to, or with, dynamic ponding or static lakes exhibited relatively large uncertainties due to the oversampling of Aquarius T_b as well as lack of an open water module in the current RTM. Statistics computed over different soil hydraulic parameters (e.g., porosity and wilting point) revealed that higher porosity and higher wilting point corresponded to poorer statistics due to the variation in

surface roughness and dielectric constant.

Among the vegetation classes, broadleaf deciduous and needleleaf forest yielded the best statistics in terms of bias, RMSE, and ubRMSE. The RTM exhibited better performance in regions of dwarf vegetation as compared to the shrub land and grassland vegetation types. The RTM exhibited the lowest accuracy in grasslands among the five different vegetation classes, which is largely attributed to regions of agricultural irrigation and a lack of local irrigation schemes as well as a lack of inter-annual crop rotations in the land surface model that serves as the input to the RTM.

In summary, RTM-derived T_b does a reasonable job in reproducing L-band T_b observations from Aquarius over different soil hydraulic properties and vegetation types across North America. Better agreement between the RTM-derived estimates and the Aquarius observations was witnessed with decreasing porosity and wilting point. The RTM-derived T_b produced reasonable statistics for most vegetation types while further consideration of cropland (which is classified as grasslands in this study) could improve the accuracy of the RTM. These findings support the usefulness of SMOS T_b observations to calibrate RTM parameters, and in turn, estimate reasonable L-band T_b from the RTM. Furthermore, these findings can be leveraged into a follow-on study by including Aquarius L-band T_b in a data assimilation framework for the purpose of improving soil moisture estimates in a land surface model. For example, as most of the northern part of the study domain was not calibrated due to the presence of abundant sub-grid scale lakes, relaxing the constraints of SMOS T_b with regards to the distance to open water bodies could

assure more SMOS observations for use during calibration. Furthermore, an update of the current RTM by including a module for open water should also be considered. In terms of error characterization, larger observation errors need to be assigned for grassland areas as well as for regions with high porosity soil and high wilting points.

Chapter 4: Estimation of Snow Mass Information through Assimilation of C-band Synthetic Aperture Radar Observations using an Advanced Land Surface Model and Support Vector Machine Regression

4.1 Overview

Beyond the retrieval of snow water equivalent (SWE) and snow depth based on remote sensing imagery, data assimilation (DA) has been widely applied to extend the value of remotely-sensed observations while also enhancing model estimates of snow. The ultimate goal of using DA is to acquire optimal estimates of snow mass information that is superior to both the observations or the model-only estimates. In terms of snow mass assimilation, snow cover estimates (e.g., snow cover area [SCA] and snow cover fraction [SCF]) from optical imagery or brightness temperatures, T_b, from passive microwave (PMW) radiometry have been typically used for updating snow mass. In terms of active microwave (AMW) observations, there are relatively few studies employing space-borne SAR imagery into a DA framework in order to improve estimates of snowmelt runoff and snow stratigraphic profiles [136,164]. The study presented in this section is the first attempt to integrate C-band backscatter

observations into an advanced land surface model (LSM) to improve terrestrial snow mass estimates. Notably, the investigation of a physically-constrained support vector machine (SVM) regression technique developed in Chapter 2 suggests that SVMs can serve as an observation operator in terms of snow mass assimilation. Accordingly, this chapter is intended to address the scientific hypothesis that integration of the SVM regression into a LSM as part of a DA framework will improve the accuracy of snow mass estimates.

Section 4.2 provides the overall introduction of DA as well as the one-dimensional ensemble Kalman filter (EnKF) used to assimilate the C-band backscatter observations into the LSM. Section 4.3 describes the brief introduction of datasets, models, and the study area. In Section 4.4, the assessment of updated SWE and snow depth through comparison with a model-only run (i.e., without data assimilation) as well as against ground-based measurements is introduced. Afterwords, study conclusions and discussion are presented.

4.2 Datasets, Models, and Methods

4.2.1 Sentinel-1 Backscatter Observations

In a similar fashion as discussed in Chapter 2, Sentinel-1 IW GRD backscatter observations were selected as the primary application with a focus on terrestrial snow mass estimates. Moreover, Sentinel-1 backscatter observations underwent the same preprocessing steps introduced in Section 2.2.2 using Google Earth Engine to mitigate geometric distortions (e.g., foreshortening and overlying) as well as thermal

and speckle noises. Additionally, Sentinel-1 observations were resampled onto a 0.01° equidistant cylindrical grid to coincide with the spatial resolution of geophysical estimates from the Noah-MP land surface model. One main difference in this chapter is that Sentinel-1 observations for only ascending overpasses (approximately 6 p.m. local time) was utilized rather than observations from descending overpasses or a combination of ascending and descending overpasses in order to minimize random errors caused by the mixture of different electromagnetic responses from different snow conditions (e.g., dry snow versus wet snow) as summarized in Section 2.3.4.

4.2.2 Land Information System

The NASA Land Information System (LIS) is an inclusive software framework developed at the Goddard Space Flight Center. LIS contains various components including advanced land surface models (LSMs), various types of observation readers (e.g., ground and satellite observations), DA algorithms, and high-performance computing routines all with the primary objective of enhancing the knowledge of land-atmosphere interactions [118]. Among the various LSMs provided within LIS, the Noah-multiparameterization (Noah-MP; [154]) model was chosen for this study.

The basic framework of Noah-MP follows the Noah LSM while it augments multiple parameterization options to improve the representation of land-atmosphere interactions [154]. In terms of snow, Noah-MP contains a physically-based snow model with three snow layers and improved snow albedo schemes, which results in better representation of snow mass estimates as well as snowmelt timing as compared

to the Noah LSM [154,226]. Selection of the parameterizations applied in Noah-MP follows the schemes introduced in Kwon et al. [121].

Before running each simulation, initial conditions for the model were established during a spin-up period (e.g., January 1980 to May 2015) using a single replicate followed by a 20-member ensemble of model realizations computed from an additional model run from May 2015 to August 2016 based on perturbed meteorological fields from the Modern-Era Retrospective analysis for Research and Application, version 2 (MERRA-2; [82]) and Tropical Rainfall Measuring Mission (TRMM) products as boundary condition (details outlined in Section 4.2.3). With the established ensemble of initial conditions, Noah-MP was simulated using both model-only (a.k.a., Open Loop) and data assimilation techniques on a 0.01° equidistant cylindrical grid with a daily time step (aggregated up from 15-minute model run) from September 2016 to August 2017.

4.2.2.1 Ground-based Measurements and Study Area

Evaluation of snow mass estimates (i.e., SWE and snow depth) from both the model-alone simulation (a.k.a. Open Loop; OL) and the DA simulation was conducted through a comparison with SWE and snow depth measurements from the SNOwpack TELemetry (SNOTEL) network. SNOTEL is a ground-based measurement network operated by the U.S. Department of Agriculture National Resources Conservation Services (NRCS; `https://www.wcc.nrcs.usda.gov/snow/`) and provides SWE, snow depth, precipitation, and air temperature measurements.

In this study, SWE and snow depth measurements during the validation period (e.g., September 2016 to August 2017) were collected from 112 stations located within the study domain (Figure 4.1). The average elevation for the selected sites was 3071 m with the lowest elevation being 2268 m (Battle Mountain; WY317) and the highest elevation being 3542 m (Sargents Mesa; CO 1128).

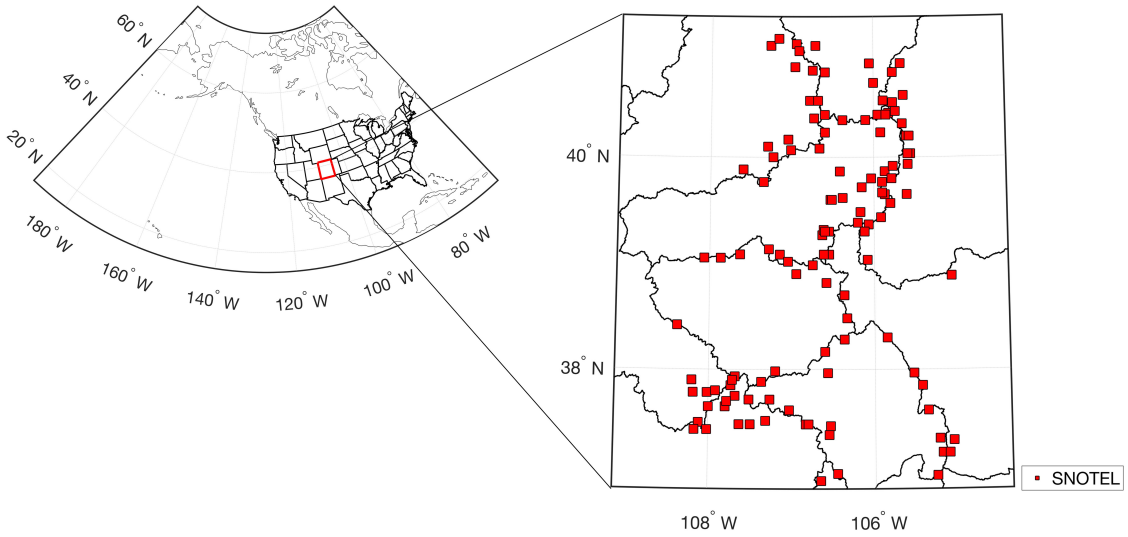

Figure 4.1: Geographic location of the study domain including the locations of SNOTEL stations. The black lines in the right-most figure represent the boundary lines of subbasins (Hydrological Unit Code level 4 scale) provided by the USGS.

4.2.3 Data Assimilation Framework

This study utilized a one-dimensional EnKF to integrate Sentinel-1 backscatter observations into the Noah-MP land surface model. One main advantage of the EnKF is that it does not require linear models or Gaussian errors, which leads to its wide application in numerous hydrologic studies including soil moisture [89, 97, 174], snow mass [51, 81, 192, 225], and streamflow [41, 57, 85].

As part of the EnKF routine, ensemble replicates are propagated in time and updates of model states are determined by the mean and spread of the ensemble replicates which approximate the state distribution. During the propagation step, the *a priori* state vector at time step t, y_t^{j-}, is calculated as a function of *a posteriori* model state vector at time step $t-1$, y_{t-1}^{j+}, forcings, $u_{j,t-1}$, and additive model error, α_j, which can be written as:

$$y_t^{j-} = f(y_{t-1}^{j+}, u_{j,t-1}, \alpha_j) \quad \text{for} \quad j \in [1, 2, \ldots N_r] \;\; with \;\; y(t = t_0) = y_0 \tag{4.1}$$

where j represents a given replicate that is propagated with the geophysical (land surface) model and N_r represents the number of the ensemble replicates. In this study, N_r=20 ensemble replicates was selected based on Kwon et al. [121]. The symbol $f(\cdot)$ indicates the nonlinear geophysical model operator (i.e., Noah-MP in this study). After the propagation step, the EnKF uses an update equation as follows:

$$y_t^{j+} = y_t^{j-} + K_t[(Z_t + \epsilon^j) - M_t(y_t^{j-})] \tag{4.2}$$

where y_t^{j-} and y_t^{j+} indicate the *a posteriori* and *a priori* model state of the jth ensemble at time step t, respectively. Z_t is the Sentinel-1 backscatter observations at measurement time t that is perturbed with measurement error, ϵ^j, following a Gaussian distribution of mean zero and observation error covariance, C_{vv}. $M_t(y_t^{j-})$ is the backscatter estimate from the observation operator, $M_t(\cdot)$, which maps the geophyiscal model space to observation space. In this study, SVM regression serves as $M_t(\cdot)$ (see section 4.2.4 for details). K_t is the Kalman gain, which is a relative weight between the observation error and model error that determines the amount

of update. K_t can be computed as:

$$K_t = Cov(y_t^{j-}, M_t(y_t^{j-}))[Cov(M_t(y_t^{j-}), M_t(y_t^{j-})) + C_{vv}]^{-1} \tag{4.3}$$

where $Cov(y_t^{j-}, M_t(y_t^{j-}))$ represents the error cross-covariance between the *a priori* model estimates and estimated backscatter derived from the observation operator. $Cov(M_t y_j^-, M_t(y_j^-))$ denotes the error (sample) covariance of the estimated backscatter derived from the observation operator and C_{vv} is the error covariance of the Sentinel-1 backscatter observations. Based on Lievens et al. [132], 0.3^2 dB^2 was selected as the error covariance of the Sentinel-1 backscatter observations.

Perturbation of model forcings is one key aspect in the OL and DA simulations that implicitly quantifies the uncertainty of the boundary conditions, and hence, the resulting snowpack based on ensemble replicates. Details of the perturbation scheme follows that introduced in Kwon et al. [121] and Reichle et al. [175]. Selected parameters for perturbation include the radiation components (i.e., downwelling shortwave and downwelling longwave radiation), near-surface air temperature, and precipitation. An overview of the perturbation parameters are summarized in Table 4.1. Throughout all four boundary conditions highlighted in Table 4.1, a first-order autoregressive model temporal correlation of 1 day was used. In the case of shortwave radiation and precipitation, these parameters were perturbed using additive, zero-mean Gaussian distributions while multiplicative, log-normal distributions with a mean of one was utilized to perturb longwave radiation and near-surface air temperature.

Table 4.1: Overall summary of perturbations of meteorological forcing datasets for both OL and DA. Note that M and A represents multiplicative and additive, respectively. AR(1) represents the first-order autoregressive temporal correlation.

Forcings	**Error Type**	**Standard Deviation**	**AR(1)**	**Cross Correlation**			
				SW	LW	P	T_a
Shortwave Radiation (SW)	M	0.5	1 day	1			
Longwave Radiation (LW)	A	50 Wm^{-2}	1 day	-0.5	1		
Rainfall Rate (P)	M	0.5	1 day	-0.8	0.5	1	
Near-Surface Air Temperature (T_a)	A	1 K	1 day	0.3	0.6	-0.1	1

4.2.4 Support Vector Machine Observation Operator

The main role of the observation operator, $M_t(\cdot)$, within the DA framework is to map the model states (e.g., SWE estimated from Noah-MP) into observation (i.e., backscatter) space. Existing studies [2, 75, 77, 121] demonstrate the ability of machine learning (ML) algorithms as an effective observation operator (alternative to a radiative transfer model, e.g.) for snow mass assimilation. More specifically, Chapter 2 revealed that the physically-constrained support vector machine (SVM) regression developed over snow-covered terrain successfully reproduced the C-band backscatter observations when considering the different electromagnetic response from different snow conditions.

Given the [1 × N] input vector (y) that represents four geophysical variables from Noah-MP (e.g., SWE, snow density, snow liquid water content, and top layer snow temperature), the general solution to SVM regression can be expressed as:

$$\begin{bmatrix} \hat{\sigma}_{VV} \\ \\ \hat{\sigma}_{VH} \end{bmatrix} = f(x) = \sum_{i=1}^{M} (\alpha_i - \alpha_i^*) k(x_i, y) + \delta \tag{4.4}$$

where $\hat{\sigma}_{VV}$ and $\hat{\sigma}_{VH}$ denotes the predicted co- and cross-polarized backscatter from

the well-trained SVM, respectively. Training matrix, x, contains the model input vectors, y, at the times of m training targets at a given pixel with a matrix size of [M $\times$ N], where M indicates the number of a available Sentinel-1 observations for SVM training [74]. α_i and α_i^* indicate the dual Lagrangian multipliers and δ represents the offset coefficients. Among the different kernel types, the Gaussian radial basis kernel function, $k(x_i, y) = \exp\{-\gamma||x_i - y||^2\}$, was selected in this study. Solution of Equation 4.4 was conducted using the LIBSVM library [35], which is an open source machine learning module provided by National Taiwan University. SVM training and prediction follows the procedure outlined in the Section 2.3.4 and is also summarized in the following section.

4.2.4.1 SVM Training and Prediction Procedure

Training targets (and outputs) include both co-polarized (σ_{VV}) and cross-polarized (σ_{VH}) Sentinel-1 backscatter observations over snow-covered terrain, which is conditionally constrained by the Interactive Multisensor Snow and Ice Mapping System (IMS) snow cover products from National Oceanic and Atmospheric Administration/National Environmental Satellite, Data, and Information Service (NOAA/NESDIS). In this section, backscatter at different polarizations were trained separately because of the different electromagnetic response in σ_{VV} and σ_{VH} depending on the snow wetness. For example, σ_{VV} does not show significant variation during the dry snow season as the long deeper penetration depth of C-band radiation leads the total backscatter to be predominantly controlled by the snow-land

interface [129]. However, an increase of liquid water content within the snowpack during wet snow conditions leads to more absorption and reflection of C-band photons, which results in the sharp decrease of σ_{VV} [131]. In the case of σ_{VH}, C-band photon scattering is more variable as it is more sensitive to multiple scatterings within the snowpack as compared to co-polarized C-band radiation [66, 228].

During the SVM training phase, Sentinel-1 observations during April 2015 to August 2016 and September 2017 to August 2018, were selected for use. In order to implement a split-sampling procedure, Sentinel-1 observations during September 2016 to August 2017 were excluded from SVM training and instead were used during the validation procedure. For training of each grid cell, a fortnightly training period was used that includes 2-week period before and after the specific fortnight of interest. This was done to better capture the snow seasonality while also reducing discontinuities between one fortnightly period and the next [75].

Besides the training target, the selection of optimal input variables plays an important role in implementing physical constraints into the statistical learning process. Following the techniques outlined in Section 2.4, four snow-related geophysical variables estimated from Noah MP (i.e., SWE, snow density, snow liquid water, and top-layer snow temperature) were selected for this study. Selection of this particular set of input datasets was predicted by the C-band scattering mechanisms over the snow-covered terrain.

4.2.4.2 SVM Controllability Issues

In general, the controllability of the system is guaranteed if and only if changing the inputs of the system can change the system output [210]. For the use of SVM regression as an observation operator in this DA framework, it is assumed that errors in the prognostic model states(s) are correlated back to the SVM-based predictions [121]. Once the appropriate type and number of input datasets and training targets are established, the SVM-based DA framework, in general, is controllable. In short, controllability issues arise when the trained SVM is required to make predictions based on inputs (scenarios) that were not witnessed during the training procedure. Unfortunately, as mentioned in Section 2.2.2, irregular data acquisition before early 2017 might influence the number of available training datasets, at times, lead to the generation of an uncontrollable SVM-based observation operator that, in turn, results in degrading the accuracy of snow mass estimates via DA.

In order to minimize this controllability issue, a rule-based DA update was utilized in this study. First, when considering the typical range of Sentinel-1 backscatter observations over snow-covered terrain (e.g., ranged from -30 dB to 0 dB in both σ_{VV} and σ_{VH}), assimilation was turned off when the predicted backscatter was outside of this specific range. Further, when the absolute deviation between predicted and observed backscatter is larger than an established threshold (e.g., 10 dB based on the previous chapter), the assimilation routine was turned off. These simple rules are intended to help mitigate issues related to a lack of SVM controllability that occurs infrequently, but has deleterious effects when it does occur.

4.2.4.3 Evaluation Metrics

For the evaluation of DA performance, snow estimates, including SWE and snow depth, from both the OL and Sentinel-1 DA were compared against the ground-based measurements. Even though only SWE was directly updated in the Sentinel-1 DA framework, it is worthwhile to evaluate snow depth as it is also directly impacted by the updated SWE assuming a constant snow density [76].

Correlation coefficient (R), bias, and root mean square error (RMSE) are selected to quantitatively examine the performance of the OL and Sentinel-1 DA and are computed as:

$$bias = \frac{1}{N_s}\sum_{j=1}^{N_s}(\langle y_{est,j}\rangle - y_{meas,j}) \tag{4.5}$$

$$RMSE = \sqrt{\frac{1}{N_s}\sum_{j=1}^{N_s}(\langle y_{est,j}\rangle - y_{meas,j})^2} \tag{4.6}$$

$$R = \frac{\sum_{j=1}^{N_s}(\langle y_{est,j}\rangle - \bar{y}_{est,j})(y_{meas,j} - \bar{y}_{meas})}{\sqrt{\sum_{j=1}^{N_s}(\langle y_{est,j}\rangle - \langle\bar{y}_{est}\rangle)^2}\sqrt{\sum_{j=1}^{N_s}(y_{meas,j} - \bar{y}_{meas})^2}} \tag{4.7}$$

where $\langle y_{est,j}\rangle$ represents the ensemble mean of SWE or snow depth estimates at time j obtained from both OL and Sentinel-1 DA. $y_{meas,j}$ denotes the ground-based SWE or snow depth at time j. $\langle\bar{y}_{est}\rangle$ is the time-averaged ensemble mean of SWE or snow depth estimates from the OL or Sentinel-1 DA. $\bar{y}_{meas}$ denotes the time-averaged SWE or snow depth from the ground-based measurements. R is a measure of the agreement in seasonal variation between the model estimates and ground-based measurements. Bias represents the systematic error while RMSE accounts for both systematic and non-systematic errors. In addition, unbiased RMSE (ubRMSE; [70])

was also included to address the non-systemic error by removing the bias from RMSE.

4.3 Results and Discussion

4.3.1 DA with and without Rule-based Updates

Performance of Sentinel-1 DA with and without rule-based updates (introduced in Section 4.2.4.2) was evaluated in order to assess the influence of the rule-based updates toward the robustness of the Sentinel-1 DA. As SWE is the only state variable which is directly updated through the assimilation, daily SWE estimates from both OL and Sentinel-1 DA (with and without rule-based update) were compared against the SNOTEL SWE measurements.

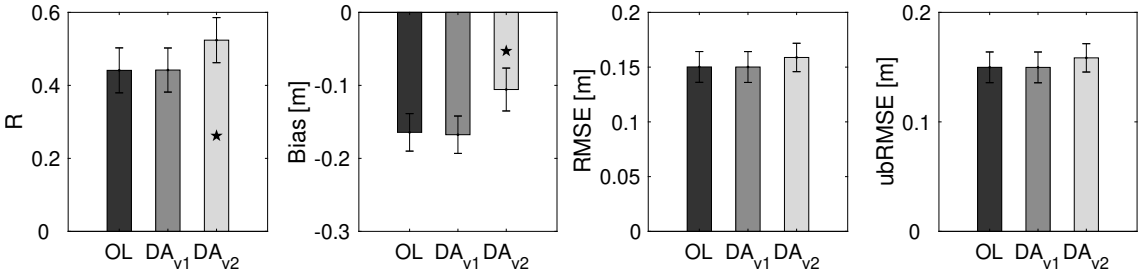

Figure 4.2: Domain-averaged goodness-of-fit statistics for SWE estimates simulated from OL and Sentinel-1 DA (with and without rule-based updates) in comparison against the SNOTEL SWE measurements. DA_{v1} does not include the rule-based updates whereas DA_{v2} does. Error bars represent the 95% confidence interval. Asterisks indicate that evaluation metrics calculated for the experiment (e.g., DA_{v1} or DA_{v2}) yielded statistically significant differences with those calculated from the Open Loop

at a 5% significance level.

Figure 4.2 summarizes the domain-averaged R, bias, RMSE, and ubRMSE calculated by comparing SWE estimates from the OL and Sentinel-1 DA simulations,

including both with and without rules-based updates (denoted as DA_{v1} and DA_{v2}, respectively) against SNOTEL SWE measurements from 112 stations within the study domain. The results confirmed that Sentinel-1 DA with the rule-based update showed significant improvement in R and bias compared to Sentinel-1 DA without the update rules as well as compared to the OL. Sentinel-1 DA without the rule-based update showed no significant difference in terms of domain-averaged bias with OL (-0.16 m) while Sentinel-1 DA with the rules-based update showed a less negative domain averaged bias of -0.11 m. Similarly, OL and Sentinel-1 DA without rule-based update did not show a significant difference in R (0.44) while Sentinel-1 DA with the rule-based update showed better agreement in terms of seasonal behavior with ground-based measurements (R=0.52).

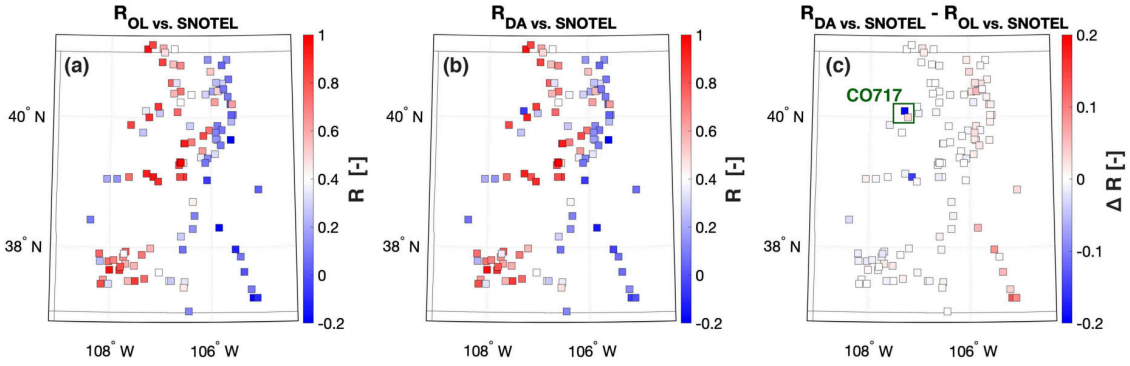

Figure 4.3: Spatial maps of correlation coefficient, R, computed between SNOTEL and (a) OL SWE and (b) Sentinel-1 DA (without rule-based update) SWE from September 2016 to August 2017. The difference in R between the OL and Sentinel-1 DA is shown in (c). The red colors (positive values) in (c) suggests that Sentinel-1 DA agrees better with SNOTEL SWE than does the OL. Oppositely, blue colors (negative values) indicate that the OL showed better agreement with SNOTEL SWE than did Sentinel-1 DA.

The spatial distribution of R for the SWE estimates from OL and Sentinel-1 DA without the rule-based update versus SNOTEL SWE measurements and dif-

ferences in skill are shown in Figure 4.3. Among the available SNOTEL stations, 56 sites out of 112 SNOTEL stations yielded better performance by OL than did Sentinel-1 DA without the rule-based update. Similar behaviors were observed from bias, RMSE, and ubRMSE in that more than 50% of available stations indicated that the OL performed better than Sentinel-1 DA without the rule-based update. However, Figure 4.3(c) illustrates that the difference between R calculated from DA without the rule-based update and OL against SNOTEL measurements showed that most of the stations indicated no significant improvement in SWE estimates between the OL and Sentinel-1 DA. Among all SNOTEL stations within the study domain, CO 717 (Ripple Creek, CO) showed the largest decrease in R (Figure 4.3(c)) and a relatively large degradation in bias (from -0.06 m to -0.31 m) as well as RMSE (from 0.40 m to 0.49 m). Accordingly, the time series of SWE simulated from OL and Sentinel-1 DA (without and with rule-based updates) against ground-based SWE measurements are shown in Figure 4.4 for the detailed analysis.

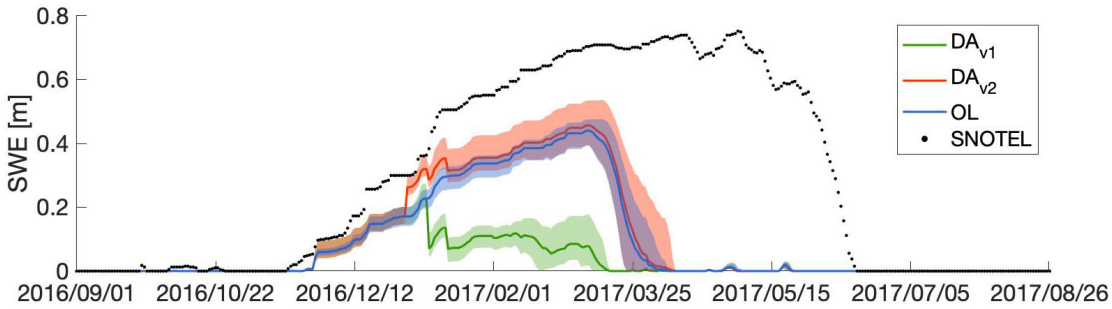

Figure 4.4: Time series of SWE estimated from OL (blue) and Sentinel-1 DA with (red) and without (green) rule-based updates along with SNOTEL measurements (black dots) at Ripple Creek station (CO 717; 40.1°N 107.3°W). Solid lines represent the ensemble mean of SWE and corresponding shadow region represents the ensemble spread of the SWE estimates.

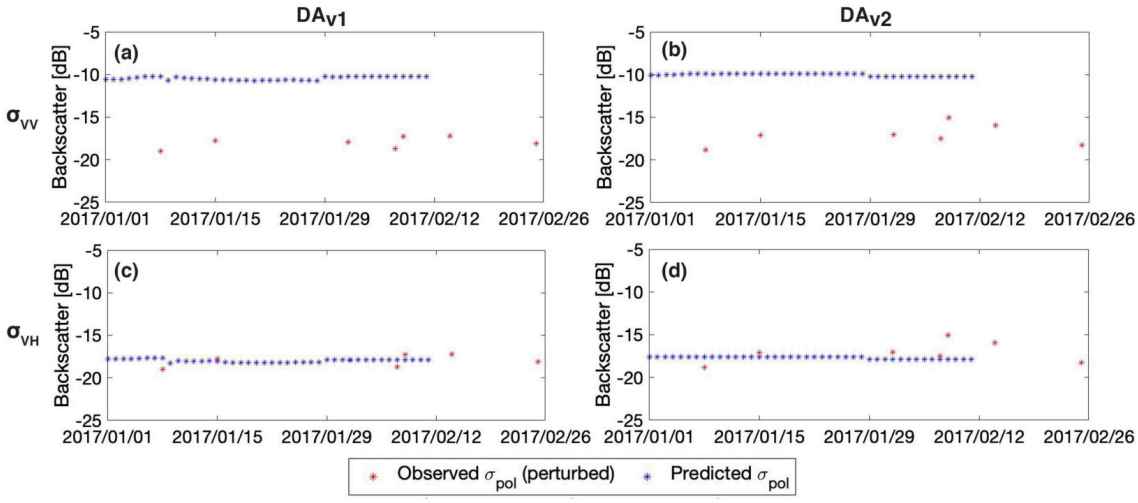

Figure 4.5: Time series of observed and predicted co-polarized (σ_{VV}) and cross-polarized (σ_{VH}) backscatter at Ripple Creek station during 1 January 2017 to 28 February 2017. The left and right column represents the Sentinel-1 DA without (a.k.a., $\mathrm{DA_{V1}}$) and with the rule-based update (a.k.a., $\mathrm{DA_{V2}}$), respectively.

Results revealed that both OL and Sentinel-1 DA (with and without rule-based updates) showed a similar trend before 5 January 2017. However, Sentinel-1 DA with and without rule-based updates showed significantly different behavior after 5 January 2017 in that Sentinel-1 DA without the rule-based update showed a significant decrease in SWE while Sentinel-1 DA with rule-based update showed an increasing trend of SWE (Figure 4.4). The main reason for this phenomenon is the influence of the rule-based update into Sentinel-1 DA. Figure 4.5 illustrates the time series of observed Sentinel-1 backscatter and predicted backscatter via the observation operator at both co-polarized (σ_{VV}) and cross-polarized (σ_{VH}) backscatter from January to February 2017. It reveals that the predicted σ_{VH} showed reasonable agreement between predicted and observed backscatter while σ_{VV} showed a large discrepancy. Given the limited number of training datasets as well as a lack of Sentinel-1 obser-

vations, SVM regression tends to predict a heavily biased predicted backscatter at this location. For example, predicted σ_{VV} represented in Figure 4.5(a) produced higher magnitude of backscatter than the observed σ_{VV}. This behavior results in decreasing the SWE estimates (Figure 4.4). In the case of DA with the rule-based update, because the assimilation switch for σ_{VV} is turned off and only σ_{VH} is used in calculating the Kalman gain, the updated SWE has a slightly better agreement with the SNOTEL SWE measurements relative to the OL. Moreover, another advantage of applying the rule-based update is to further influence the accuracy of predicted backscatter. As the SVM utilizes the updated (*a posterior)* geophysical variables to predict the σ_{VV} and σ_{VH}, it results in improving the accuracy of the predicted backscatter in the following days. For example, Sentinel-1 DA without rule-based update showed a slight increase in predicted σ_{VV} on 29 January 2017 while Sentinel-1 DA with rule-based update showed a slight decrease in predicted σ_{VV}, which better agrees with the magnitude of observed σ_{VV} (Figure 4.5(a) and (b)).

4.3.2 Evaluation of SWE against Ground-based Measurements

The primary focus of this section is the evaluation of Sentinel-1 DA with the rule-based update (hereafter denoted as Sentinel-1 DA_{v2}) through comparison against the SNOTEL SWE measurements from September 2016 to August 2017. Domain-averaged statistics presented in Figure 4.2 indicated that Sentinel-1 DA_{v2} yielded the significant improvement in R and bias while the magnitude of RMSE and

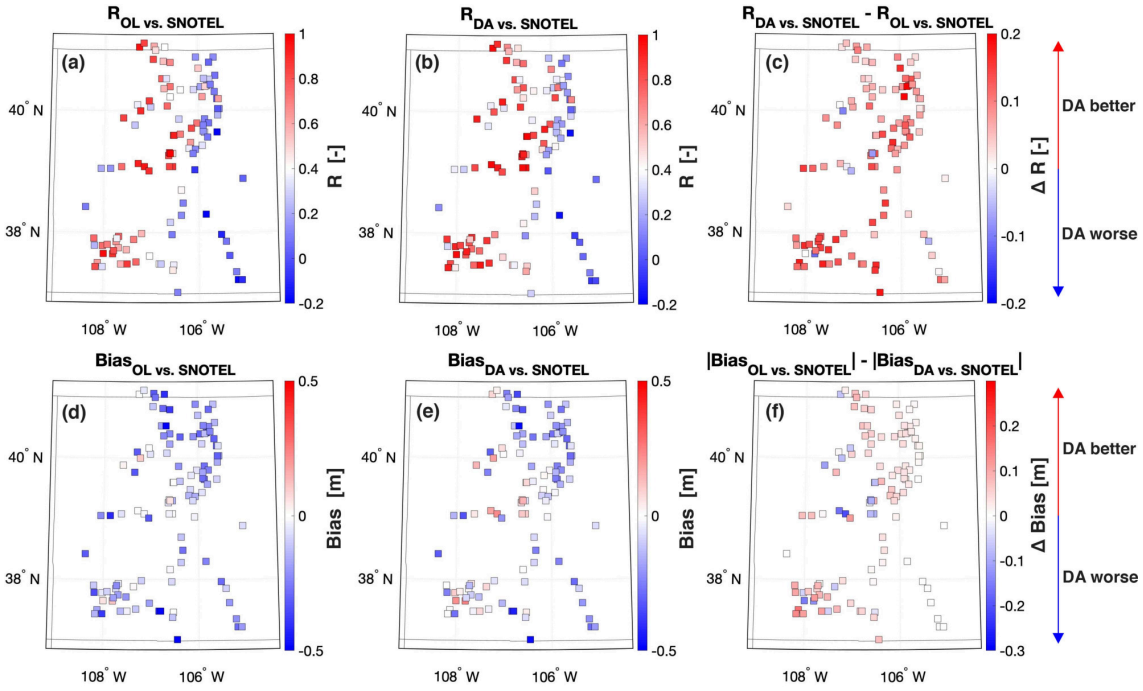

Figure 4.6: Spatial maps of correlation coefficient, R, (top row) and bias (bottom row) computed against the SNOTEL SWE measurement from September 2016 to August 2017. Left and middle columns represent the statistics of OL SWE and Sentinel-1 DA_{v2} (with rule-based update) SWE, respectively. The differences in R and bias are shown in (c) and (f), respectively. The red colors (positive values) in (c) suggests that Sentinel-1 DA_{v2} agrees better with SNOTEL SWE than does the OL. Oppositely, blue colors (negative values) indicate that the OL showed better agreement with SNOTEL SWE than did Sentinel-1 DA_{v2}.

ubRMSE were slightly increased. Figure 4.6 illustrates the temporal mean of R and bias as well as improvements in statistical metrics at the SNOTEL stations when using Sentinel-1 DA_{v2}. In the case of OL, R ranged from -0.21 to 0.99 while R for Sentinel-1 DA_{v2} ranges from -0.18 to 0.99. Among all available SNOTEL stations, more than 90% yielded a statistical improvement, indicating that Sentinel-1 DA_{v2} resulted in better agreement in terms of seasonal variation with the SNOTEL SWE measurements relative to the OL simulation. Similar behavior was observed for bias in that Sentinel-1 DA_{v2} showed a smaller magnitude in bias than the OL (Figure

4.6(f)). The bias in SWE estimated from the OL ranged from -0.55 m to 0.11 m while the bias of SWE simulated from Sentinel-1 DA_{v2} ranges between -0.49 m to 0.24 m. In general, SWE estimates from Sentinel-1 DA_{v2} showed less bias than the OL at 84 SNOTEL stations (out of a total of 112) located within the study domain.

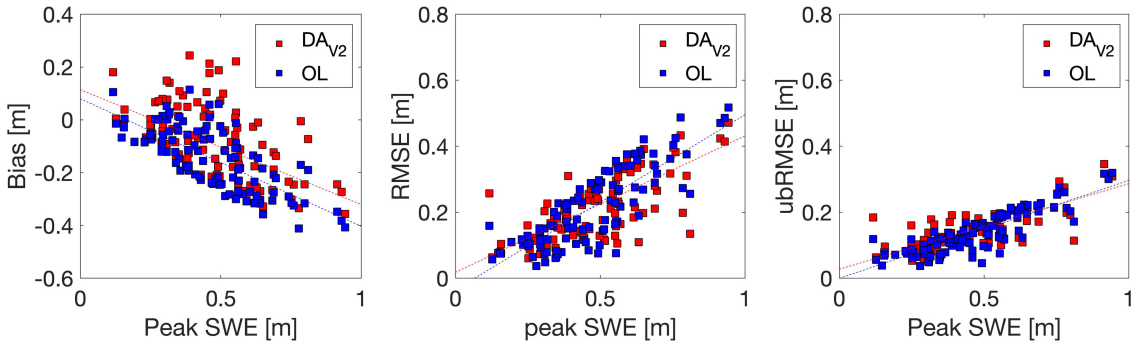

Figure 4.7: Scatter plots of the bias, RMSE, and ubRMSE in accordance with the peak of SWE observed from SNOTEL stations. Note that blue and red dot represents the Open Loop (e.g., model-only simulation) and Sentinel-1 DA_{V2}, respectively.

According to Figure 4.6(d) and (e), most of the bias was negative across the study domain. One of the main reasons for the discrepancy between simulated and measured SWE can be explained through the spatial scale mismatch. Ground-based measurements have a spatial footprint of $\sim$1 m^2 while SWE estimates from both the OL and Sentinel-1 DA_{v2} have a spatial footprint of $\sim 10^6$ m^2. Furthermore, the bias in SWE estimates from both the OL and Sentinel-1 DA_{v2} is increasingly negative with an increase in the amount of peak SWE (Figure 4.7(a)). One possible explanation for this phenomenon is related to the difficulty in representing the complex snow stratigraphy as snow becomes deeper. The increase in SWE uncertainty with higher peak SWE can be also explained by errors in the snow albedo. Snow albedo is a first-order control in the partitioning of available energy at the surface, and in

turn, influences the amount of snowmelt [11]. Kumar et al. [117] assimilated the Moderate Resolution Imaging Spectroradiometer (MODIS) albedo retrievals in the Noah-MP land surface model over the continental U.S. The results confirmed that model-only run tends to significantly underestimate snow albedo during the winter period (e.g., November to March). Underestimation of the snow albedo results in an increase of the net radiation and snowmelt, and in turn, reduces the peak snow accumulation. Furthermore, Bosilovich et al. [21] revealed that MERRA2 precipitation showed relatively large uncertainties over the Rockies due to the orographic effect related to the complex topography. Uncertainties in precipitation significantly influences to the accuracy of MERRA-2 snowfall data. Liu and Margulis [134] addressed that raw MERRA2 snowfall product showed significant underestimation when compared against the ensemble-based snowfall reanalysis datasets implemented with the uncertainty of precipitation.

Focusing on the evaluation of the OL and Sentinel-1 DA_{v2} performance, integration of C-band backscatter observations with machine learning as the observation operator helped to slightly reduce the magnitude of bias with the trend line slightly approaching to the slope of zero (Figure 4.7(a)). RMSE and ubRMSE represented in Figure 4.7(b) and (c) also showed that Sentinel-1 DA_{v2} showed slight improvement as the trend line of Sentinel-1 DA_{v2} is less than for the OL simulation. However, the bias in Sentinel-1 DA_{v2} showed more spread in terms of bias, RMSE, and ubRMSE at relatively low peak SWE values.

Domain-averaged statistics of SWE estimates from both the OL and Sentinel-1 DA_{v2} during the snow accumulation (e.g., December, January, and February) and

Table 4.2: Domain-averaged statistics of SWE estimated from the OL and Sentinel-1 DA_{v2} relative to SNOTEL SWE measurements. Note that statistics with an asterisk denote statistically significant differences between the SWE estimates from the OL and Sentinel-1 DA_{v2} at a 5% level of significance.

Period		**R [-]**	**Bias [m]**	**RMSE [m]**	**ubRMSE [m]**
Snow	OL	0.75	-0.10	0.14	0.07
Accumulation	DA_{v2}	0.81	-0.03*	0.14	0.07
Snow	OL	0.32	-0.29	0.33	0.11
Ablation	DA_{v2}	0.40	-0.22*	0.31	0.13*

snow ablation (e.g., March, April, and May) are summarized in Table 4.2. Overall, statistics during the snow accumulation period showed better performance than during the snow ablation period. Domain-averaged bias was significantly reduced from -0.10 m (OL) to -0.03 m (Sentinel-1 DA_{v2}) and R also revealed slight improvement from 0.75 (OL) to 0.81 (Sentinel-1 DA_{v2}) yet did not achieve statistical significance at the 5% significance level. Even though domain-averaged bias showed significant improvement in Sentinel-1 DA_{v2}, the RMSE and ubRMSE yielded no significant skill difference between the OL and Sentinel-1 DA_{v2}. This phenomenon is also revealed in Figure 4.7(a) in that the bias in Sentinel-1 DA_{v2} showed a relatively wider spread relative to the OL when the peak SWE is less than 0.4 m.

In the case of the snow ablation period, the magnitude of statistical metrics was lower than that for the snow accumulation period. More specifically, the ranges of R were within the range of -0.17 to 0.93 for OL and -0.17 to 0.96 for Sentinel-1 DA_{v2}. In the case of the bias, the OL yielded a bias range from -0.95 m to 0.15 m while the bias of Sentinel-1 DA_{v2} ranged from -0.62 m to 0.20 m. RMSE does not

reveal any significant differences between the OL and Sentinel-1 DA_{v2}; ubRMSE showed a slight increase from 0.11 (OL) to 0.13 (Sentinel-1 DA_{v2}) with a statistical significance of 5%.

4.3.3 Evaluation of Snow Depth against Ground-based Measurements

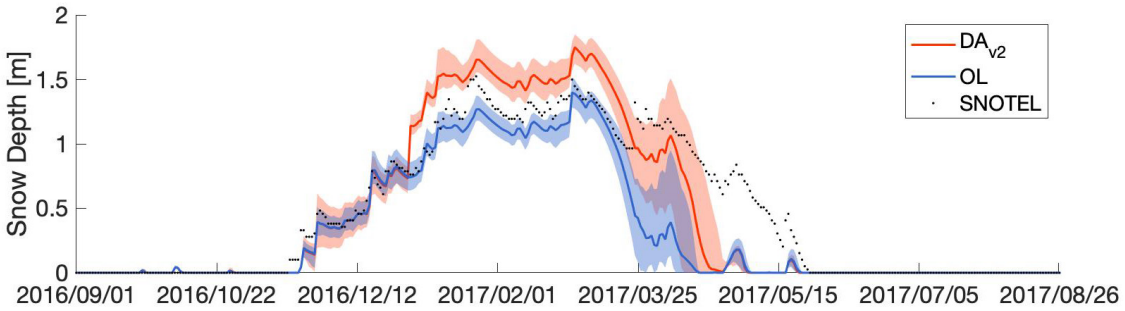

Figure 4.8: Time series of the estimated snow depth from OL and Sentinel-1 DA as well as SNOTEL snow depth measurement at Mineral Creek (CO 629; 40.23°N 106.6°W) during September 2016 to August 2017. Note that solid line represents the ensemble mean of the snow depth estimates while shading of corresponding color represents the ensemble spread of snow depth estimates.

Figure 4.8 represents the time series of snow depth at Mineral Creek (CO 629; 40.23°N 106.6°W) from September 2016 to August 2017. The reason for selecting this site is fairly typical seasonal variation of snow among the 112 SNOTEL stations. These results confirmed that both the OL and Sentinel-1 DA_{v2} showed good agreement in capturing seasonal patterns with the ground-based snow depth measurements. Among the various statistical metrics, bias showed the most improvement from -0.24 m (OL) to -0.03 m (Sentinel-1 DA_{v2}). Sentinel-1 DA_{v2} showed slightly better performance in capturing the seasonal variation of SNOTEL snow depth measurement with a slightly higher magnitude of R (0.90) than the OL (0.81).

Similarly, RMSE and ubRMSE of DA (0.30 m and 0.29 m, respectively) showed improvement compared to the RMSE and ubRMSE of the OL (0.38 m and 0.31 m, respectively). In addition, Sentinel-1 DA_{v2} showed advantages over the OL from late-March (Figure 4.8). That is, the OL showed a significant, rapid snowmelt exist immediately after the peak in early-March and then the snow disappeared by 15 Apr 2017. However, snow depth estimates from Sentinel-1 DA_{v2} were similar to the SNOTEL measurements in late-March and yielded a slightly longer snow season compared to the OL. According to the global forest cover datasets [91], this site showed a high forest cover fraction of around 0.7. Chen et al. [37, 38] mentioned that high vegetation cover fraction often results in shortening the snow period in Noah-MP snow mass estimates as an increase of canopy during spring leads to the increase of longwave radiation from the sub-canopy that often results in early snow disappearance. With the assimilation of Sentinel-1 observations during the snow ablation period that contains relatively deeper and wetter snow, Sentinel-1 DA_{v2} resulted in the improvement in the updated snow depth.

The spatial distribution of R for the snow depth estimates from the OL and Sentinel-1 DA_{v2} compared to SNOTEL snow depth measurements revealed that over 50% of the SNOTEL stations (e.g., 54% for OL and 66% for Sentinel-1 DA) showed R larger than 0.6. R for the OL and Sentinel-1 DA_{v2} ranged from -0.05 to 0.98 and -0.03 to 0.98, respectively. In terms of the difference of R from OL versus SNOTEL measurements and Sentinel-1 DA_{v2} versus SNOTEL measurements illustrated in Figure 4.9(c), 101 out of 112 SNOTEL stations showed improvement as a result of Sentinel-1 DA_{v2}. In terms of bias, snow depth showed a similar pattern

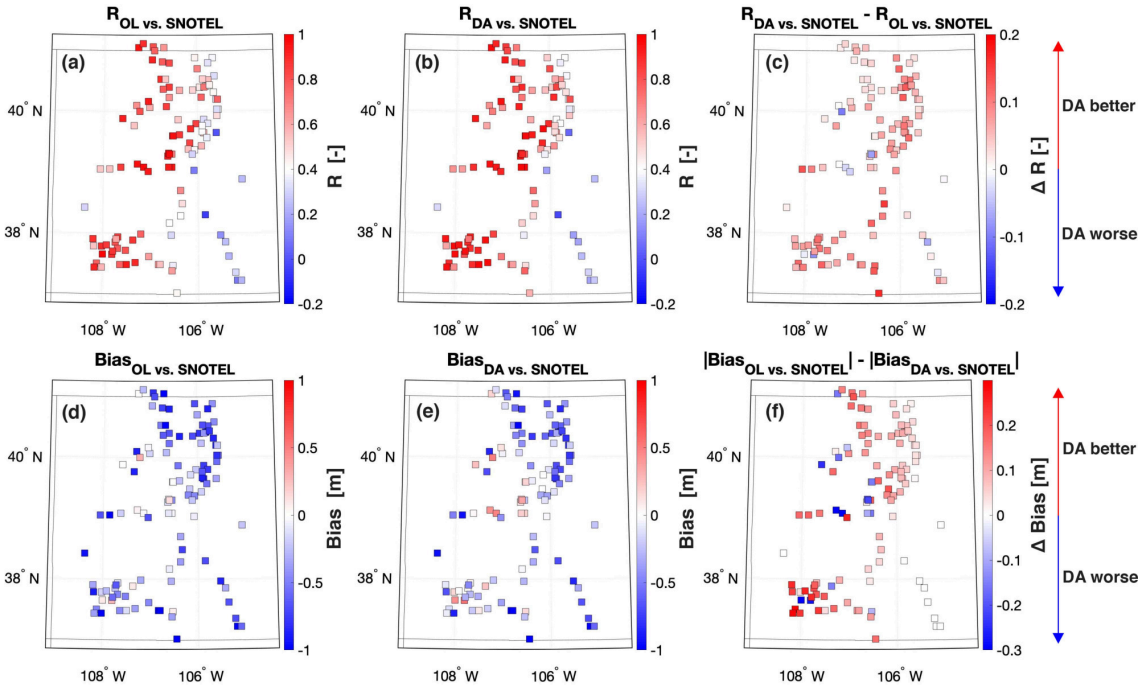

Figure 4.9: Spatial maps of correlation coefficient, R, (top row) and bias (bottom row) computed against the SNOTEL snow depth measurement from September 2016 to August 2017. Left and middle columns represent the statistics of the OL and Sentinel-1 DA_{v2} (with rule-based update), respectively. The differences in R and bias are shown in (c) and (f), respectively. The red colors (positive value) in (c) suggests that Sentinel-1 DA_{v2} agrees better with the SNOTEL snow depth than does the OL. Oppositely, blue color (negative values) indicate that the OL showed better agreement with SNOTEL snow depth than does Sentinel-1 DA_{v2}.

with SWE in that negative bias was dominant across the study domain. The bias of the OL ranged from -1.41 m to 0.31 m while the bias of Sentinel-1 DA_{v2} ranged between -1.29 m to 0.56 m. Differences in the magnitude of the bias between the OL and Sentinel-1 DA_{v2} showed that approximately 80% of the stations showed improvement in snow depth when estimated with Sentinel-1 DA_{v2} (Figure 4.9(f)).

Table 4.3 summarizes the domain-averaged R, bias, RMSE, and ubRMSE of the snow depth estimates from the OL and Sentinel-1 DA_{v2} during the snow accumulation and snow ablation periods. Most of the statistics indicate improvement

Table 4.3: Domain-averaged statistics of snow depth estimated from the OL and Sentinel-1 DA_{v2} relative to SNOTEL snow depth measurements. Note that statistics with an asterisk denote statistically significant differences between the OL and Sentinel-1 DA_{v2} at a 5% level of significance.

Period		**R [-]**	**Bias [m]**	**RMSE [m]**	**ubRMSE [m]**
Snow	OL	0.73	-0.42	0.53	0.22
Accumulation	DA_{v2}	0.79	-0.24*	0.46	0.20
Snow	OL	0.58	-0.72	0.81	0.27
Ablation	DA_{v2}	0.65*	-0.57*	0.75	0.29

via Sentinel-1 DA_{v2} during both the snow accumulation and ablation periods. More specifically, the bias of Sentinel-1 DA_{v2} during the snow accumulation and snow ablation periods showed a significant improvement at a 5% significance level. The bias during the snow accumulation period ranged from -1.18 m to 0.28 m for the OL whereas Sentinel-1 DA_{v2} yielded bias ranging from -0.93 m to 0.45 m. Similar behavior was observed for RMSE and R with a slight improvement in Sentinel-1 DA_{v2} compared with the OL. Overall improvement in Sentinel-1 DA_{v2} with regards to snow depth is similarly related to the overall improvement in SWE.

4.4 Conclusions and Future Work

The main goal of this chapter is to improve snow mass estimates (i.e., SWE and snow depth) by assimilating C-band backscatter observations into an advanced land surface model using support vector machine regression and a one-dimensional ensemble Kalman filter. The DA experiment was conducted across the snow-covered terrain of Western Colorado for September 2016 to August 2017. The SWE and snow

depth estimates in the Open Loop (i.e., without assimilation) and DA simulation were compared against measured SWE and snow depth at 112 SNOTEL stations.

Before evaluating the performance of Sentinel-1 DA, the influence of applying a rule-based update, which prescribes the expected range of backscatter over the snow-covered terrain, was evaluated by comparing SWE estimates from DA with and without the rule-based update against the SNOTEL SWE measurements. In general, more than 50% of the SNOTEL stations yielded a slight improvement in R and bias; however, many of these improvements were small values close to zero. When constraints on the range of predicted backscatter, $\hat{\sigma}^0_{VV}$ and $\hat{\sigma}^0_{VH}$ were introduced using a rule-based update, the improvements were much more significant. The rule-based update helped mitigate some of the SVM controllability issues related to a limited number of available training datasets. Furthermore, the application of rule-based update also improved the accuracy of SVM-based predicted backscatter during the SWE update, and in turn, improved the overall accuracy of SWE estimates.

A detailed assessment of SWE estimates from Sentinel-1 $\mathrm{DA_{v2}}$ (a.k.a. DA with the rule-based update) showed the capability of Sentinel-1 $\mathrm{DA_{v2}}$ to improve the accuracy of SWE estimates relative to the OL run. Detailed analysis of bias, RMSE, and ubRMSE for the SWE estimates from Sentinel-1 $\mathrm{DA_{v2}}$ also revealed the most improvements in the accuracy of the SWE estimates. More specifically, more than 75% of the SNOTEL stations showed improvement in bias and R. Statistical analysis of the SWE estimates from Sentinel-1 $\mathrm{DA_{v2}}$ during both the snow accumulation and snow ablation periods revealed the improvements, in general, when compared against the OL. More specifically, the bias showed statistically significant improvements

during both the snow accumulation (e.g. -0.10 m for OL to -0.03 m for Sentinel-1 DA_{v2}) and snow ablation periods (e.g. -0.29 m for OL to -0.22 m for Sentinel-1 DA_{v2}). In the case of RMSE and ubRMSE, there was no statistically significant difference between the OL and Sentinel-1 DA_{v2} while ubRMSE was slightly degraded in Sentinel-1 DA_{v2}. In addition, bias, RMSE, and ubRMSE from Sentinel-1 DA_{v2} showed more statistical spread when the peak SWE calculated from SNOTEL SWE measurements was relatively small, which is partly related to the relatively small sensitivity of C-band backscatter in dry, shallow snow.

Updated snow depth estimates via Sentinel-1 DA_{v2} also showed improvement compared to the OL. Specifically, more than 54% of the SNOTEL stations showed improvement in both R and bias. Seasonal variations in the snow depth estimates from the OL and Sentinel-1 DA_{v2} showed reasonable agreement with the SNOTEL measurements. More specifically, Sentinel-1 DA_{v2} showed advantages during the snow ablation period in that both magnitude and seasonal variation of snow depth matched closer to that of the SNOTEL measurements than the OL. Furthermore, Sentinel-1 DA_{v2} slightly extended the snow season relative to the OL. The statistical behavior of snow depth estimates during the snow accumulation and snow ablation period also yielded an improvement in accuracy when using the Sentinel-1 DA_{v2}. The snow ablation period showed a more significant improvement in R and bias at 5% level of significance. Overall, improvement in snow depth estimates from Sentinel-1 DA_{v2} is highly related to the improvement in SWE estimates as snow depth is recalculated based on the updated SWE assuming constant snow density before and after the update. Moreover, integration of Sentinel-1 backscatter observations

helped improve the accuracy of snow mass estimates. At the same time, however, random errors were added via Sentinel-1 DA_{v2} due to the complex electromagnetic responses of C-band backscatter in snow, the presence of noise in the backscatter observations, and limitations in the efficacy of the SVM-based observation operator.

In summary, this study helped demonstrate the capability support vector machine (SVM) regression as an observation operator within a C-band backscatter observation assimilation framework in order to improve the characterization of terrestrial snow mass. Furthermore, the rule-based update implemented during DA helped mitigate some of the controllability issues of SVM regression when trained by sparse training datasets. This research further motivates the application of physically-constrained SVM regression that considers the first-order physics of the electromagnetic response of terrestrial snow.

Chapter 5: Conclusions and Future Research

5.1 Conclusions

This dissertation focused on the evaluation of two different types of observation operators: 1) a radiative transfer model (RTM), and 2) a machine learning algorithm for the improvement of soil moisture and terrestrial snow mass estimates, respectively. Furthermore, a machine learning-based observation operator was utilized in the Sentinel-1 data assimilation framework in order to improve the terrestrial snow mass estimates across regional scales. The overall scientific question explored in this study is:"Can a radiative transfer model and a machine learning techniques serve as effective observation operators in the assimilation of microwave observations into a land surface model to better characterize soil moisture and terrestrial snow mass?"

In Chapter 2, a physically-constrained support vector machine (SVM) was designed to predict C-band backscatter observations over snow-covered terrain in Western Colorado. More specifically, different types of training targets, training window lengths, and delineation of snow with respect to the liquid water content were considered in conjunction with the first-order electromagnetic response of snow. Evaluation of predicted backscatter yielded reasonable accuracy when compared

against the Sentinel-1 observations. More specifically, a combination of ascending overpasses with descending overpasses yielded a significant increase in spatial coverage and the lowest magnitude of bias, but introduced more random errors due to the mixture of signals from different snow conditions. Similarly, elongation of the training window length resulted in acquiring more spatial coverage and improvement in bias while RMSE and ubRMSE were slightly increased. Lastly, separate training of dry snow versus wet snow revealed the improvement in statistical performance when compared with predicted backscatter without the dry snow versus wet snow delineation.

In Chapter 3, L-band brightness temperatures (T_b) are estimated from a zero-order tau-omega RTM calibrated with multi-angular SMOS T_b observations across North America. RTM-derived T_b was compared against Aquarius T_b observations colocated in space and time as a function of soil hydraulic parameters and vegetation types. The overall comparison showed that RTM-derived T_b showed good performance during both ascending and descending overpasses excluding the presence of sub-grid scale lakes and densely-forested regions. RTM-derived T_b showed good performance over relatively low porosity soils and low wilting point soils while uncertainty was increased along with the increase of porosity and wilting point. In terms of vegetation types, broadleaf and needleleaf forest showed reasonable statistical performance while grassland vegetation showed the highest uncertainty due to a lack of irrigation schemes and inter-annual crop rotation with the land surface model.

In Chapter 4, the SVM regression based explored in the Chapter 2 was uti-

lized as observation operator along with a one-dimensional ensemble Kalman filter in order to integrate C-band backscatter observations into an advanced land surface model with the goal of improving terrestrial snow mass estimates. DA experiments were conducted from September 2016 to August 2017 over snow-covered terrain across Western Colorado and evaluated through comparison against SNOTEL measurements. Before conducting the evaluation of updated SWE and snow depth, the influence of applying a rule-based updates, which prescribes an expected range of observed backscatter over snow-covered terrain, on DA performance was also examined. DA with the rule-based update yielded significantly better statistics than the traditional DA approach without the rules as well as the OL when compared against SNOTEL measurements. More notably, the rule-based update exhibited more robustness in overcoming SVM controllability issues and influencing the accuracy of SVM-based predicted backscatter. Assessments of SWE and snow depth estimates from Sentinel-1 DA showed significant improvement in terms of R and bias when compared against measured SWE and snow depth from SNOTEL stations. Sentinel-1 DA highlighted advantages during the snow ablation period in that the snow season was slightly extended and the magnitude of SWE and snow depth showed better agreement with SNOTEL measurements.

Overall results lead to the conclusion that RTM and machine-learning based algorithms can serve as effective observation operators in future DA studies by successfully reproducing L-band brightness temperature and C-band backscatter over snow-covered terrain, respectively. Furthermore, the well-trained support vector machine regression algorithm demonstrated skill within the Sentinel-1 DA framework,

which leads to a better characterization of terrestrial snow mass estimates.

5.2 Main Contributions and Novelty of Research

This dissertation includes the first attempt to utilize SVM regression over snow-covered terrain for the purpose of predicting C-band backscatter as presented in Chapter 2. More specifically, physically-constrained approach based on the first-order physics of scattering mechanisms over the snow-covered terrain yielded moderate accuracy in terms of statistical comparison. Key findings can be summarized as follows:

- Among the different training target sets, C-band backscatter observations from the descending overpass are preferred for use in snow mass data assimilation framework.

- Examination of different training window suggests that a monthly training window best balances the spatial coverage with prediction accuracy.

- SVM training using wet snow versus dry snow delineation is strongly recommended as the approach implicitly considers the different first-order scattering mechanisms over snow-covered terrain.

Chapter 3 showed that a RTM-derived L-band T_b yielded reasonable accuracy in comparison with the Aquarius L-band T_b observations across North America. Overall results encourage the use of the L-band RTM as an observation operator in a future soil moisture DA framework. Major findings and contribution to the

scientific community can be summarized as follows:

- Multi-angular SMOS T_b observations serve as an effective calibration dataset to obtain accurate L-band T_b estimates from the RTM.
- Uncertainties of RTM-derived T_b estimates with respect to soil hydraulic parameters and vegetation cover types can help better characterize error covariances to be used in a further soil moisture DA framework.

Chapter 4 is new and novel in that C-band backscatter was integrated into the Noah-MP land surface model using SVM regression and an ensemble Kalman filter with the objective of improving terrestrial snow mass estimates. Key findings from Chapter 4 are summarized as follows:

- Integration of C-band backscatter over snow-covered terrain yielded systematic improvements in SWE and snow depth estimates when compared against the model-only simulation.
- DA showed larger improvements of snow mass estimates during the snow ablation period rather than the snow accumulation period due to the increased sensitivity of C-band radiation in a wet (ripe) snowpack.

5.3 Future Research Plans

5.3.1 Aquarius Brightness Temperature Assimilation

Evaluation of the RTM-derived T_b showed the ability to serve as an observation operator within a soil moisture data assimilation framework. Key findings in

Chapter 3 can be further implemented into a future soil moisture DA framework. For example, the calibration scheme using SMOS observations should be modified by relaxing the constraints regarding the distance to open water bodies in order to improve the accuracy of RTM-derived T_b near open water bodies. In addition, a spatially-variant observation error can be more accurately prescribed. For example, regions with relatively high porosity soils and high wilting point soils as well as grassland land cover types should have a relatively large magnitude of observation error as compared to other regions.

5.3.2 Robustness Experiments of SVM Framework

Although physically-constrained support vector regression showed reasonable performance in predicting backscatter over the snow-covered terrain, several components can still result in the overall improvement of SVM performance. First, an extension of the training period can result in obtaining more Sentinel-1 observations, and in turn, better yield unbiased predicted backscatter via support vector machine regression. Furthermore, consideration of including more geophysical variables from LSM as input datasets for SVM should be explored. For example, the scattering mechanism during the dry snow conditions showed that backscatter from the snow-land interface becomes the dominant scattering component. Thus, including a dynamic estimates of root mean square height (defined as a standard deviation of surface elevation variation) or a dynamic estimates of soil roughness could help to improve the predicted backscatter during the snow accumulation period. Further-

more, as backscatter is significantly influenced by the vegetation cover, normalized difference vegetation index (NDVI) and enhanced vegetation index (EVI) can be another consideration accounting for the accumulation of biomass as an input dataset for SVM training. Lastly, better characterization of dry snow versus wet snow conditions should be considered. The current analysis utilized the snow liquid water content from Noah-MP as a proxy to classify dry versus wet snow conditions while it also contains uncertainty. Thus, a combination of snow wetness information from LSM as well as passive and active microwave imagery should be included in future work.

5.3.3 Examination of Physically-constrained Machine Learning in Snow Mass DA

In Chapter 4, the examination of SVM trained ascending-only training target sets with a fortnightly training window utilized in the DA framework resulted in the improvement of terrestrial snow mass estimates. Based on these results, Sentinel-1 DA could be extended to using different training target sets (e.g., descending-only observations and combination of ascending and descending overpasses) and different training windows (e.g., monthly and seasonal training periods) and then assess the influence on the accuracy of updated snow mass estimates. Furthermore, significant improvements of predicted backscatter along with the delineation of dry versus wet snow pixels described in Chapter 2 can be also implemented into the Sentinel-1 DA framework. As the first-order physics of different scattering mechanisms with

regards to different snow wetness conditions should be considered in the Sentinel-1 DA framework, it is expected to improve the overall accuracy of daily snow mass estimates during both the snow accumulation and snow ablation periods.

5.3.4 Extension of Sentinel-1 DA to Hydro-meteorological Fluxes

Along with the improvement of terrestrial snow mass estimates with the Sentinel-1 DA framework, it can be further hypothesized that the improvement in SWE magnitude as well as the elongation of the snow period would result in improvements in other hydrological variables. More specifically, it is hypothesized that updated snow mass estimates could also improve the accuracy of streamflow estimates from the LSM based on the improved snow melt information from DA. Furthermore, a combination of streamflow routing model (e.g., Hydrological Modeling and Analysis Platform (HyMAP; Getirana et al. [83, 84]) along with Sentinel-1 DA updates during the snow melt period would likely be reflected in changes to the surface runoff. Evaluation of runoff at daily and monthly timescales could be conducted through comparison with ground-based streamflow observations provided by USGS and the Global Runoff Data Centre (GRDC).

Appendix A: L-band Radiative Transfer Model

The L-band RTM utilized in Chapter 3 requires 32 different parameters in order to estimate the L-band brightness temperature (T_b). For this study, an incidence angle of 42.5°was utilized, which corresponds to the incidence angle of the SMOS level 1C product. Table A.1 summarizes the initially assigned values for the key RTM parameters utilized for parameterizing the soil roughness (e.g., roughness parameter [h], angular dependence [$\mathrm{N_{r_p}}$], and scattering albedo [ω]) and vegetation conditions (e.g., leaf equivalent water thickness [LEWT] and vegetation structure parameter [$\mathrm{b_p}$]). Note that all the variables excluding the LEWT and $\mathrm{N_{r_p}}$ were calibrated using multi-angular SMOS observations based on the particle swarm optimization search algorithm introduced in Kennedy and Eberhart [107].

For the soil-texture dependent parameters such as fraction of the different types of soils (e.g., sand, clay, and silt) as well as the soil hydraulic parameters (e.g., porosity and wilting point) were not selected for calibration in order to assure the consistency with the soil moisture and soil temperature as estimated from the Catchment land surface model [53]. Figure A.1 shows the spatial pattern of sand, clay, and silt fractions across the study domain based on the soil classification scheme introduced in De Lannoy et al. [50].

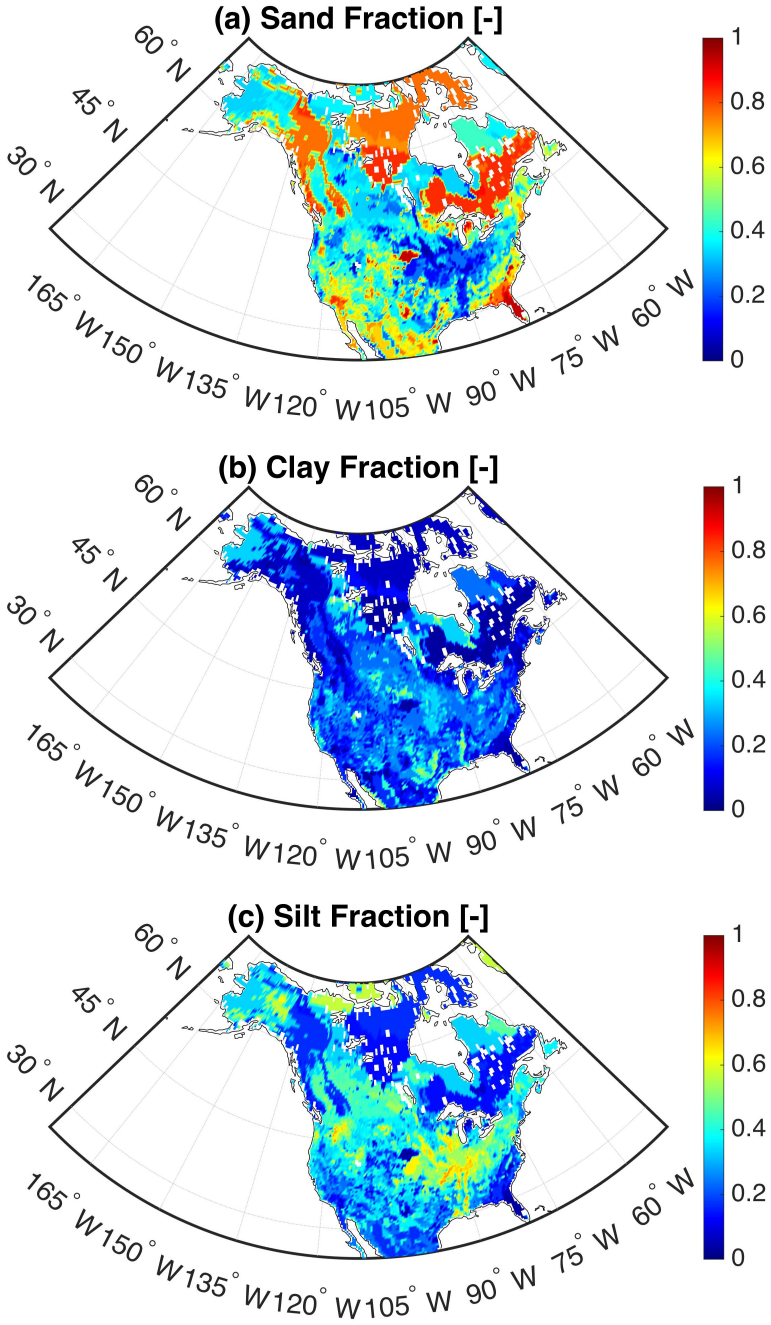

Figure A.1: Maps of (a) sand, (b) clay, and (c) silt fractions across the study domain.

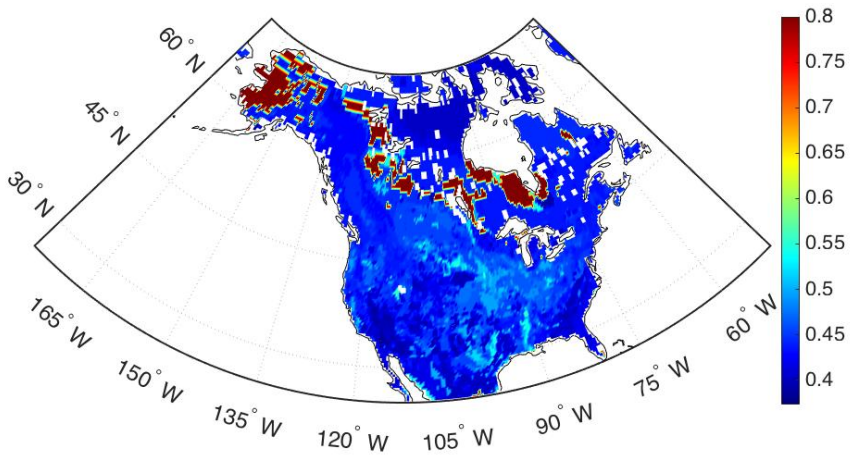

Figure A.2: Maps of porosity utilized in the GEOS L-band RTM across the study domain.

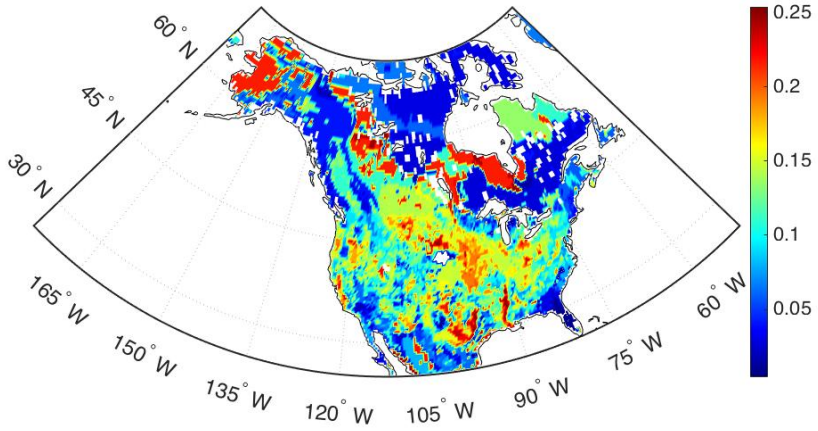

Figure A.3: Maps of wilting point (WP) utilized in the GEOS L-band RTM across the study domain.

Table A.1: Summary of the literature-based values assigned for the calibration of the key parameters accounting for surface roughness and vegetation conditions (modified from De Lannoy et al. [53]). Note that subscript p represents the polarization (i.e., horizontal or vertical polarization).

Land cover	h=h_{min}=h_{max} [-]	ω [-]	**LEWT [kgm^{-2}]**	$\mathbf{b_p}$[-]	$\mathbf{N_{r_p}}$
Broad deciduous	1.66	0.05	1	0.33	0
Neeedleleaf deciduous	1.66	0.05	1	0.33	0
Grassland	1.66	0.05	0.5	0.2	0
Shrub	1.66	0.05	0.5	0.3	0
Dwarf	1.66	0.05	0.5	0.15	0

Figures A.2 and A.3 illustrate the spatial distribution of porosity and wilting point, respectively, which are used in the L-band RTM in this study. Parameterization of wilting point (WP) was computed using the fraction of sand (f_s) and clay (f_c) shown in the Figures A.1(a) and (b) following the equation A.1.

$$WP = 0.06774 - 0.00064 \times f_s + 0.00478 \times f_c \tag{A.1}$$

Wilting point is also utilized to estimate the transition of soil moisture (WT), which plays a key role in parameterizing effective roughness height (h) described in Section 3.2.1. Figure A.4 describes the WT over the study domain. WT is calculated as follows:

$$WT = 0.48 \times WP + 0.165 \tag{A.2}$$

In addition to the WT, field capacity is utilized in the L-band RTM which is represented in Figure A.5. Field capacity is included in the RTM as an additional constraint in the parameterization of effective roughness height, h.

In order to parameterize the electromagnetic response of vegetation, vegetation

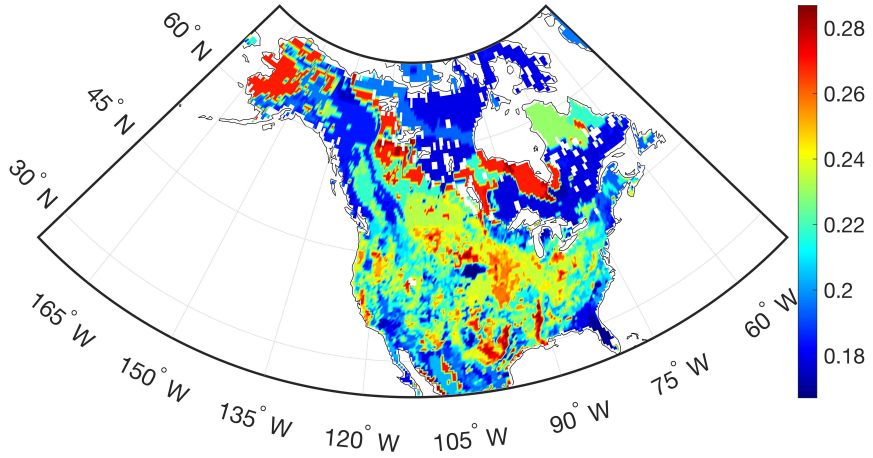

Figure A.4: Maps of transition of soil moisture (WT) utilized in GEOS-5 L-band RTM across the study domain

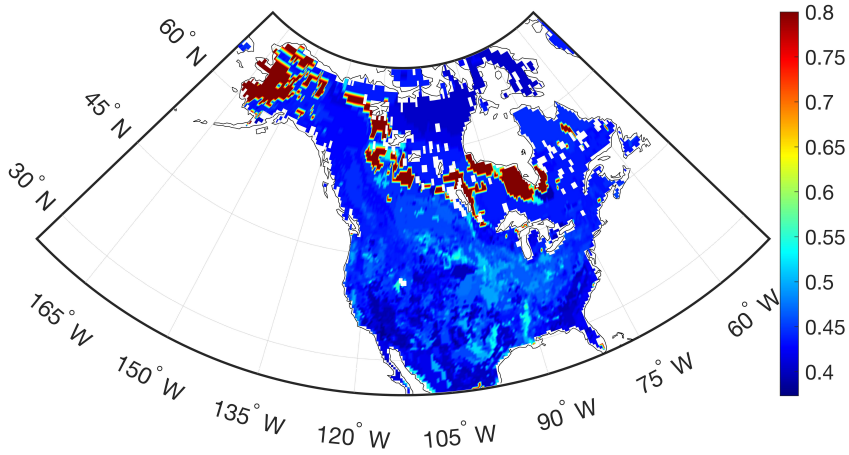

Figure A.5: Maps of field capacity (FC) utilized in the GEOS-5 L-band RTM across the study domain

transmissivity ($\tau_{veg,p}$) is calculated based on the LEWT, b_p, and leaf area index (LAI). $\tau_{veg,p}$ is further utilized in acquiring the vegetation attenuation (A_p) expressed in Equation 3.2.1. Figures A.6 and illustrate the spatial distribution of the $\tau_{veg,p}$ and A_p, respectively, over the study domain for 02 July 2012.

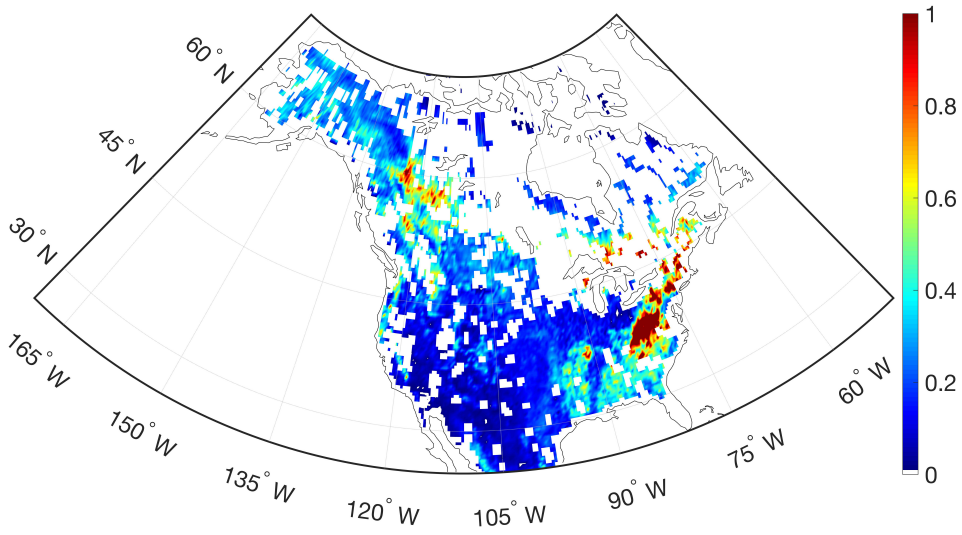

Figure A.6: Maps of vegetation transmissivity ($\tau_{veg,p}$) for 02 July 2012 over the study domain.

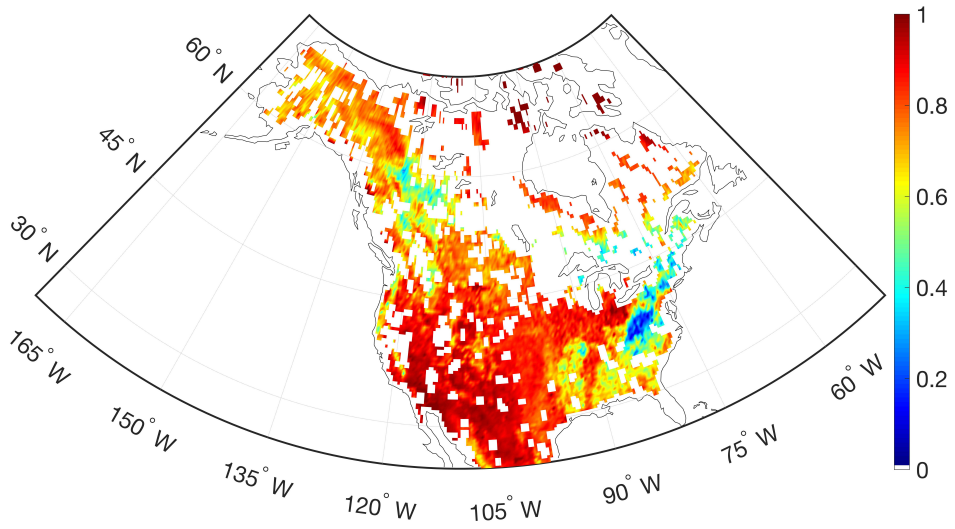

Figure A.7: Maps of vegetation attenuation (A_p) for 02 July 2012 across the study domain.

Appendix B: Support Vector Machine Regression

Figure B.1 illustrates a schematic for the one-dimensional, nonlinear support vector machine (SVM) regression along with the variables utilized in SVM regression. Assume a $[M \times N]$ training matrix, x, such that it contains N = 4 different geophysical variables simulated from Noah-MP (e.g., snow water equivalent, snow density, snow liquid water content, and top layer snow temperature) used in characterizing the physical conditions of snow at M different times for a given location in space. The training targets (z; Sentinel-1 backscatter observations in this paper) have a size of $[M \times 1]$.

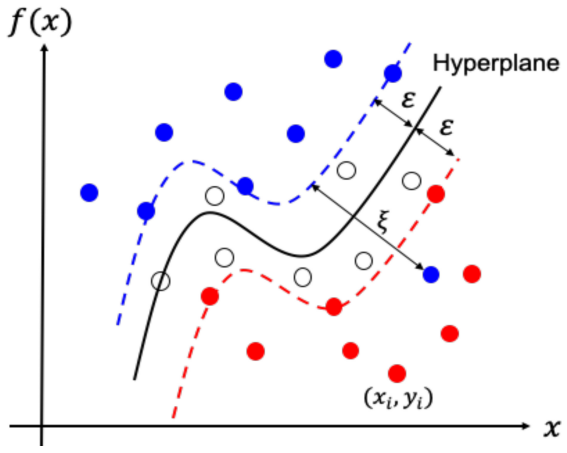

Figure B.1: Schematic for nonlinear support vector machine regression and corresponding variables. Note that dots on the dashed lines represents the data points selected as the so-called support vectors.

This study utilized the ε-SV regression introduced in Vapnik [213]. The main goal for ε-SV regression is to minimize the objective function, which can be written as:

$$f(\omega, \delta) = \langle w \cdot \phi(x) \rangle + \delta \tag{B.1}$$

where ω is a weighting factor and $\phi(x)$ is nonlinear function for mapping the geophysical variables into observation (i.e., backscatter) space. $\langle w \cdot \phi(x) \rangle$ refers to the inner (dot) product of ω and $\phi(x)$. δ represents the bias coefficient. As the main goal of SVM regression is to optimize parameters to increase the accuracy of $f(\omega, \delta)$, the basic formulation of nonlinear SVM regression can be expressed as follows:

$$\begin{aligned} &\text{minimize} \ \ \frac{1}{2}\|w\|^2 + C\sum_{i=1}^{m}(\xi_i + \xi_i^*) \\ &\text{subject to} \ \begin{cases} f(\omega, \delta) - z_i \leq \varepsilon + \xi_i \\ z_i - f(\omega, \delta) \leq \varepsilon + \xi_i^* \\ \xi_i, \ \xi_i^* \geq 0 \end{cases} \end{aligned} \tag{B.2}$$

where $C(> 0)$ is the user-defined constant representing the trade-off between tolerance of ε and $f(\omega, \delta)$ [194]. In this study, C is estimated based on the difference between the maximum and minimum training targets (e.g., co-polarized and cross-polarized backscatter). ξ_i and ξ_i^* are slack variables and z_i represents the Sentinel-1 backscatter observation at timestep i. For the ε, representing the margins, the range was set from $0 \sim 5$ before SVM training and it is optimized during the training procedure. Optimization of equation B.2 is commonly regarded as a dual optimization problem [35] and can be solved by applying a dual set of Lagrangian multipliers (α_i and α_i^*) as:

$$\begin{aligned} \text{minimize } & \frac{1}{2}\sum_{i,j=1}^{m}(\alpha_i - \alpha_i^*)(\alpha_j - \alpha_j^*)\langle\phi(x_i)\cdot\phi(x_j)\rangle \\ & + \sum_{i=1}^{m}\varepsilon(\alpha_i + \alpha_i^*) - \sum_{i=1}^{m} z_i(\alpha_i + \alpha_i^*) \\ \text{subject to } & \begin{cases} \sum_{i=1}^{m}\varepsilon(\alpha_i + \alpha_i^*) = 0 \\ \\ \alpha_i,\ \alpha_i^* \in [0, C], i = 1, 2, ..., m \end{cases} \end{aligned} \tag{B.3}$$

In real-world applications, computation of $\langle\phi(x_i)\cdot\phi(x_j)\rangle$ can be too computationally costly, which motivates one to employ a kernel technique for improving computational efficiency by directly mapping the solution into higher-dimensional space [75, 194]. There are different types of kernel functions that can be used such as linear, nonlinear, and polynomial forms [26]. Among them, the radial basis kernel function (RBF) is employed in this study due to its advantages in dealing with datasets having nonlinear relationships between inputs and outputs (training target). As such, the kernel function can be expressed as:

$$k(x_i, x_j) = \langle\phi(x_i), \phi(x_j)\rangle = exp\{-\gamma\|x_i - x_j\|^2\} \tag{B.4}$$

where x_i and x_j represent a single instance of $\mathbf{x}$ in time and space and $\|\cdot\|$ represents the Euclidean norm between $\phi(x_i)$ and $\phi(x_j)$. The positive parameter, γ, is an adjustable parameter to control the width of the Gaussian variable. When γ is small, more weight will be given to the points closer to x_i while a larger γ indicates more importance to points far from x_i. In this study, the initial range of γ was prescribed from the 2^{-7} to 2^7.

Replacing the dot product with the RBF kernel function expressed in Equation

B.4 allows for Equation B.3 to be rewritten as:

$$\begin{aligned} \text{minimize } & \frac{1}{2}\sum_{i,j=1}^{m}(\alpha_i - \alpha_i^*)(\alpha_j - \alpha_j^*)k(x_i, x_j) \\ & + \sum_{i=1}^{m}\varepsilon(\alpha_i + \alpha_i^*) - \sum_{i=1}^{m} z_i(\alpha_i + \alpha_i^*) \\ \text{subject to } & \begin{cases} \sum_{i=1}^{m}\varepsilon(\alpha_i + \alpha_i^*) = 0 \\ \\ \alpha_i,\ \alpha_i^* \in [0, C], i = 1, 2, ..., m \end{cases} \end{aligned} \tag{B.5}$$

In a similar manner, the weight vector, w, can be calculated as follows:

$$w = \sum_{i=1}^{m}(\alpha_i - \alpha_i^*)\Phi(x_i) \tag{B.6}$$

$$f(\omega, \delta) = \sum_{i=1}^{m}(\alpha_i - \alpha_i^*)k(x_i, x_j) + \delta \tag{B.7}$$

Note that bias coefficient, δ is computed during the training procedure based on the Karush-Kuhn-Tucker (KKT) conditions [116], and in turn, w can be calculated so that which is utilized for estimating the prediction. Details of the SVM training and prediction schematic is summarized in Figure B.2.

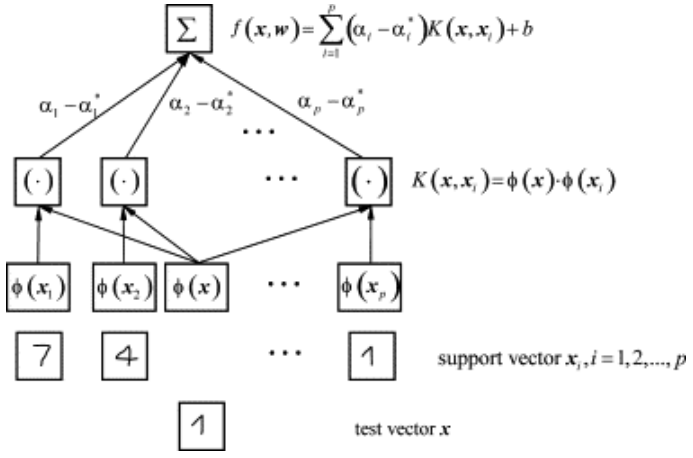

Figure B.2: Schematic of the regression procedures constructed by the support vector machine [173].

Example maps of different parameter values for the trained support vector machines during 15 January 2017 to 29 January 2017 using combined training target sets and fortnightly training window are shown in Figures B.3 and B.4. The total number of parameters in a trained SVM is dependent on the number of so-called support vectors, which is dependent on the size of the training set. Therefore, there is no singular, deterministic number of the parameter values illustrated in Figures B.3 and B.4 merely demonstrate a few of the myriad of parameter values in in order to provide the reader with a better idea for how a well-trained SVM in this study is constructed. For instance, SWE and snow density showed positive bias during the 15 January 2017 to 29 January 2017 ranged between 8.3 to 12.5 and 16.0 to 20.0, respectively. In case of snow liquid water content, most of bias showed the negative value (ranged from -8.3 to -6.5) during the period. The range of weights lied from -0.27 to 0.15 throughout the different input variables.

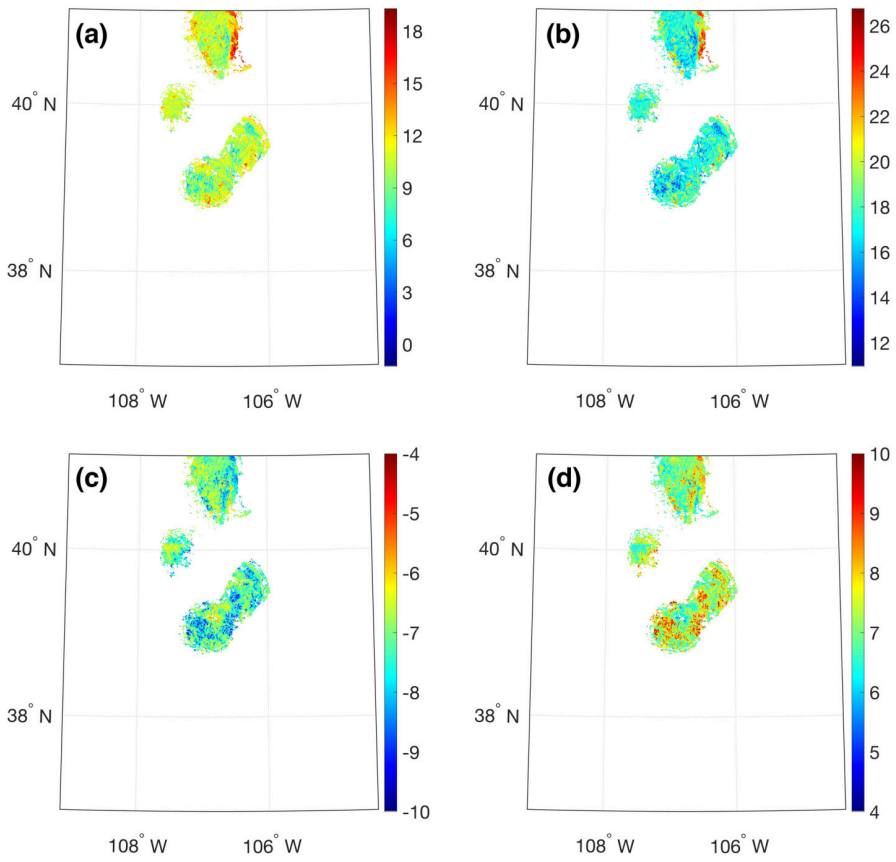

Figure B.3: Maps of bias coefficient, δ, for (a) SWE, (b) snow density, (c) snow liquid water content, and (d) top layer snow temperature used for predicting backscatter during 15 January 2017 to 29 January 2017.

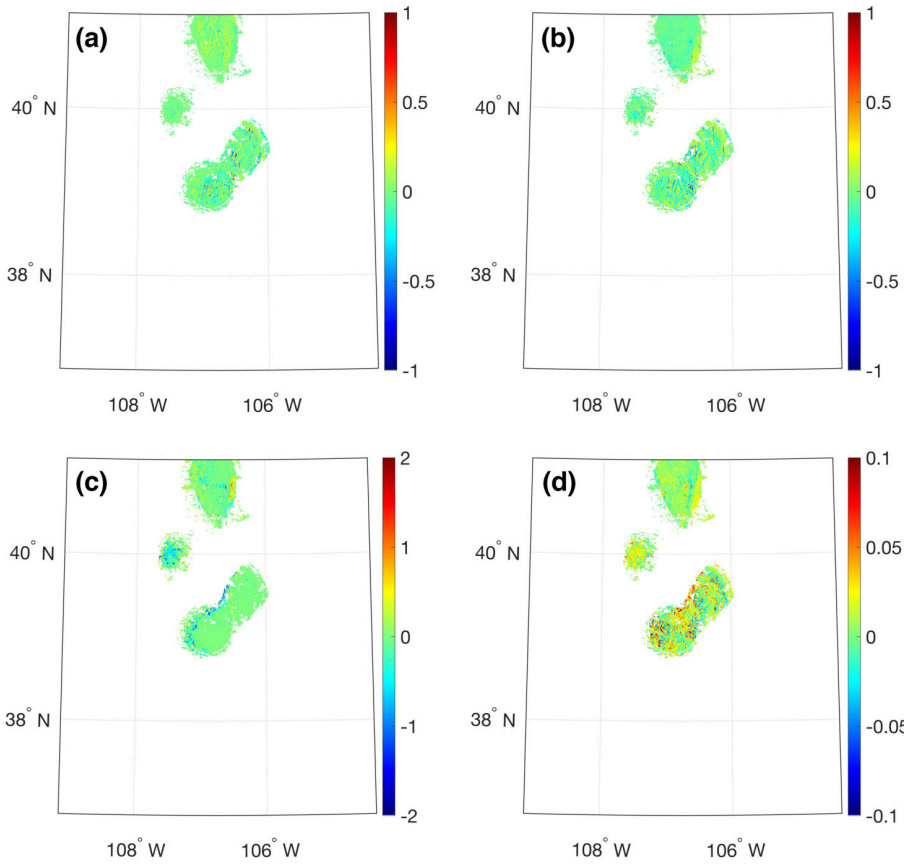

Figure B.4: Maps of weighting factor, w, for (a) SWE, (b) snow density, (c) snow liquid water content, and (d) top layer snow temperature used for predicting backscatter during 15 January 2017 to 29 January 2017.

Bibliography

[1] Abdalati, W., and Steffen, K. Snowmelt on the Greenland Ice Sheet as Derived from Passive Microwave Satellite Data. *Journal of Climate 10*, 2 (1997), 165–175.

[2] Ahmad, J. A., Forman, B. A., and Kwon, Y. Analyzing machine learning predictions of passive microwave brightness temperature spectral difference over snow-covered terrain in High Mountain Asia. *Frontiers in Earth Science 7* (2019), 212.

[3] Andreadis, K. M., and Lettenmaier, D. P. Assimilating remotely sensed snow observations into a macroscale hydrology model. *Advances in Water Resources 29*, 6 (2006), 872–886.

[4] Angueira, P., and Romo, J. A. *Equipment and Subsystem Technology Aspects: A Radio Link Designer Approach*. John Wiley & Sons, Ltd, 2012, ch. 4, pp. 100–173.

[5] Arsenault, K. R., Houser, P. R., De Lannoy, G. J. M., and Dirmeyer, P. A. Impacts of snow cover fraction data assimilation on modeled energy and moisture budgets. *Journal of Geophysical Research: Atmospheres 118*, 14 (2013), 7489–7504.

[6] Arsenault, K. R., Kumar, S. V., Geiger, J. V., Wang, S., Kemp, E., Mocko, D. M., Beaudoing, H. K., Getirana, A., Navari, M., Li, B., Jacob, J., Wegiel, J., and Peters-Lidard, C. D. The Land surface Data Toolkit (LDT v7.2) – a data fusion environment for land data assimilation systems. *Geoscientific Model Development 11*, 9 (2018), 3605–3621.

[7] Aschbacher, J. *Land surface studies and atmospheric effects by satellite microwave radiometry*. PhD dissertation, University of Innsbruck, 1989.

[8] Aschbacher, J., and Milagro-Peréz, M. P. The European Earth monitoring (GMES) programme: Status and perspectives. *Remote Sensing of Environment 120* (2012), 3 – 8.

[9] Azimi, H., Bonakdari, H., and Ebtehaj, I. Design of radial basis function-based support vector regression in predicting the discharge coefficient of a side weir in a trapezoidal channel. *Applied Water Science 9*, 4 (2019), 78.

[10] Baghdadi, N., Gauthier, Y., and Bernier, M. Capability of multitemporal ERS-1 SAR data for wet-snow mapping. *Remote Sensing of Environment 60*, 2 (1997), 174 – 186.

[11] Bair, E. H., Rittger, K., Skiles, S. M., and Dozier, J. An examination of snow albedo estimates from modis and their impact on snow water equivalent reconstruction. *Water Resources Research 55*, 9 (2019), 7826–7842.

[12] Barba, A. A., and d'Amore, M. Relevance of dielectric properties in microwave assisted processes. *Microwave materials characterization 6* (2012), 91–118.

[13] Barnett, T. P., Adam, J. C., and Lettenmaier, D. P. Potential impacts of a warming climate on water availability in snow-dominated regions. *Nature 438*, 7066 (2005), 303–309.

[14] Bernier, M., Dedieu, J.-P., and Duguay, Y. Snow characterization using radar imaging. In *Land Surface Remote Sensing in Continental Hydrology*, N. Baghdadi and M. Zribi, Eds. Elsevier, 2016, pp. 139 – 182.

[15] Bernier, M., Fortin, J.-P., Gauthier, Y., Gauthier, R., Roy, R., and Vincent, P. Determination of snow water equivalent using radarsat sar data in eastern canada. *Hydrological Processes 13*, 18 (1999), 3041–3051.

[16] Best, M., Pryor, M., Clark, D., Rooney, G., Essery, R., Ménard, C., Edwards, J., Hendry, M., Porson, A., Gedney, N Mercado, L., Sitch, S., Blyth, E., Boucher, O., Cox, P., Grimmond, C., and Harding, R. The Joint UK Land Environment Simulator (JULES), model description–Part 1: energy and water fluxes. *Geoscientific Model Development 4*, 1 (2011), 677–699.

[17] Bindlish, R., Jackson, T., Cosh, M., Zhao, T., and O'Neill, P. Global soil moisture from the Aquarius/SAC-D satellite: Description and initial assessment. *IEEE Geoscience and Remote Sensing Letters 12*, 5 (2015), 923–927.

[18] Biswas, S. K., Jones, L., Rocca, D., and Gallio, J. Aquarius/SAC-D Microwave Radiometer (MWR): Instrument description & brightness temperature calibration. In *2012 IEEE International Geoscience and Remote Sensing Symposium* (2012), pp. 2956–2959.

[19] Blyth, E., Gash, J., Lloyd, A., Pryor, M., Weedon, G. P., and Shuttleworth, J. Evaluating the JULES land surface model energy fluxes using FLUXNET data. *Journal of Hydrometeorology 11*, 2 (2010), 509–519.

[20] Bormann, K. J., Brown, R. D., Derksen, C., and Painter, T. H. Estimating snow-cover trends from space. *Nature Climate Change 8*, 11 (2018), 924–928.

[21] Bosilovich, M. G., Akella, S., Coy, L., Cullather, R., Draper, C., Gelaro, Ronald, K., Robin, Liu, Q., Molod, A., Norris, P., Wargan, K., Chao, W., Reichle, R., Takacs, L., Vikhliaev, Y., Bloom, S., Collow, A., Firth, S., Labow, Gordo nnd Partyka, G., Pawson, S., Reale, O., Schubert, S. D., and Suarez, M. *MERRA-2: Initial evaluation of the climate*. National Aeronautics and Space Administration, Goddard Space Flight Center, 2015.

[22] Bowden, G. J., Dandy, G. C., and Maier, H. R. Input determination for neural network models in water resources applications. Part 1—background and methodology. *Journal of Hydrology 301*, 1 (2005), 75 – 92.

[23] Brodzik, M. J., Billingsley, B., Haran, T., Raup, B., and Savoie, M. H. EASE-Grid 2.0: Incremental but Significant Improvements for Earth-Gridded Data Sets. *ISPRS International Journal of Geo-Information 1*, 3 (2012), 32–45.

[24] Brutsaert, W. *Hydrology: an introduction*. Cambridge University Press, 2005.

[25] Cai, X., Yang, Z.-L., David, C. H., Niu, G.-Y., and Rodell, M. Hydrological evaluation of the Noah-MP land surface model for the Mississippi River Basin. *Journal of Geophysical Research: Atmospheres 119*, 1 (2014), 23–38.

[26] Camps-Valls, G., Gomez-Chova, L., Munoz-Mari, J., Vila-Frances, J., and Calpe-Maravilla, J. Composite kernels for hyperspectral image classification. *IEEE Geoscience and Remote Sensing Letters 3*, 1 (Jan 2006), 93–97.

[27] Cao, Y., Yang, X., and Zhu, X. Retrieval snow depth by artificial neural network methodology from integrated AMSR-E and in-situ data—A case study in Qinghai-Tibet Plateau. *Chinese Geographical Science 18*, 4 (2008), 356–360.

[28] Carlyle-Moses, D. E., Levia, D. F., Iida, S., Michalzik, B., Nanko, K., and Tischer, A. *Forest-Water Interactions*, vol. 240. Springer Nature, 2019.

[29] Carrera, M. L., Bilodeau, B., Bélair, S., Abrahamowicz, M., Russell, A., and Wang, X. Assimilation of Passive L-band Microwave Brightness Temperatures in the Canadian Land Data Assimilation System: Impacts on Short-Range Warm Season Numerical Weather Prediction. *Journal of Hydrometeorology 20*, 6 (2019), 1053–1079.

[30] Cerveny, R. S. The Western San Juan Mountains: Their Geology, Ecology, and Human History. *American Scientist 85*, 3 (1997), 281–282.

[31] Chan, S. K., Bindlish, R., O'Neill, P. E., Njoku, E., Jackson, T., Colliander, A., Chen, F., Burgin, M., Dunbar, S., Piepmeier, J., Yueh, S., Entekhabi, D., Cosh, M. H., Caldwell, T., Walker, J., Wu, X., Berg, A., Rowlandson, T., Pacheco, A., McNairn, H., Thibeault, M., Martínez-Fernández, J., González-Zamora, A., Seyfried, M., Bosch, D., Starks, P., Goodrich, D., Prueger, J., Palecki, M., Small, E. E., Zreda, M., Calvet, J., Crow, W. T., and Kerr, Y. Assessment of the SMAP Passive Soil Moisture Product. *IEEE Transactions on Geoscience and Remote Sensing 54*, 8 (2016), 4994–5007.

[32] Chandrasekhar, S. *Radiative transfer*. Courier Corporation, 2013.

[33] Chang, A., Foster, J., and Hall, D. Nimbus-7 SMMR Derived Global Snow Cover Parameters. *Annals of Glaciology 9* (1987), 39–44.

[34] Chang, A. T. C., and Tsang, L. A Neural Network Approach to Inversion of Snow Water Equivalent from Passive Microwave Measurements. *Nordic Hydrology 23* (1992), 173–182.

[35] Chang, C.-C., and Lin, C.-J. Libsvm: A library for support vector machines. *ACM transactions on intelligent systems and technology (TIST) 2*, 3 (2011), 27.

[36] Che, T., Li, X., Jin, R., and Huang, C. Assimilating passive microwave remote sensing data into a land surface model to improve the estimation of snow depth. *Remote Sensing of Environment 143* (2014), 54–63.

[37] Chen, F., Barlage, M., Tewari, M., Rasmussen, R., Jin, J., Lettenmaier, D., Livneh, B., Lin, C., Miguez-Macho, G., Niu, Guo-Yue Wen, L., and Yang, Z.-L. Modeling seasonal snowpack evolution in the complex terrain and forested Colorado Headwaters region: A model intercomparison study. *Journal of Geophysical Research: Atmospheres 119*, 24 (2014), 13–795.

[38] Chen, F., Zhang, G., Barlage, M., Zhang, Y., Hicke, J. A., Meddens, A., Zhou, G., Massman, W. J., and Frank, J. An Observational and Modeling Study of Impacts of Bark Beetle–Caused Tree Mortality on Surface Energy and Hydrological Cycles. *Journal of Hydrometeorology 16*, 2 (2015), 744–761.

[39] Chen, Y., Yang, K., Qin, J., Cui, Q., Lu, H., La, Z., Han, M., and Tang, W. Evaluation of SMAP, SMOS, and AMSR2 soil moisture retrievals against observations from two networks on the Tibetan Plateau. *Journal of Geophysical Research: Atmospheres 122*, 11 (2017), 5780–5792.

[40] Cho, E., Tuttle, S. E., and Jacobs, J. M. Evaluating Consistency of Snow Water Equivalent Retrievals from Passive Microwave Sensors over the North Central U. S.: SSM/I vs. SSMIS and AMSR-E vs. AMSR2. *Remote Sensing 9*, 5 (2017).

[41] Clark, M. P., Rupp, D. E., Woods, R. A., Zheng, X., Ibbitt, R. P., Slater, A. G., Schmidt, J., and Uddstrom, M. J. Hydrological data assimilation with the ensemble Kalman filter: Use of streamflow observations to update states in a distributed hydrological model. *Advances in Water Resources 31*, 10 (2008), 1309–1324.

[42] Clifford, D. Global estimates of snow water equivalent from passive microwave instruments: History, challenges and future developments. *International Journal of Remote Sensing 31*, 14 (2010), 3707–3726.

[43] Collow, T. W., Robock, A., Basara, J. B., and Illston, B. G. Evaluation of SMOS retrievals of soil moisture over the central United States with currently available in situ observations. *Journal of Geophysical Research: Atmospheres 117*, D9 (2012).

[44] Conde, V., Nico, G., Mateus, P., Catalão, J., Kontu, A., and Gritsevich, M. On The Estimation of Temporal Changes of Snow Water Equivalent by Spaceborne SAR Interferometry: A New Application for the Sentinel-1 Mission. *Journal of Hydrology and Hydromechanics 67*, 1 (2019), 93–100.

[45] Cui, H., Jiang, L., Du, J., Zhao, S., Wang, G., Lu, Z., and Wang, J. Evaluation and analysis of AMSR-2, SMOS, and SMAP soil moisture products in the Genhe area of China. *Journal of Geophysical Research: Atmospheres 122*, 16 (2017), 8650–8666.

[46] Dai, Y., Zeng, X., Dickinson, R. E., Baker, I., Bonan, G. B., Bosilovich, M. G., Denning, A. S., Dirmeyer, P. A., Houser, P. R., Niu, G., Oleson, K. W., Schlosser, C. A., and Yang, Z.-L. The Common Land Model. *Bulletin of the Americn Meteorological Society 84*, 8 (2003), 1013–1024.

[47] Davis, D. T., Chen, Z., Tsang, L., Hwang, J. ., and Chang, A. T. C. Retrieval of snow parameters by iterative inversion of a neural network. *IEEE Transactions on Geoscience and Remote Sensing 31*, 4 (July 1993), 842–852.

[48] de Almeida, B., Gomes, B. S., and Leite, V. C. Particle swarm optimization: A powerful technique for solving engineering problems. In *Swarm*

Intelligence-Recent Advances, New Perspectives and Applications. IntechOpen, 2019.

[49] De Lannoy, G., Reichle, R. H., Arsenault, K. R., Houser, P. R., Kumar, S., Verhoest, N. E. C., and Pauwels, V. R. N. Multiscale assimilation of Advanced Microwave Scanning Radiometer–EOS snow water equivalent and Moderate Resolution Imaging Spectroradiometer snow cover fraction observations in northern Colorado. *Water Resources Research 48*, 1 (2012).

[50] De Lannoy, G. J., Koster, R. D., Reichle, R. H., Mahanama, S. P., and Liu, Q. An updated treatment of soil texture and associated hydraulic properties in a global land modeling system. *Journal of Advances in Modeling Earth Systems 06* (2014), 957–979.

[51] De Lannoy, G. J., Reichle, R. H., Houser, P. R., Arsenault, K. R., Verhoest, N. E., and Pauwels, V. R. Satellite-scale snow water equivalent assimilation into a high-resolution land surface model. *Journal of Hydrometeorology 11*, 2 (2010), 352–369.

[52] De Lannoy, G. J. M., and Reichle, R. H. Assimilation of smos brightness temperatures or soil moisture retrievals into a land surface model. *Hydrology and Earth System Sciences 20*, 12 (2016), 4895–4911.

[53] De Lannoy, G. J. M., Reichle, R. H., and Pauwels, V. R. N. Global Calibration of the GEOS-5 L-Band Microwave Radiative Transfer Model over Nonfrozen Land Using SMOS Observations. *Journal of Hydrometeorology 14*, 3 (2013), 765–785.

[54] De Lannoy, G. J. M., Reichle, R. H., and Vrugt, J. A. Uncertainty quantification of GEOS-5 L-band radiative transfer model parameters using Bayesian inference and SMOS observations. *Remote Sensing of Environment 148* (2014), 146 – 157.

[55] de Rosnay, P., Drusch, M., Boone, A., Balsamo, G., Decharme, B., Harris, P., Kerr, Y., Pellarin, T., Polcher, J., and Wigneron, J.-P. AMMA Land Surface Model Intercomparison Experiment coupled to the Community Microwave Emission Model: ALMIP-MEM. *Journal of Geophysical Research: Atmospheres 114*, D5 (2009).

[56] De Zan, F., and Monti Guarnieri, A. Topsar: Terrain observation by progressive scans. *IEEE Transactions on Geoscience and Remote Sensing 44*, 9 (Sep. 2006), 2352–2360.

[57] Dechant, C., and Moradkhani, H. Radiance data assimilation for operational snow and streamflow forecasting. *Advances in Water Resources 34*, 3 (2011), 351 – 364.

[58] Dedieu, J. P., De Farias, G. B., Castaings, T., Allain-Bailhache, S., Pottier, E., Durand, Y., and Bernier, M. Interpretation of a RADARSAT-2 fully polarimetric time-series for snow cover studies in an Alpine context – first results. *Canidian Journal of Remote Sensing 38*, 3 (2012), 336–351.

[59] Derksen, C., Toose, P., Rees, A., Wang, L., English, M., Walker, A., and Sturm, M. Development of a tundra-specific snow water equivalent retrieval algorithm for satellite passive microwave data. *Remote Sensing of Environment 114*, 8 (2010), 1699–1709.

[60] Dibike, Y. B., Velickov, S., Solomatine, D., and Abbott, M. B. Model induction with support vector machines: introduction and applications. *Journal of Computing in Civil Engineering 15*, 3 (2001), 208–216.

[61] Dobreva, I. D., and Klein, A. G. Fractional snow cover mapping through artificial neural network analysis of modis surface reflectance. *Remote Sensing of Environment 115*, 12 (2011), 3355 – 3366.

[62] Dong, J., Walker, J. P., Houser, P. R., and Sun, C. Scanning multichannel microwave radiometer snow water equivalent assimilation. *Journal of Geophysical Research: Atmospheres 112*, D7 (2007).

[63] Dressler, K. A., Leavesley, G. H., Bales, R. C., and Fassnacht, S. R. Evaluation of gridded snow water equivalent and satellite snow cover products for mountain basins in a hydrologic model. *Hydrological Processes 20*, 4 (2006), 673–688.

[64] Drusch, M. Initializing numerical weather prediction models with satellite-derived surface soil moisture: Data assimilation experiments with ECMWF's Integrated Forecast System and the TMI soil moisture data set. *Journal of Geophysical Research: Atmospheres 112*, D3 (2007).

[65] Drusch, M., Holmes, T., de Rosnay, P., and Balsamo, G. Comparing ERA-40-based L-band brightness temperatures with Skylab observations: A calibration/validation study using the Community Microwave Emission Model. *Journal of hydrometeorology 10*, 1 (2009), 213–226.

[66] Du, J., Shi, J., and Rott, H. Comparison between a multi-scattering and multi-layer snow scattering model and its parameterized snow backscattering model. *Remote Sensing of Environment 114*, 5 (2010), 1089 – 1098.

[67] Eckerstorfer, M., and Malnes, E. Manual detection of snow avalanche debris using high-resolution Radarsat-2 SAR images. *Cold Regions Science and Technology 120* (2015), 205 – 218.

[68] Ek, M. B., Mitchell, K. E., Lin, Y., Rogers, E., Grunmann, P., Koren, V., Gayno, G., and Tarpley, J. D. Implementation of Noah

land surface model advances in the National Centers for Environmental Prediction operational mesoscale Eta model. *Journal of Geophysical Research: Atmospheres 108*, D22 (2003).

[69] Entekhabi, D., Njoku, E. G., O'Neill, P. E., Kellogg, K. H., Crow, W. T., Edelstein, W. N., Entin, J. K., Goodman, S. D., Jackson, T. J., Johnson, J., Kimball, J., Piepmeier, J. R., Koster, R. D., Martin, N., McDonald, K. C., Moghaddam, M., Moran, S., Reichle, R., Shi, J. C., Spencer, M. W., Thurman, S. W., Tsang, L., and Van Zyl, J. The soil moisture active passive (SMAP) mission. *Proceedings of the IEEE 98*, 5 (2010), 704–716.

[70] Entekhabi, D., Reichle, R. H., Koster, R. D., and Crow, W. T. Performance Metrics for Soil Moisture Retrievals and Application Requirements. *Journal of Hydrometeorology 11*, 3 (jun 2010), 832–840.

[71] Evensen, G. *Data assimilation: the ensemble Kalman filter*. Springer Science & Business Media, 2009.

[72] Feldman, A. F., Short Gianotti, D. J., Trigo, I. F., Salvucci, G. D., and Entekhabi, D. Satellite-Based Assessment of Land Surface Energy Partitioning–Soil Moisture Relationships and Effects of Confounding Variables. *Water Resources Research 55*, 12 (2019), 10657–10677.

[73] Fenicia, F., Kavetski, D., and Savenije, H. H. G. Elements of a flexible approach for conceptual hydrological modeling: 1. Motivation and theoretical development. *Water Resources Research 47*, 11 (2011).

[74] Forman, B. A., and Reichle, R. H. Using a Support Vector Machine and a Land Surface Model to Estimate Large-Scale Passive Microwave Brightness Temperatures over Snow-Covered Land in North America. *IEEE Journal of Selected Topics in Applied Earth Observations and Remote Sensing 8*, 9 (2015), 4431–4441.

[75] Forman, B. A., Reichle, R. H., and Derksen, C. Estimating Passive Microwave Brightness Temperature Over Snow-Covered Land in North America Using a Land Surface Model and an Artificial Neural Network. *Geoscience and Remote Sensing, IEEE Transactions on 52*, 1 (2014), 235–248.

[76] Forman, B. A., Reichle, R. H., and Rodell, M. Assimilation of terrestrial water storage from GRACE in a snow-dominated basin. *Water Resource Research 48*, November 2011 (2012), 1–14.

[77] Forman, B. A., and Xue, Y. Machine learning predictions of passive microwave brightness temperature over snow-covered land using the special sensor microwave imager (SSM/I). *Physical Geography 38*, 2 (2017), 176–196.

[78] Foster, J. L., Sun, C., Walker, J. P., Kelly, R., Chang, A., Dong, J., and Powell, H. Quantifying the uncertainty in passive microwave snow water equivalent observations. *Remote Sensing of Environment 94*, 2 (2005), 187–203.

[79] Friedl, M. A., Sulla-Menashe, D., Tan, B., Schneider, A., Ramankutty, N., Sibley, A., and Huang, X. MODIS Collection 5 global land cover: Algorithm refinements and characterization of new datasets. *Remote Sensing of Environment 114*, 1 (2010), 168–182.

[80] Frulla, L. A., Milovich, J. A., Karszenbaum, H., and Gagliardini, D. A. Radiometric corrections and calibration of sar images. In *IGARSS '98. Sensing and Managing the Environment. 1998 IEEE International Geoscience and Remote Sensing. Symposium Proceedings. (Cat. No.98CH36174)* (July 1998), vol. 2, pp. 1147–1149 vol.2.

[81] Garnaud, C., Bélair, S., Carrera, M. L., Derksen, C., Bilodeau, B., Abrahamowicz, M., Gauthier, N., and Vionnet, V. Quantifying snow mass mission concept trade-offs using an observing system simulation experiment. *Journal of Hydrometeorology 20*, 1 (2019), 155–173.

[82] Gelaro, R., McCarty, W., Suárez, M. J., Todling, R., Molod, A., Takacs, L., Randles, C. A., Darmenov, A., Bosilovich, M. G., Reichle, R., Wargan, K., Coy, L., Cullather, R., Draper, C., Akella, S., Buchard, V., Conaty, A., da Silva, A. M., Gu, W., Kim, G.-K., Koster, R., Lucchesi, R., Merkova, D., Nielsen, J. E., Partyka, G., Pawson, S., Putman, W., Rienecker, M., Schubert, S. D., Sienkiewicz, M., and Zhao, B. The Modern-Era Retrospective Analysis for Research and Applications, Version 2 (MERRA-2). *Journal of Climate 30*, 14 (2017), 5419–5454.

[83] Getirana, A., Boone, A., Yamazaki, D., Decharme, B., Papa, F., and Mognard, N. The Hydrological Modeling and Analysis Platform (HyMAP): Evaluation in the Amazon Basin. *Journal of Hydrometeorology 13*, 6 (2012), 1641–1665.

[84] Getirana, A. C. V., Dutra, E., Guimberteau, M., Kam, J., Li, H.-Y., Decharme, B., Zhang, Z., Ducharne, A., Boone, A., Balsamo, G., Rodell, M., Toure, A. M., Xue, Y., Peters-Lidard, C. D., Kumar, S. V., Arsenault, K., Drapeau, G., Ruby Leung, L., Ronchail, J., and Sheffield, J. Water balance in the amazon basin from a land surface model ensemble. *Journal of Hydrometeorology 15*, 6 (2014), 2586–2614.

[85] Gichamo, T. Z., and Tarboton, D. G. Ensemble streamflow forecasting using an energy balance snowmelt model coupled to a distributed hydrologic model with assimilation of snow and streamflow observations. *Water Resources Research* (2019).

[86] Graf, T., Koike, T., Li, X., Hirai, M., and Tsutsui, H. Assimilating passive microwave brightness temperature data into a land surface model to improve the snow depth predictability. In *2006 IEEE International Symposium on Geoscience and Remote Sensing* (July 2006), pp. 706–709.

[87] Granata, F., Gargano, R., and de Marinis, G. Support vector regression for rainfall-runoff modeling in urban drainage: A comparison with the EPA's storm water management model. *Water 8*, 3 (2016), 69.

[88] Grant, J. P., Wigneron, J. P., Van de Griend, A. A., Kruszewski, A., Søbjærg, S. S., and Skou, N. A field experiment on microwave forest radiometry: L-band signal behaviour for varying conditions of surface wetness. *Remote Sensing of Environment 109*, 1 (2007), 10–19.

[89] Gruber, A., De Lannoy, G., and Crow, W. A Monte Carlo based adaptive Kalman filtering framework for soil moisture data assimilation. *Remote sensing of environment 228* (2019), 105–114.

[90] Hall, D. K., Kelly, R. E., Foster, J. L., and Chang, A. T. *Estimation of Snow Extent and Snow Properties*. American Cancer Society, 2006, ch. 55.

[91] Hansen, M. C., Potapov, P. V., Moore, R., Hancher, M., Turubanova, S. A., Tyukavina, A., Thau, D., Stehman, S. V., Goetz, S. J., Loveland, T. R., Kommareddy, A., Egorov, A., Chini, L., Justice, C. O., and Townshend, J. R. G. High-resolution global maps of 21st-century forest cover change. *science 342*, 6160 (2013), 850–853.

[92] He, G. J., Jiang, J. X., Xia, Z. H., Hao, Y., Xiao, P. F., Feng, X. Z., and Wang, Z. Snow cover extraction in mountain areas using RadarSat-2 polarimetrie SAR data. In *2016 16th International Conference on Ground Penetrating Radar (GPR)* (June 2016), pp. 1–5.

[93] Helmert, J., Şensoy Şorman, A., Alvarado Montero, R., De Michele, C., De Rosnay, P., Dumont, M., Finger, D. C., Lange, M., Picard, G., Potopová, V., Pullen, S., Vikhamar-Schuler, D., and Arslan, A. N. Review of snow data assimilation methods for hydrological, land surface, meteorological and climate models: Results from a cost harmosnow survey. *Geosciences 8*, 12 (2018).

[94] Holmes, T., De Jeu, R., Owe, M., and Dolman, A. Land surface temperature from Ka band (37 GHz) passive microwave observations. *Journal of Geophysical Research: Atmospheres 114*, D4 (2009).

[95] Holmes, T. R. H., Jackson, T. J., Reichle, R. H., and Basara, J. B. An assessment of surface soil temperature products from numerical weather prediction models using ground-based measurements. *Water Resources Research 48*, 2 (2012).

[96] Hostache, R., Rains, D., Mallick, K., Chini, M., Pelich, R., Lievens, H., Fenicia, F., Corato, G., Verhoest, N. E. C., and Matgen, P. Assimilation of SMOS brightness temperature into a large-scale distributed conceptual hydrological model. *Hydrology and Earth System Sciences Discussions 2019* (2019), 1–28.

[97] Huang, C., Li, X., Lu, L., and Gu, J. Experiments of one-dimensional soil moisture assimilation system based on ensemble kalman filter. *Remote sensing of environment 112*, 3 (2008), 888–900.

[98] Huang, C.-Y., and Anderegg, W. R. L. Large drought-induced aboveground live biomass losses in southern Rocky Mountain aspen forests. *Global Change Biology 18*, 3 (2012), 1016–1027.

[99] Huffman, G. J., Bolvin, D. T., Nelkin, E. J., Wolff, D. B., Adler, R. F., Gu, G., Hong, Y., Bowman, K. P., and Stocker, E. F. The TRMM multisatellite precipitation analysis (TMPA): Quasi-global, multiyear, combined-sensor precipitation estimates at fine scales. *Journal of hydrometeorology 8*, 1 (2007), 38–55.

[100] Jackson, T., and Schmugge, T. Vegetation effects on the microwave emission of soils. *Remote Sensing of Environment 36*, 3 (1991), 203–212.

[101] Jackson, T. J., Bindlish, R., Cosh, M. H., Zhao, T., Starks, P. J., Bosch, D. D., Seyfried, M., Moran, M. S., Goodrich, D. C., Kerr, Y. H., and Leroux, D. Validation of Soil Moisture and Ocean Salinity (SMOS) Soil Moisture Over Watershed Networks in the U.S. *IEEE Transactions on Geoscience and Remote Sensing 50*, 5 (May 2012), 1530–1543.

[102] Johnson, M. T., Ramage, J., Troy, T. J., and Brodzik, M. J. Snowmelt Detection with Calibrated, Enhanced-Resolution Brightness Temperatures (CETB) in Colorado Watersheds. *Water Resources Research 56*, 1 (2020).

[103] Joyce, R. J., Janowiak, J. E., Arkin, P. A., and Xie, P. CMORPH: A method that produces global precipitation estimates from passive microwave and infrared data at high spatial and temporal resolution. *Journal of hydrometeorology 5*, 3 (2004), 487–503.

[104] Kang, D. H., Tan, S., and Kim, E. J. Evaluation of Brightness Temperature Sensitivity to Snowpack Physical Properties Using Coupled Snow Physics and Microwave Radiative Transfer Models. *IEEE Transactions on Geoscience and Remote Sensing 57*, 12 (2019), 10241–10251.

[105] Kelly, R. The AMSR-E Snow Depth Algorithm: Description and Initial Results. *Journal of The Remote Sensing Society of Japan 29*, 1 (2009), 307–317.

[106] Kelly, R. E., Chang, A. T., Tsang, L., and Foster, J. L. A prototype AMSR-E global snow area and snow depth algorithm. *IEEE Transactions on Geoscience and Remote Sensing 41*, 2 (2003), 230–242.

[107] Kennedy, J., and Eberhart, R. Particle swarm optimization. In *Proceedings of ICNN'95-International Conference on Neural Networks* (1995), vol. 4, IEEE, pp. 1942–1948.

[108] Kerr, Y. H., Waldteufel, P., Richaume, P., Wigneron, J. P., Ferrazzoli, P., Mahmoodi, A., Al Bitar, A., Cabot, F., Gruhier, C., Juglea, S. E., Leroux, D., Mialon, A., and Delwart, S. The SMOS soil moisture retrieval algorithm. *IEEE transactions on geoscience and remote sensing 50*, 5 (2012), 1384–1403.

[109] Kerr, Y. H., Waldteufel, P., Wigneron, J. ., Martinuzzi, J., Font, J., and Berger, M. Soil moisture retrieval from space: the soil moisture and ocean salinity (SMOS) mission. *IEEE Transactions on Geoscience and Remote Sensing 39*, 8 (2001), 1729–1735.

[110] Kerr, Y. H., Waldteufel, P., Wigneron, J., Delwart, S., Cabot, F., Boutin, J., Escorihuela, M., Font, J., Reul, N., Gruhier, C., Juglea, S. E., Drinkwater, M. R., Hahne, A., Martín-Neira, M., and Mecklenburg, S. The SMOS Mission: New Tool for Monitoring Key Elements ofthe Global Water Cycle. *Proceedings of the IEEE 98*, 5 (2010), 666–687.

[111] Kim, E., Gatebe, C., Hall, D., Newlin, J., Misakonis, A., Elder, K., Marshall, H. P., Hiemstra, C., Brucker, L., De Marco, E., Crawford, C., Kang, D. H., and Entin, J. NASA's SnowEx campaign: Observing seasonal snow in a forested environment. In *2017 IEEE International Geoscience and Remote Sensing Symposium (IGARSS)* (July 2017), pp. 1388–1390.

[112] Kornelsen, K. C., Cosh, M. H., and Coulibaly, P. Potential of bias correction for downscaling passive microwave and soil moisture data. *Journal of Geophysical Research: Atmospheres 120*, 13 (2015), 6460–6479.

[113] Koster, R. D., Mahanama, S. P., Livneh, B., Lettenmaier, D. P., and Reichle, R. H. Skill in streamflow forecasts derived from large-scale estimates of soil moisture and snow. *Nature Geoscience 3*, 9 (2010), 613–616.

[114] Koster, R. D., and Suarez, M. J. Modeling the land surface boundary in climate models as a composite of independent vegetation stands. *Journal of Geophysical Research: Atmospheres 97*, D3 (1992), 2697–2715.

[115] Koster, R. D., Suarez, M. J., Ducharne, A., Stieglitz, M., and Kumar, P. A catchment-based approach to modeling land surface processes

in a general circulation model 1. Model structure. *Journal of Geophysical Research 105*, D20 (2000), 24809–24822.

[116] Kuhn, H. W., and Tucker, A. W. Nonlinear programming. In *Proceedings of the Second Berkeley Symposium on Mathematical Statistics and Probability* (Berkeley, Calif., 1951), University of California Press, pp. 481–492.

[117] Kumar, S., Mocko, D., Vuyovich, C., and Peters-Lidard, C. Impact of Surface Albedo Assimilation on Snow Estimation. *Remote Sensing 12*, 4 (2020), 645.

[118] Kumar, S. V., Peters-Lidard, C. D., Tian, Y., Houser, P. R., Geiger, J., Olden, S., Lighty, L., Eastman, J. L., Doty, B., Dirmeyer, P., Adams, J., Mitchell, K., Wood, E. F., and Sheffield, J. Land information system: An interoperable framework for high resolution land surface modeling. *Environmental Modelling and Software 21*, 10 (2006), 1402–1415.

[119] Kumar, S. V., Reichle, R. H., Harrison, K. W., Peters-Lidard, C. D., Yatheendradas, S., and Santanello, J. A. A comparison of methods for a priori bias correction in soil moisture data assimilation. *Water Resources Research 48*, 3 (2012), 1–16.

[120] Kunzi, K. F., Patil, S., and Rott, H. Snow-Cover Parameters Retrieved from Nimbus-7 Scanning Multichannel Microwave Radiometer (SMMR) Data. *IEEE Transactions on Geoscience and Remote Sensing GE-20*, 4 (Oct 1982), 452–467.

[121] Kwon, Y., Forman, B. A., Ahmad, J. A., Kumar, S. V., and Yoon, Y. Exploring the Utility of Machine Learning-Based Passive Microwave Brightness Temperature Data Assimilation over Terrestrial Snow in High Mountain Asia. *Remote Sensing 11*, 19 (2019).

[122] Lakshmi, V. Remote sensing of soil moisture. *ISRN Soil Science 2013* (2013).

[123] Langley, P., and Simon, H. A. Applications of machine learning and rule induction. *Communications of the ACM 38*, 11 (1995), 54–64.

[124] Le Vine, D. M., Lagerloef, G. S. E., Colomb, F. R., Yueh, S. H., Member, S., and Pellerano, F. A. Aquarius : An Instrument to Monitor Sea Surface Salinity From Space. *IEEE Transactions on Geoscience and Remote Sensing 45*, 7 (2007), 2040–2050.

[125] Li, D., Wrzesien, M. L., Durand, M., Adam, J., and Lettenmaier, D. P. How much runoff originates as snow in the western united states, and how will that change in the future? *Geophysical Research Letters 44*, 12 (2017), 6163–6172.

[126] Li, H., Wang, Z., He, G., and Man, W. Estimating Snow Depth and Snow Water Equivalence Using Repeat-Pass Interferometric SAR in the Northern Piedmont Region of the Tianshan Mountains. *Journal of Sensors 2017* (2017).

[127] Li, H., Zhang, Z., and Liu, Z. Application of Artificial Neural Networks for Catalysis: A Review. *Catalysts 7*, 10 (2017).

[128] Li, J., and Castagna, J. Support vector machine (svm) pattern recognition to avo classification. *Geophysical Research Letters 31*, 2 (2004).

[129] Liang, S. *Advances in land remote sensing: system, modeling, inversion and application*. Springer Science & Business Media, 2008, ch. 3.3.

[130] Liang, X., Lettenmaier, D. P., and Wood, E. F. One-dimensional statistical dynamic representation of subgrid spatial variability of precipitation in the two-layer variable infiltration capacity model. *Journal of Geophysical Resaerch: Atmosphere 101*, D16 (1996), 21403–21422.

[131] Lievens, H., Demuzere, M., Marshall, H.-P., Reichle, R. H., Brucker, L., Brangers, I., de Rosnay, P., Dumont, M., Girotto, M., Immerzeel, W. W., Jonas, T., Kim, E. J., Koch, I., Marty, C., Saloranta, T., Schöber, J., and De Lannoy, G. J. M. Snow depth variability in the Northern Hemisphere mountains observed from space. *Nature communications 10*, 1 (2019), 4629.

[132] Lievens, H., Reichle, R. H., Liu, Q., De Lannoy, G., Dunbar, R. S., Kim, S., Das, N. N., Cosh, M., Walker, J. P., and Wagner, W. Joint Sentinel-1 and SMAP data assimilation to improve soil moisture estimates. *Geophysical research letters 44*, 12 (2017), 6145–6153.

[133] Lindström, G., Johansson, B., Persson, M., Gardelin, M., and Bergström, S. Development and test of the distributed HBV-96 hydrological model. *Journal of hydrology 201*, 1-4 (1997), 272–288.

[134] Liu, Y., and Margulis, S. A. Deriving Bias and Uncertainty in MERRA-2 Snowfall Precipitation Over High Mountain Asia. *Frontiers in Earth Science 7* (2019), 280.

[135] Liu, Y., Yang, Z., Lin, P., Zheng, Z., and Xie, S. Comparison and evaluation of multiple land surface products for the water budget in the yellow river basin. *Journal of Hydrology* (2019), 124534.

[136] Luojus, K. P., Pulliainen, J. T., Metsamaki, S. J., and Hallikainen, M. T. Enhanced SAR-Based Snow-Covered Area Estimation Method for Boreal Forest Zone. *IEEE Transactions on Geoscience and Remote Sensing 47*, 3 (March 2009), 922–935.

[137] Ma, H., Zeng, J., Chen, N., Zhang, X., Cosh, M. H., and Wang, W. Satellite surface soil moisture from SMAP, SMOS, AMSR2 and ESA CCI: A comprehensive assessment using global ground-based observations. *Remote Sensing of Environment 231* (2019), 111215.

[138] Mahanama, S. P., Koster, R. D., Walker, G. K., Takacs, L. L., Reichle, R. H., De Lannoy, G., Liu, Q., Zhao, B., and Suarez, M. J. Land boundary conditions for the Goddard Earth Observing System model version 5 (GEOS-5) climate modeling system: Recent updates and data file descriptions. Tech. rep., National Aeronautics and Space Administration, sep 2015.

[139] Marin, C., Bertoldi, G., Premier, V., Callegari, M., Brida, C., Hürkamp, K., Tschiersch, J., Zebisch, M., and Notarnicola, C. Use of Sentinel-1 radar observations to evaluate snowmelt dynamics in alpine regions. *The Cryosphere Discussions 2019* (2019), 1–31.

[140] Mätzler, C. Applications of the interaction of microwaves with the natural snow cover. *Remote sensing reviews 2*, 2 (1987), 259–387.

[141] Matzler, C. Microwave permittivity of dry snow. *IEEE Transactions on Geoscience and Remote Sensing 34*, 2 (March 1996), 573–581.

[142] McCuen, R. H. *Modeling hydrologic change : statistical methods*. CRC press, 2016.

[143] McFarland, M. J., Miller, R. L., and Neale, C. M. Land surface temperature derived from the SSM/I passive microwave brightness temperatures. *IEEE Transactions on Geoscience and Remote Sensing 28*, 5 (1990), 839–845.

[144] McLaughlin, D. An integrated approach to hydrologic data assimilation: Interpolation, smoothing, and filtering. *Advances in Water Resources 25*, 8-12 (2002), 1275–1286.

[145] Meyer, T., Weihermüller, L., Vereecken, H., and Jonard, F. Vegetation Optical Depth and Soil Moisture Retrieved from L-Band Radiometry over the Growth Cycle of a Winter Wheat. *Remote Sensing 10*, 10 (2018).

[146] Montero, R. A., Schwanenberg, D., Krahe, P., Lisniak, D., Sensoy, A., Sorman, A. A., and Akkol, B. Moving horizon estimation for assimilating H-SAF remote sensing data into the HBV hydrological model. *Advances in Water Resources 92* (2016), 248 – 257.

[147] Moreira, A., Prats-Iraola, P., Younis, M., Krieger, G., Hajnsek, I., and Papathanassiou, K. P. A tutorial on synthetic aperture radar. *IEEE Geoscience and remote sensing magazine 1*, 1 (2013), 6–43.

[148] Nagler, T., and Rott, H. Retrieval of wet snow by means of multitemporal SAR data. *IEEE Transactions on Geoscience and Remote Sensing 38*, 2 (March 2000), 754–765.

[149] Nagler, T., Rott, H., Malcher, P., and Müller, F. Assimilation of meteorological and remote sensing data for snowmelt runoff forecasting. *Remote sensing of Environment 112*, 4 (2008), 1408 – 1420.

[150] Nagler, T., Rott, H., Ripper, E., Bippus, G., and Hetzenecker, M. Advancements for Snowmelt Monitoring by Means of Sentinel-1 SAR. *Remote Sensing 8*, 4 (2016).

[151] Nakano, S., Ueno, G., and Higuchi, T. Merging particle filter for sequential data assimilation. *Nonlinear Processes in Geophysics 14*, 4 (July 2007), 395–408.

[152] National Ice Center. IMS Daily Northern Hemisphere Snow and Ice analysis at 1km, 4km, and 24km Resolutions, version 1. Tech. rep., National Snow and Ice Data Center, 2008.

[153] Neelam, M., and Mohanty, B. P. Global sensitivity analysis of the radiative transfer model. *Water Resources Research 51*, 4 (2015), 2428–2443.

[154] Niu, G.-Y., Yang, Z.-L., Mitchell, K. E., Chen, F., Ek, M. B., Barlage, M., Kumar, A., Manning, K., Niyogi, D., Rosero, E., Tewari, M., and Xia, Y. The community Noah land surface model with multiparameterization options (Noah-MP): 1. Model description and evaluation with local-scale measurements. *Journal of Geophysical Research: Atmospheres 116*, D12 (2011).

[155] Njoku, E. G., and Entekhabi, D. Passive microwave remote sensing of soil moisture. *Journal of hydrology 184*, 1-2 (1996), 101–129.

[156] Njoku, E. G., Jackson, T. J., Lakshmi, V., Chan, T. K., and Nghiem, S. V. Soil moisture retrieval from AMSR-E. *IEEE transactions on Geoscience and remote sensing 41*, 2 (2003), 215–229.

[157] Oliva, R., Daganzo, E., Kerr, Y. H., Mecklenburg, S., Nieto, S., Richaume, P., and Gruhier, C. SMOS radio frequency interference scenario: Status and actions taken to improve the RFI environment in the 1400–1427-MHz passive band. *IEEE Transactions on Geoscience and Remote Sensing 50*, 5 (2012), 1427–1439.

[158] Owe, M., de Jeu, R., and Holmes, T. Multisensor historical climatology of satellite-derived global land surface moisture. *Journal of Geophysical Research: Earth Surface 113*, F1 (2008).

[159] Pan, M., Sahoo, A. K., and Wood, E. F. Improving soil moisture retrievals from a physically-based radiative transfer model. *Remote Sensing of Environment 140* (2014), 130 – 140.

[160] Park, J., Korosov, A. A., Babiker, M., Sandven, S., and Won, J. Efficient Thermal Noise Removal for Sentinel-1 TOPSAR Cross-Polarization Channel. *IEEE Transactions on Geoscience and Remote Sensing 56*, 3 (2018), 1555–1565.

[161] Pellarin, T., Wigneron, J. ., Calvet, J. ., Berger, M., Douville, H., Ferrazzoli, P., Kerr, Y. H., Lopez-Baeza, E., Pulliainen, J., Simmonds, L. P., and Waldteufel, P. Two-year global simulation of L-band brightness temperatures over land. *IEEE Transactions on Geoscience and Remote Sensing 41*, 9 (2003), 2135–2139.

[162] Pervez, M. S., and Brown, J. F. Mapping Irrigated Lands at 250-m Scale by Merging MODIS Data and National Agricultural Statistics. *Remote Sensing 2*, 10 (2010), 2388–2412.

[163] Petropoulos, G. P., Ireland, G., and Barrett, B. Surface soil moisture retrievals from remote sensing: Current status, products & future trends. *Physics and Chemistry of the Earth, Parts A/B/C 83-84* (2015), 36 – 56. Emerging science and applications with microwave remote sensing data.

[164] Phan, X. V., Ferro-Famil, L., Gay, M., Durand, Y., Dumont, M., Morin, S., Allain, S., D'Urso, G., and Girard, A. 1D-Var multilayer assimilation of X-band SAR data into a detailed snowpack model. *The Cryosphere 8*, 5 (2014), 1975–1987.

[165] Piepmeier, J., Brown, S., Gales, J., Hong, L., Lagerloef, G., Le Vine, D., de Matthaeis, P., Meissner, T., Bindlish, R., Jackson, T., et al. Aquarius radiometer post-launch calibration for product version 2. Tech. rep., National Aeronautics and Space Administration, 2013.

[166] Pivot, F. C. C-Band SAR Imagery for Snow-Cover Monitoring at Treeline, Churchill, Manitoba, Canada. *Remote Sensing 4*, 7 (2012), 2133–2155.

[167] Polcher, J., Piles, M., Gelati, E., Barella-Ortiz, A., and Tello, M. Comparing surface-soil moisture from the SMOS mission and the ORCHIDEE land-surface model over the Iberian Peninsula. *Remote sensing of environment 174* (2016), 69–81.

[168] Pôssa, É. M., and Maillard, P. Precise Delineation of Small Water Bodies from Sentinel-1 Data using Support Vector Machine Classification. *Canadian Journal of Remote Sensing 44*, 3 (2018), 179–190.

[169] Potin, P., Rosich, B., Grimont, P., Miranda, N., Shurmer, I., O'Connell, A., Torres, R., and Krassenburg, M. Sentinel-1 Mission Status. In *Proceedings of EUSAR 2016: 11th European Conference on Synthetic Aperture Radar* (2016), pp. 1–6.

[170] Potin, P., Rosich, B., Roeder, J., and Bargellini, P. Sentinel-1 Mission operations concept. In *2014 IEEE Geoscience and Remote Sensing Symposium* (July 2014), pp. 1465–1468.

[171] Quets, J., Lannoy], G. J. D., Yaari], A. A., Chan, S., Cosh, M. H., Gruber, A., Reichle, R. H., der Schalie], R. V., and Wigneron, J.-P. Uncertainty in soil moisture retrievals: An ensemble approach using SMOS L-band microwave data. *Remote Sensing of Environment 229* (2019), 133 – 147.

[172] Rains, D., Han, X., Lievens, H., Montzka, C., and Verhoest, N. E. C. SMOS brightness temperature assimilation into the Community Land Model. *Hydrology and Earth System Sciences 21*, 11 (2017), 5929–5951.

[173] Ranković, V., Grujović, N., Divac, D., and Milivojević, N. Development of support vector regression identification model for prediction of dam structural behaviour. *Structural Safety 48* (2014), 33–39.

[174] Reichle, R., McLaughlin, D. B., and Entekhabi, D. Hydrologic Data Assimilation with the Ensemble Kalman Filter. *Journal of Hydrometeorology 130* (2002), 103–114.

[175] Reichle, R. H. Data assimilation methods in the Earth sciences. *Advances in Water Resources 31*, 11 (2008), 1411–1418.

[176] Reichle, R. H., De Lannoy, G. J. M., Forman, B. A., Draper, C. S., and Liu, Q. Connecting Satellite Observations with Water Cycle Variables Through Land Data Assimilation: Examples Using the NASA GEOS-5 LDAS. *Surveys in Geophysics 35*, 3 (2014), 577–606.

[177] Rienecker, M. M., Suarez, M. J., Gelaro, R., Todling, R., Bacmeister, J., Liu, E., Bosilovich, M. G., Schubert, S. D., Takacs, L., Kim, G. K., Bloom, S., Chen, J., Collins, D., Conaty, A., Da Silva, A., Gu, W., Joiner, J., Koster, R. D., Lucchesi, R., Molod, A., Owens, T., Pawson, S., Pegion, P., Redder, C. R., Reichle, R., Robertson, F. R., Ruddick, A. G., Sienkiewicz, M., and Woollen, J. MERRA: NASA's modern-era retrospective analysis for research and applications. *Journal of Climate 24*, 14 (2011), 3624–3648.

[178] Rodell, M., and Houser, P. R. Updating a Land Surface Model with MODIS-Derived Snow Cover. *Journal of Hydrometeorology 5*, 6 (2004), 1064–1075.

[179] Roodposhti, M. S., Safarrad, T., and Shahabi, H. Drought sensitivity mapping using two one-class support vector machine algorithms. *Atmospheric research 193* (2017), 73–82.

[180] Rott, H., and Nagler, T. Monitoring temporal dynamics of snowmelt with ERS-1 SAR. In *1995 International Geoscience and Remote Sensing Symposium, IGARSS '95. Quantitative Remote Sensing for Science and Applications* (July 1995), vol. 3, pp. 1747–1749 vol.3.

[181] Roy, A., Royer, A., and Turcotte, R. Improvement of springtime streamflow simulations in a boreal environment by incorporating snow-covered area derived from remote sensing data. *Journal of Hydrology 390*, 1 (2010), 35 – 44.

[182] Schaufler, S., Bauer-Marschallinger, B., Hochstöger, S., and Wagner, W. Modelling and correcting azimuthal anisotropy in Sentinel-1 backscatter data. *Remote Sensing Letters 9*, 8 (2018), 799–808.

[183] Schmugge, T., Jackson, T., Kustas, W., and Wang, J. Passive microwave remote sensing of soil moisture: Results from HAPEX, FIFE and MONSOON 90. *ISPRS Journal of Photogrammetry and Remote Sensing 47*, 2-3 (1992), 127–143.

[184] Schmugge, T. J., Kustas, W. P., Ritchie, J. C., Jackson, T. J., and Rango, A. Remote sensing in hydrology. *Advances in water resources 25*, 8-12 (2002), 1367–1385.

[185] Serreze, M. C., Clark, M. P., Armstrong, R. L., McGinnis, D. A., and Pulwarty, R. S. Characteristics of the western United States snowpack from snowpack telemetry (SNOTEL) data. *Water Resources Research 35*, 7 (1999), 2145–2160.

[186] Shi, J., Davis, R. E., and Dozier, J. Stereological determination of dry-snow parameters for discrete-scatterer microwave modeling. *Annals of Glaciology 17* (1993), 295–299.

[187] Shi, J., and Dozier, J. Radar backscattering response to wet snow. In *[Proceedings] IGARSS '92 International Geoscience and Remote Sensing Symposium* (May 1992), vol. 2, pp. 927–929.

[188] Shi, J., and Dozier, J. Estimation of snow water equivalence using SIR-C/X-SAR. I. Inferring snow density and subsurface properties. *IEEE Transactions on Geoscience and Remote Sensing 38*, 6 (2000), 2465–2474.

[189] Siebert, S., Henrich, V., Freken, K., and Bruke, J. Update of the digital global map of irrigation areas to version 5. *Institute of Crop Science and Resource Conservation, Rheinische Friedrich-Wilhelms-Universität, Bonn, Germany and Food and Agriculture Organization of the United Nations* (2013).

[190] Simpson, J. J., and McIntire, T. J. A recurrent neural network classifier for improved retrievals of areal extent of snow cover. *IEEE Transactions on Geoscience and Remote Sensing 39*, 10 (Oct 2001), 2135–2147.

[191] Singh, G., Venkataraman, G., Yamaguchi, Y., and Park, S. Capability Assessment of Fully Polarimetric ALOS–PALSAR Data for Discriminating Wet Snow From Other Scattering Types in Mountainous Regions. *IEEE Transactions on Geoscience and Remote Sensing 52*, 2 (Feb 2014), 1177–1196.

[192] Slater, A. G., and Clark, M. P. Snow Data Assimilation via an Ensemble Kalman Filter. *Journal of Hydrometeorology 7*, 3 (2006), 478–493.

[193] Slevin, D., Tett, S., and Williams, M. Multi-site evaluation of the JULES land surface model using global and local data. *Geosci. Model Dev. Discuss 7* (2014), 5341–5380.

[194] Smola, A. J., and Schölkopf, B. A tutorial on support vector regression. *Statistics and Computing 14*, 3 (Aug 2004), 99–222.

[195] Solomatine, D. P., and Shrestha, D. L. A novel method to estimate model uncertainty using machine learning techniques. *Water Resources Research 45*, 12 (2009).

[196] Song, S., and Wang, W. Impacts of Antecedent Soil Moisture on the Rainfall-Runoff Transformation Process Based on High-Resolution Observations in Soil Tank Experiments. *Water 11*, 2 (2019), 296.

[197] Sturm, M., Goldstein, M. A., and Parr, C. Water and life from snow: A trillion dollar science question. *Water Resources Research 53*, 5 (2017), 3534–3544.

[198] Sun, L., Seidou, O., Nistor, I., and Liu, K. Review of the Kalman-type hydrological data assimilation. *Hydrological Sciences Journal 61*, 13 (2016), 2348–2366.

[199] Suzuki, K., and Zupanski, M. Uncertainty in solid precipitation and snow depth prediction for Siberia using the Noah and Noah-MP land surface models. *Frontiers of Earth Science 12*, 4 (2018), 672–682.

[200] Tait, A. Estimation of snow water equivalent using passive microwave radiation data. *Remote Sensing of Environment 64*, 3 (1998), 286–291.

[201] Tang, Q., Gao, H., Lu, H., and Lettenmaier, D. P. Remote sensing: hydrology. *Progress in Physical Geography 33*, 4 (2009), 490–509.

[202] Tedesco, M., and Narvekar, P. S. Assessment of the nasa amsr-e swe product. *IEEE Journal of Selected Topics in Applied Earth Observations and Remote Sensing 3*, 1 (March 2010), 141–159.

[203] Tedesco, M., Pulliainen, J., Takala, M., Hallikainen, M., and Pampaloni, P. Artificial neural network-based techniques for the retrieval of SWE and snow depth from SSM/I data. *Remote Sensing of Environment 90*, 1 (2004), 76 – 85.

[204] Thakur, P. K., Aggarwal, S., Garg, P., Garg, R., Mani, S., Pandit, A., and Kumar, S. Snow physical parameters estimation using space-based Synthetic Aperture Radar. *Geocarto International 27*, 3 (2012), 263–288.

[205] Torres, R., Snoeij, P., Geudtner, D., Bibby, D., Davidson, M., Attema, E., Potin, P., Rommen, B., Floury, N., Brown, M., Traver, I. N., Deghaye, P., Duesmann, B., Rosich, B., Miranda, N., Bruno, C., L'Abbate, M., Croci, R., Pietropaolo, A., Huchler, M., and Rostan, F. GMES Sentinel-1 mission. *Remote Sensing of Environment 120* (2012), 9 – 24. The Sentinel Missions - New Opportunities for Science.

[206] Toure, A. M., Luojus, K., Rodell, M., Beaudoing, H., and Getirana, A. Evaluation of Simulated Snow and Snowmelt Timing in the Community Land Model Using Satellite-Based Products and Streamflow Observations. *Journal of Advances in Modeling Earth Systems 10*, 11 (2018), 2933–2951.

[207] Tsai, Y.-L. S., Dietz, A., Oppelt, N., and Kuenzer, C. Wet and Dry Snow Detection Using Sentinel-1 SAR Data for Mountainous Areas with a Machine Learning Technique. *Remote Sensing 11*, 8 (2019).

[208] Tsang, L., Chen, Z., Oh, S., Marks, R. J., and Chang, A. T. C. Inversion of snow parameters from passive microwave remote sensing measurements by a neural network trained with a multiple scattering model. *IEEE Transactions on Geoscience and Remote Sensing 30*, 5 (Sep. 1992), 1015–1024.

[209] Tsang, L., Kong, J. A., and Shin, R. T. *Theory of Microwave Remote Sensing*. Wiley series in remote sensing. Wiley, 1985.

[210] Tsui, C.-C. *Robust control system design: advanced state space techniques*. CRC Press, 2003, ch. 1.3.

[211] Ulaby, F., and Long, D. *Microwave Radar and Radiometric Remote Sensing*. University of Michigan Press, 2014.

[212] Ulaby, F. T., and Stiles, W. H. The active and passive microwave response to snow parameters: 2. Water equivalent of dry snow. *Journal of Geophysical Research: Oceans 85*, C2 (1980), 1045–1049.

[213] Vapnik, V. *The nature of statistical learning theory*. Springer science & business media, 1995.

[214] Wagner, W., Hahn, S., Kidd, R., Melzer, T., Bartalis, Z., Hasenauer, S., Figa-Saldaña, J., de Rosnay, P., Jann, A., Schneider, S., Komma, J., Kubu, G., Brugger, K., Aubrecht, C., Züger, J., Gangkofner, U., Kienberger, S., Brocca, L., Wang, Y., Blöschl, G., Eitzinger, J., Steinnocher, K., Zeil, P., and Rubel, F. The ASCAT soil moisture product: A review of its specifications, validation results, and emerging applications. *Meteorologische Zeitschrift 22*, 1 (2013), 5–33.

[215] Wang, J. R., and Schmugge, T. J. An empirical model for the complex dielectric permittivity of soils as a function of water content. *IEEE Transactions on Geoscience and Remote Sensing GE-18*, 4 (1980), 288–295.

[216] Westman, W. E., and Paris, J. F. Detecting forest structure and biomass with C-band multipolarization radar: Physical model and field tests. *Remote Sensing of Environment 22*, 2 (1987), 249 – 269.

[217] Wigneron, J.-P., Kerr, Y., Waldteufel, P., Saleh, K., Escorihuela, M.-J., Richaume, P., Ferrazzoli, P., [de Rosnay], P., Gurney, R., Calvet, J.-C., Grant, J., Guglielmetti, M., Hornbuckle, B., Mätzler, C., Pellarin, T., and Schwank, M. L-band microwave emission of the biosphere (L-MEB) model: Description and calibration against experimental data sets over crop fields. *Remote Sensing of Environment 107*, 4 (2007), 639–655.

[218] Wilcoxon, F. Individual comparisons by ranking methods. In *Breakthroughs in statistics*. Springer, 1992, pp. 196–202.

[219] Willis, R., and Yeh, W. *Groundwater systems planning and management*. Prentice Hall Inc., Old Tappan, NJ, 1 1987.

[220] Winsvold, S. H., Kääb, A., Nuth, C., Andreassen, L. M., van Pelt, W. J. J., and Schellenberger, T. Using SAR satellite data time series for regional glacier mapping. *The Cryosphere 12*, 3 (2018), 867–890.

[221] Wood, E. F., Roundy, J. K., Troy, T. J., van Beek, L. P. H., Bierkens, M. F. P., Blyth, E., de Roo, A., Döll, P., Ek, M., Famiglietti, J., Gochis, D., van de Giesen, N., Houser, P., Jaffé, P. R., Kollet, S., Lehner, B., Lettenmaier, D. P., Peters-Lidard, C., Sivapalan, M., Sheffield, J., Wade, A., and Whitehead, P. Hyperresolution global land surface modeling: Meeting a grand challenge for monitoring Earth's terrestrial water. *Water Resources Research 47*, 5 (2011).

[222] Wösten, J., Pachepsky, Y., and Rawls, W. Pedotransfer functions: bridging the gap between available basic soil data and missing soil hydraulic characteristics. *Journal of Hydrology 251*, 3 (2001), 123 – 150.

[223] Xiao, X., Zhang, T., Zhong, X., Shao, W., and Li, X. Support vector regression snow-depth retrieval algorithm using passive microwave remote sensing data. *Remote Sensing of Environment 210* (2018), 48 – 64.

[224] Xue, Y., and Forman, B. A. Atmospheric and Forest Decoupling of Passive Microwave Brightness Temperature Observations Over Snow-Covered Terrain in North America. *IEEE Journal of Selected Topics in Applied Earth Observations and Remote Sensing 10*, 7 (2017), 3172–3189.

[225] Xue, Y., Forman, B. A., and Reichle, R. H. Estimating snow mass in North America through assimilation of AMSR-E brightness temperature observations using the Catchment land surface model and support vector machines. *Water Resources Research* (2018), 1–22.

[226] Yang, Z.-L., Niu, G.-Y., Mitchell, K. E., Chen, F., Ek, M. B., Barlage, M., Longuevergne, L., Manning, K., Niyogi, D., Tewari, M., and Xia, Y. The community Noah land surface model with multiparameterization options (Noah-MP): 2. Evaluation over global river basins. *Journal of Geophysical Research: Atmospheres 116*, D12 (2011).

[227] Yu, P. S., Chen, S. T., and Chang, I. F. Support vector regression for real-time flood stage forecasting. *Journal of Hydrology 328*, 3 (2006), 704 – 716.

[228] Yueh, S. H., Dinardo, S. J., Akgiray, A., West, R., Cline, D. W., and Elder, K. Airborne Ku-Band Polarimetric Radar Remote Sensing of Terrestrial Snow Cover. *IEEE Transactions on Geoscience and Remote Sensing 47*, 10 (Oct 2009), 3347–3364.

[229] Zehe, E., Becker, R., Bárdossy, A., and Plate, E. Uncertainty of simulated catchment runoff response in the presence of threshold processes: Role of initial soil moisture and precipitation. *Journal of hydrology 315*, 1-4 (2005), 183–202.